Alma Mater Studiorum · University of Bologna

School of Science
Department of Physics and Astronomy
Master Degree in Physics

Innovative materials for direct X-ray detection: organic semiconductors and 2D transition metal dichalcogenides

Supervisor:
Prof. Laura Basiricò

Co-supervisor:
Dr. Ilaria Fratelli

Submitted by:
Mikhail Bandurist

Academic Year 2022/2023

Table of Contents

Abstract ... 1

Introduction ... 1

Chapter 1 Overview on X-ray detection ... 4

1.1 Sources of characteristic X-rays ... 4

1.2 X-ray tube ... 6

1.3 Interaction mechanisms of X-rays with matter ... 10

1.4 Inorganic semiconducting materials for X-ray detection ... 13

Chapter 2 Thin-film X-ray detectors based on organic semiconductors and transition metal dichalcogenides ... 21

2.1 Device architecture of thin-film X-ray detectors ... 21

2.2 Thin Film Transistors ... 22

2.2.1 Transfer and output characteristics of a TFT ... 23

2.3 X-ray detection mechanism for semiconducting thin-film X-ray detectors ... 26

2.3.1 Charge collection and Photoconductive gain ... 26

2.4 X-ray Sensitivity ... 29

2.5 Organic and hybrid semiconductor-based X-ray detectors: State of the Art ... 31

2.6 Overview on X-ray detectors based on TMTES:PS ... 32

2.7 Overview on 2D transition metal dichalcogenides ... 38

2.7.1 Crystal structure and energy gap ... 38

2.7.2 Fabrication methods of 1L-MoS_2 ... 41

2.7.3 Overview on electrical properties of MoS_2-based TFTs ... 45

2.7.4 Overview on the performance of 1L-MoS_2 direct X-ray detectors ... 47

Chapter 3 Experimental Methods ... 52

3.1 Experimental setups ... 52

3.2 MoS2 Samples ... 57

3.2.1 Electrical characterization of the MoS_2 phototransistors ... 58

3.2.2 Characterization of the MoS_2 phototransistors under X-rays ... 59

3.3 TMTES:PS samples 60
3.3.1 Fabrication methods 61
3.3.2 Electrical characterization 62
3.3.3 Characterization under X-rays 64
Chapter 4 Results for MoS_2-based X-ray detectors 66
4.1 Electrical characterization of the MoS_2 detectors 66
4.2 X-ray measurements of the MoS_2-based detectors 68
4.3 Comparison with literature 73
4.4 Side Effects of the MoS_2 device characterization 74
Chapter 5 Results for TMTES:PS samples 77
5.1 Electrical characterization of the TMTES:PS detectors 77
5.1.1 Overview on the device performance and results 77
5.1.2 Dependence of the electrical parameters on the TMTES:PS ratio 79
5.2 X-ray measurement of the TMTES:PS detectors 80
5.3 Comparative analysis of TMTES:PS X-ray detectors 84
5.4 Side Effects of the TMTES:PS characterization 87
Chapter 6 Conclusions 89
Bibliography 91

Abstract

The objective of this experimental work was to evaluate the performance of thin-film X-ray detectors represented as thin-film transistors and based on transition metal dichalcogenide MoS_2 and on a fully organic semiconductor 1,4,8,11-tetramethyl-6,13-triethylsilylethynyl pentacene (TMTES) blended with polystyrene (PS) with the TMTES:PS ratio of 17:3, 9:1, 19:1 and 39:9. As a result, the average sensitivity of the MoS_2-based photodetectors was estimated to lie in the range between 10^{11} and 10^{12} μC/(Gy·cm^3), while the TMTES:PS exhibited the sensitivity per unit area of $(3.4 \pm 1.3) \times 10^3$ μC/(Gy·cm^2) and $(2.7 \pm 0.8) \times 10^3$ μC/(Gy·cm^2) for the TMTES:PS ratio of 17:3 and 9:1, respectively. Such sensitivity per unit area is one order of magnitude lower than that evaluated for the MoS2-based devices. Additionally, in combination with previous research conducted on the TMTES:PS X-ray detectors, it was found that the overall performance of the devices deteriorates with the reduction of relative amount of PS in the blend. On the whole, both types of photodetectors perform excellent characteristics upon X-ray exposure, which provides motivation for further research on the MoS_2 and TMTES:PS semiconductor applications in direct X-ray detection.

Introduction

My experimental research regards the use of prominent 2D semiconducting materials in direct X-ray detection devices. In particular, I examine the performance of photodetectors with the thin-film transistor (TFT) architecture based on two distinct semiconductors, such as transition metals dichalcogenides (TMDCs) represented by *n*-type molybdenum disulfide MoS_2, and a fully organic *p*-type semiconductor *p*-type 1,4,8,11-tetramethyl-6,13-triethylsilylethynyl pentacene (TMTES) blended with polystyrene (PS) in four different TMTES:PS ratios of 17:3, 9:1, 19:1 and 39:1. Both semiconducting materials are still poorly investigated for mass production, yet they have already been reported to possess excellent characteristics as photosensitive materials for X-ray radiation detection. As a consequence, further research on the application of these materials for the ionizing radiation sensing would become a significant contribution to the development of perspective thin-film flexible X-ray detectors.

The goal of this experimental study was to assess the electrical performance of both MoS_2- and TMTES:PS-based TFTs and to evaluate their X-ray detection efficiency represented by the sensitivity value of the devices. For this purpose, each sample from both batches initially underwent an electrical characterization in order to derive its main electrical parameters, such as the majority charge carrier mobility μ, threshold voltage V_{th}, subthreshold swing *SS* and the ON/OFF ratio. After that the TFTs were exposed to a DC characterization under X-ray radiation generated by an X-ray tube. By performing a series of irradiation pulses, the sensitivity of a device was calculated.

In the first part of the experiment, photodetectors with the MoS_2 based transistor were characterized both electrically and upon impinging X-rays. The final objective was to calculate the average sensitivity of the batch and to compare it with outer research, where MoS_2 active layer has been employed for X-ray detection only in photoconductor architecture, while this study is the first reporting the performance of a MoS_2-based field effect transistor for such application. Similarly, the second part involved the electrical and X-ray characterization of the TMTES:PS-based photodetectors. By measuring the average sensitivity for each TMTES:PS ratio, we managed to perform the analysis on the device sensitivity behaviour across varying the relative quantity of PS in the blend. To achieve more extensive and reliable output, the obtained results were consolidated with the data extracted from previous research concerning the TMTES:PS X-ray detectors.

The complete dissertation is divided in several chapters describing the general structure of the materials and the experimental procedure. Chapter 1 provides an overview on the sources of X-ray radiation and its interaction with matter. In particular, the configuration and working principle of an X-ray tube are discussed in detail, since this device was practically used as an X-ray source in the experimental part of the research. Besides, commonly used solid-state X-ray detectors based on silicon (Si), germanium (Ge), gallium arsenide (GaAs) and on other conventional semiconductors, are surveyed.

In Chapter 2 the general theory of thin-film transistor architecture and its electrical performance is presented. Also, methods of derivation of electrical parameters of a TFT, including the analysis of its sensitivity, are discussed. After that the chapter provides a comprehensive overview on the TMTES:PS organic semiconductor and its application as an active channel in thin-film X-ray detectors. The subsequent research considers the general structure of TMDCs and focuses on the MoS_2 thin films and their fabrication methods. The application of single- and multilayer MoS_2 nanosheets in TFTs and in X-ray photoconductors is thoroughly contemplated.

Chapter 3 describes the whole experimental procedure, during which the MoS_2 and TMTES:PS TFTs subsequently underwent the electrical and X-ray characterization. Specifically, the chapter introduces the equipment used for each type of photodetectors and the general steps to acquire the sensitivity of a device.

In Chapter 4 the obtained properties of the MoS_2-based X-ray detectors are presented and discussed. The calculated average electrical parameters and device sensitivity is then compared to the corresponding values from literature. Additionally, the chapter provides an analysis on different side effects that occurred along with the characterization of the MoS_2 TFTs.

Chapter 5 depicts an analogous analysis of the TMTES:PS devices performance during an electrical characterization and under X-rays. The average electrical parameters and sensitivity are calculated for each TMTES:PS ratio. Their dependence on the PS relative amount is then scrutinized and given a theoretical explanation. As for the MoS_2-based devices, some non-idealities are reported during the experimental procedure. Finally, Chapter 6 summarizes the main results obtained for the MoS_2 and TMTES:PS X-ray detectors and provides the comparison of their efficiencies towards the ionizing radiation detection.

Chapter 1 Overview on X-ray detection

Ionizing electromagnetic radiation is one of the basic types of radiation along with heavy charged particles, neutron and electron radiation. Particular interest is represented by the photons with the wavelength in the range between 0.1 Å and 1 Å, which constitute so-called X-rays. Such radiation is widely used in material science, crystallography, nuclear medicine, aerospace and in many other technological domains. The physics behind the interaction form the basis for X-ray detection. Therefore, before analyzing specifically the detection mechanisms and devices for X-ray detection, it is essential to study how X-ray photons are created and their interaction with atoms in matter. For this purpose, in this chapter I discuss basic phenomena that serve as X-ray sources, including atom excitation (used in X-ray tubes), excitation by radioactive decay and synchrotron radiation. After that the working principle of an X-ray tube is presented, since this tool was used in my research.

The next section will be dedicated to main mechanisms of interaction between X-ray with absorber atoms, which include photoelectric absorption, Rayleigh scattering etc. Finally, I will briefly discuss currently used X-ray detectors based on inorganic semiconductors, such as silicon (Si), germanium (Ge), gallium arsenide (GaAs) and other conventional semiconducting materials.

1.1 Sources of characteristic X-rays

If the orbital electrons in an atom are disrupted from their normal configuration by some excitation process, the atom may exist in an excited state for a relatively short period of time. Eventually, there is a natural tendency for the orbital electrons to rearrange themselves to return the atom to its lowest energy state (ground state) within a time which is characteristically in the range of nanoseconds for a solid material. The energy emitted in the transition from the excited state to the ground state takes the form of a *characteristic X-ray photon* whose energy is defined as the difference between the initial and the final states of the atom [1].

A large number of different physical processes can lead to the population of excited atomic states from which characteristic X-rays originate. The most common mechanisms include:

- **Excitation by radioactive decay**

In the nuclear decay process of electron capture, the nuclear charge is decreased by the capture of an orbital electron, most often a *K*-electron. The resulting atom still has the right number of electrons, but the capture process also creates a vacancy in one of the inner shells. Once this vacancy is subsequently filled, characteristic X-rays are generated [1].

- **Excitation by external radiation**

This method involves an external source of radiation (X-rays, electrons, α-particles etc.) which strikes the target, creating excited or ionized atoms in the target. Since many of these atoms eventually de-excite to the ground state through the emission of characteristic X-rays, the target can serve as a localized source of these X-rays.

As an example, the incident radiation may consist of X-rays generated in a conventional X-ray tube. The external X-rays may then interact with the atoms of a target through photoelectric absorption; therefore, the excited atoms will emit characteristic X-rays creating their X-ray spectrum. This process is called *X-ray fluorescence*.

Another example of incident radiation could be an external electron beam. In this case the characteristic X-ray spectrum from the target will be contaminated by the continuous *bremsstrahlung* spectrum generated by the deceleration of impinging electrons by their interaction with atomic nuclei. For targets of low atomic number, acceleration potentials of only a few thousand volts are required, which allows to use compact electron sources.

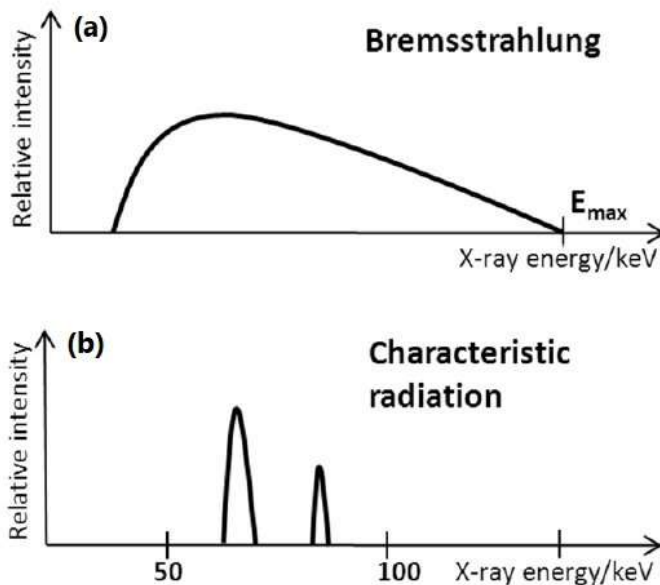

Figure 1.1 Typical X-ray spectrum: (**a**) bremsstrahlung radiation outputs continuous spectrum; (**b**) characteristic radiation spectrum represents discrete peaks [2].

The excitation of a target can also be due to heavy charged particles. The interactions of these particles with the target will give rise to the excited atoms, which will subsequently emit characteristic X-rays. For compact and portable sources, α-particles are often used as incident radiation. As α-particle emitters, ^{210}Po and ^{244}Cm are commonly used [1].

- **Synchrotron radiation**

X-rays can be also produced by electron beam bent into a circular orbit. According to the electromagnetic theory, a fraction of the beam energy is released when the trajectory of the electrons is deflected within a cycle. When extracted from the accelerator in a tangential direction, the radiation appears as an intense and highly directional beam of photons with the energy ranging from visible light (~eV) to X-rays (~10^4 eV). Although limited to large-scale centralized user facilities, this unique form of electromagnetic radiation is of great demand because of its high intensity, monoenergetic and tunable radiation energy [1].

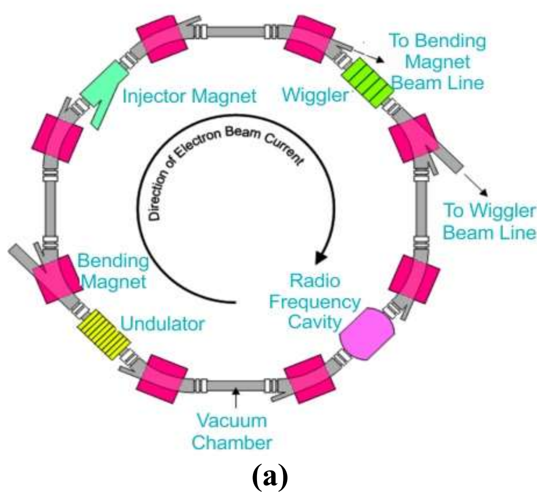

(a)

(b)

Figure 1.2 (**a**) Schematic representation of a synchrotron [3]; as depicted, different tools can be used for electron beam deflection, which results in X-ray emission. (**b**) A ring-shaped synchrotron ESRF constructed in Grenoble, France [4].

1.2 X-ray tube

In this section I would like to focus more on a specific radiation source – an X-ray tube, that is broadly employed in numerous laboratories and medical departments. Since such device was also used during the experimental part of my research, a comprehensive description of the architecture and working principle of an X-ray tube is necessary to have full perception of how the X-ray measurements were performed.

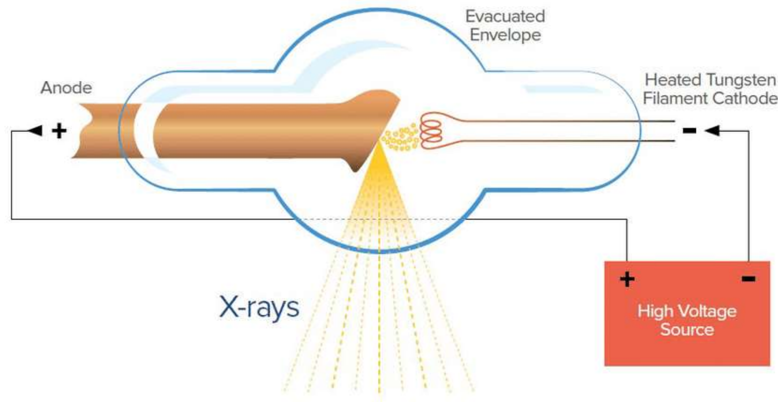

Figure 1.3 Schematic representation of an X-ray tube [5].

As depicted in Fig. 1.3, X-rays are generated from the conversion of kinetic energy of electrons into electromagnetic radiation when they become decelerated by interaction with a target material. A high voltage in the range of 20-150 kV is generated between the anode and the cathode of an X-ray tube. [6]. The negative pole of the voltage is applied to the cathode, considered as the source of electrons, and the positive pole is applied to the anode, which is the target for the electrons. In order to eject electrons from the cathode, a current through a filament at the cathode is generated by a separate voltage circuit. The thermionic emission effect causes the filament to heat up and to expel the electrons into vacuum. Once the electrons are ejected, they are accelerated by the X-ray tube voltage and strikes the anode. At the anode, electrons start to interact with the atoms of the anode. In particular, the positive nuclei start to attract negatively charged electrons, causing their deflection and deceleration and resulting into emission of *bremsstrahlung* X-ray radiation from the anode in different directions. By providing different collimators, a beam of X-ray photons with certain size and shape is obtained [6], [5].

The operational characteristics of an X-ray tube include mainly the voltage and the current between the cathode and the anode. The first one allows to control kinetic energy of the electrons and thus, the energy of generated X-ray photons. The latter is used to tune the number of electrons impinging on the anode and to vary the number of generated photons. Therefore, controlling both these values allows us to establish the desired energy spectra and intensity of X-rays.

Main factors that affect X-ray production efficiency include the kinetic energy of the incident electrons and the atomic number Z of the anode (target material). The approximate ratio of radiative energy loss (bremsstrahlung X-rays) to collisional energy loss (excitation of atoms) is the following:

$$\frac{Radiative\ energy\ loss}{Collisional\ energy\ loss} \cong \frac{E_k Z}{820{,}0}, \text{for } E_k \leq 150 \text{ keV} \quad 1.1$$

where E_k is the kinetic energy of incident electrons [5]. Most X-ray tube anodes are made of tungsten, due to its high atomic number (Z = 74) and exceptionally high melting point of 3422 ℃ [7] with a correspondingly low rate of evaporation. In mammography, molybdenum (Z = 42) and rhodium (Z=45) are also used. For instance, if we consider incident electrons with kinetic energy of 100 keV impinging on a tungsten anode, the ratio of radiative to collisional losses will be ≈ 0.9%, meaning that more than 99% of the incident electron energy gets converted to heat. Consequently, the heat dissipation problem is a significant concern for employment of X-ray tubes [5], [8].

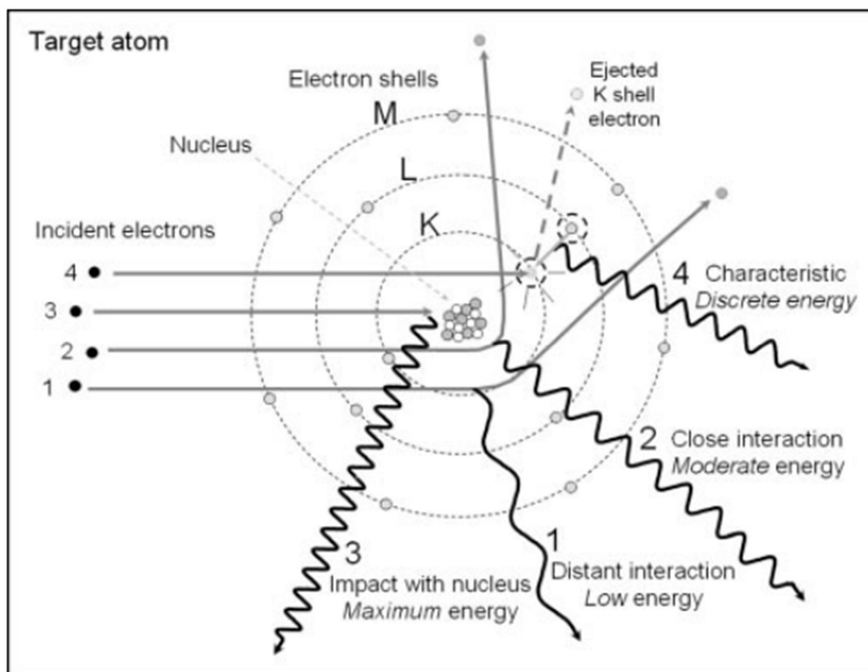

Figure 1.4 Mechanisms of formation of bremsstrahlung radiation and characteristic X-rays. Events 1, 2 and 3 demonstrate the interaction of incident electrons in vicinity of the target nucleus producing bremsstrahlung X-rays by the deceleration and deflection of the electrons through Coulomb interaction. Event 4 depicts emission of characteristic X-rays by ejecting of an orbital electron from the K-shell. An unstable vacancy is formed and an outer shell electron occupies the vacancy emitting energy in the form of a characteristic X-ray photon [9].

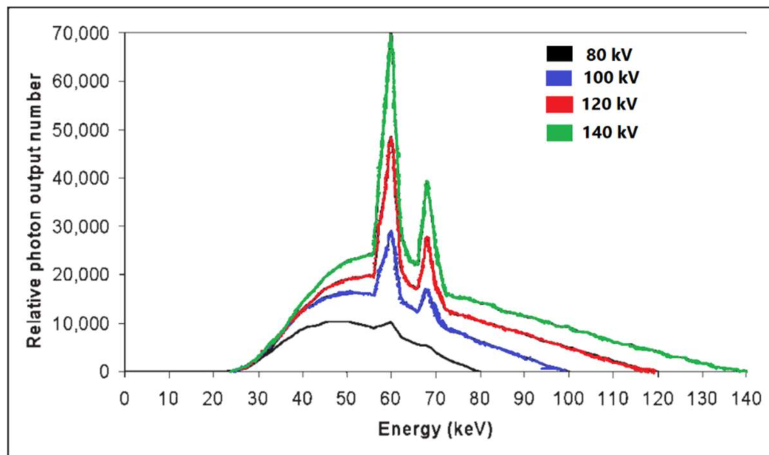

Figure 1.5 Bremsstrahlung and characteristic X-ray energy spectrum for a tungsten anode with the X-ray tube operating at 80, 100, 120 and 140 kV at equal tube current [9].

The X-ray spectrum (Fig. 1.5) output by an X-ray tube consists of discrete characteristic X-rays and continuous bremsstrahlung radiation spectrum with the maximum X-ray energy determined by the potential difference between electrodes. The closer the incident electrons travel to the absorber nucleus, the more intense will be their interaction and the higher will be the emitted photon energy. However, probability of close interaction with the nucleus decreases, thus, decreasing the number of high-energy photons. Therefore, an unfiltered bremsstrahlung radiation energy spectrum is formed the minimum rate at the highest energy and its linear increase with decreasing energy. At the same time low-energy photons are easily attenuated from the beam exiting the X-ray tube window (by Al or Be filters, for example). The measured bremsstrahlung spectrum will have its peak at intermediate energy decreasing to zero at low X-ray energy [9].

Discrete characteristic X-ray spectrum is created by the removal of orbital electrons from the target atoms through their interaction with incident electrons. Each electron shell (denoted by K, L, M etc.) have certain biding energies, which for tungsten are 69.5 keV, 11.5 keV and 2.5 keV for the K, L and M shells, respectively. If a highly energetic incident electron has its kinetic energy of at least 69.5 keV, it can potentially eject a K-shell electron leaving a vacancy in the K-shell. Since the atom becomes energetically unstable, another electron for outer shells (L, M, N etc.) will occupy the vacancy in the K-shell (Fig. 1.4, event 4), emitting its energy in the form of an X-ray photon. The energy of the photon is defined as the difference in the binding energies of the K-shell and the outer shell. For example, an electron passing from the L-shell to the K-shell will emit a photon with the energy of 69.5-11.5 = 57.0 keV. Since each element has different electron binding energies, the emitted X-ray energies are characteristic of a specific anode element. These characteristic X-rays will create discrete energy spectrum, which shall be added to the continuous bremsstrahlung spectrum. It

is worth noting that characteristic X-rays fully depend on the applied voltage, for example, the K-characteristic radiation from a tungsten anode will occur only of the X-ray tube is operated at voltage of ≥ 69.5 kV. As the tube voltage is increased above the minimum value, characteristic X-ray production will also increase its fraction in the X-ray spectrum [9].

1.3 Interaction mechanisms of X-rays with matter

Although a large number mechanisms of interaction between electromagnetic radiation and matter are known, the three major types are usually taken into consideration:

- Photoelectric absorption
- Compton scattering
- Pair production

The common feature of these interactions is partial or complete transfer of the photon energy to an orbital electron, which results in abrupt disappearance of an impinging photon or change of its trajectory by scattering on the electron [1]. Besides, each interaction mechanism probability depends both on the energy of an impinging photon and the atomic number *Z* of an absorber.

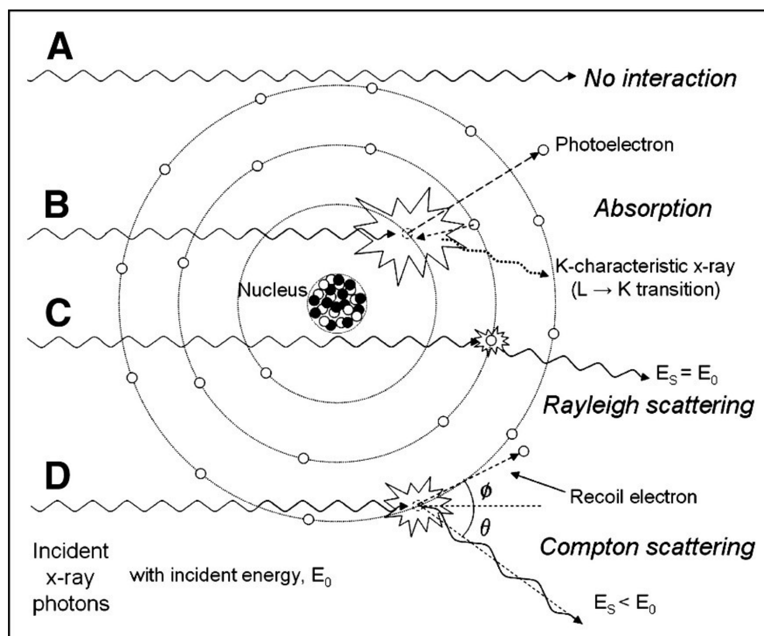

Figure 1.6 Schematic representation of X-ray interactions. (**A**) Incident photons perform no interaction with the absorber material; (**B**) Photoelectric absorption results in total removal of impinging X-ray photon with energy greater than binding energy of an electron in its shell, with excess energy transformed into kinetic energy of the photoelectron; (**C**) coherent (Rayleigh) scattering is the interaction between the photon and an electron (or an atom), in which no energy is exchanged and the photon is deflected from its original direction; (**D**) Compton scattering interactions occur with essentially unbound electrons, with transfer of energy shared between the recoil electron and scattered photon [10].

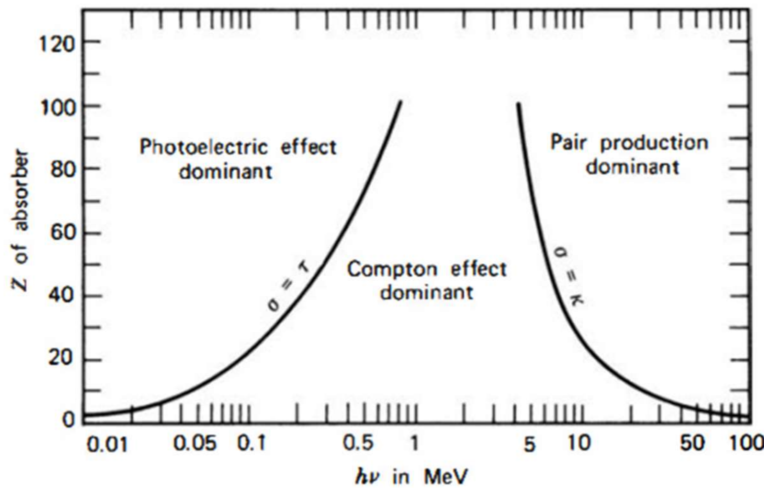

Figure 1.7 Schematic representation of relative probability for different interaction types depending on the Z of an absorber atom and on the photon energy $h\nu$. The lines illustrate the values of $h\nu$ for which the two neighbouring effects are equally probable [1].

- **Photoelectric absorption**

In the photoelectric absorption process, a photon interacts with an absorber atom, in which the photon passes its energy to an orbital electron and disappears. Instead, an energetic *photoelectron* is ejected by the atom from one of its bound shells. The photoelectron energy is calculated according to the energy conservation law:

$$E_{e^-} = h\nu - E_b \quad 1.2$$

where E_b is the binding energy of the photoelectron in its original shell. In addition to the photoelectron, the photoelectron absorption also generates an ionized absorber atom with a vacancy in one of its shells. This vacancy is quickly filled through capture of a free electron or rearrangement of electrons from the other shells. As a result, one or more characteristic X-ray photons may be generated. In most cases these X-rays are reabsorbed close to the original site through photoelectric absorption involving less tightly bound shells. However, their possible escape from radiation detectors can influence their response. In some fraction of the cases, the emission of an Auger electron may substitute the characteristic X-ray in carrying away the atomic excitation energy.

According to Fig. 1.7, a photoelectric absorption process is the predominant type of interaction for X-rays (and gamma-rays) of relatively low energy for low-Z absorbers. For example, in water photoelectric absorption is dominant up to ~26 keV, while in bones it stays dominant up to ~45 keV [11]. The process is also enhanced for absorber materials of high atomic number Z. Although there is no single analytic expression for the probability of photoelectric absorption per atom over all ranges of photon energy E_γ and Z, its rough approximation is present:

$$\tau \cong const \times \frac{Z^n}{E_\gamma^{3.5}} \qquad 1.3$$

where n varies between 4 and 5 over gamma-ray energy region [1].

- **Compton scattering**

In Compton scattering, the incoming X-ray (or gamma-ray) photon is deflected through an angle θ with respect to its original direction (Fig. 1.8) by its interaction with an electron in an absorber atom. The photon transfers a portion of its energy to the electron (assumed to be initially at rest), which is called *recoil electron*. Since any angle of scattering is possible, the energy transferred to the electron can vary from zero to a large fraction of the impinging photon energy [1].

The expression that relates the energy transfer and the scattering angle can be derived by combining the energy and momentum conservation laws:

$$h\nu' = \frac{h\nu}{1 + \frac{h\nu}{m_0c^2}(1 - \cos\theta)} \qquad 1.4$$

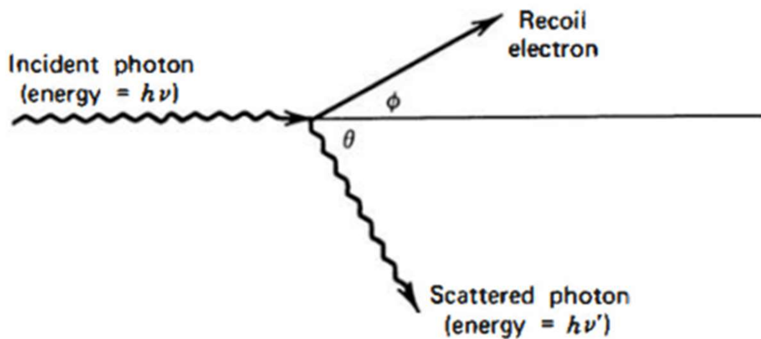

Figure 1.8 Schematic representation of the Compton scattering process [1].

where m_0c^2 is the rest mass energy of the electron (0.511 MeV). The probability of Compton scattering per atom depends on the number of electrons availble as scattering targets and thus, increases linearly with Z [1].

- **Coherent scattering**

In addition to Compton scattering, another type of scattering can occur, when an X-ray (or gamma-ray) photon interacts coherently with an absorber atom. Such *coherent scattering* or *Rayleigh scattering* process neither excites nor ionizes the atom and the scattered photon retains its original

energy, although its direction is changed. The probability of Rayleigh scattering is significant only for low photon energies (usually below a few hundred keV for common materials) and in high-Z absorbers. Since the average deflection angle decreases with increasing energy, the practical importance of coherent scattering is restricted to low photon energies [1].

- **Pair production**

If the gamma-ray energy exceeds twice the rest-mass energy of an electron ($E_{\gamma} \geq 1.02$ MeV), the process of pair production becomes energetically possible. In this interaction (which must take place in the Coulomb field of the nucleus), the gamma-ray photon disappears generating an electron-positron pair. All the excess energy goes into kinetic energy shared by the positron and the electron. Since the positron will subsequently annihilate after slowing down in the absorbing medium, two annihilation photons are normally produced as secondary products of the interaction. No precise expression exists for the probability of pair per nucleus, but its magnitude varies approximately as the square of the absorber atomic number [1].

- **Absorbed dose**

The mean absorbed radiation energy per unit mass of the absorber is called *absorbed dose*. The SI unit of absorbed dose is defined as *gray* (Gy) which is 1 joule per kilogram. The absorbed dose is a reasonable measure of the chemical or physical effects created by a given radiation exposure in an absorbing material [1].

1.4 Inorganic semiconducting materials for X-ray detection

The whole multitude of X-ray detection devices might be unified by the principle of creation of charges (free electrons and holes) by absorption of energy due to the passing of X-rays through a material. The most commonly used examples are gas ionization chambers, scintillation counters and semiconductor-based detectors. While the first two types have quite complex configuration, the semiconductor-based devices provide outstanding combination of compact size, high speed, spatial resolution and sensitivity [12]. The use of semiconductor materials as radiation detectors can result in a much larger number of carriers for a given incident radiation event that is possible for any other common detector type [1]. The fundamental information carriers are *electron-hole* pairs created by a charged particle or a photon (as primary radiation or its secondary products) in the detector. The motion of generated electrons and holes in an applied electric field generates the basic electrical signal (also called photocurrent) from the semiconductor detector [1].

Before discussing concrete solid-state X-ray detectors and their architectures, it is good practice to classify the group of semiconductor-based detectors via *direct* and *indirect* detection

mechanisms. In the indirect detection, the incident X-ray energy is converted into an electrical signal through a two-step process by using a scintillator material (e.g. CsI or Gd_2O_2S [13]). In the first step the X-ray radiation impinges on a scintillator, which converts the incident radiation into visible photons. In the second step, a photodetector (e.g. a photodiode) converts the visible photons into an electrical signal. In the direct detection, the incoming ionizing radiation is converted into photocurrent directly in a semiconductor material. Since in our research a semiconductor-based device was used to directly generate photocurrent, from now on our discussion will be focused on the semiconductor-based devices employing the direct detection mode [14].

In the next paragraphs I will focus on the X-ray detectors based on inorganic semiconductors, leaving devices based on novel material thin-films in the next chapter. The currently used direct detectors can be subsequently classified into two groups depending on the objective of an X-ray measurement. The first class are *spectroscopic* detectors, which are used to measure the energy of X-ray photons without tracking their trajectory through a material. The second group are *imaging* detectors, which are employed to depict an X-ray image (for example, of a patient's body). In this case spectroscopic detectors are usually composed of a single element, such as a photodiode or a phototransistor (discussed in detail in the next chapter). Imaging detectors, on the other hand, must be spatially multiplied into millions of pixels to obtain precise X-ray image [12].

To provide a good and reliable radiation detection response a direct semiconductor-based X-ray detector should meet the following requirements:

- A small enough band gap that would stimulate the formation of electron-hole pairs and therefore, increase the total photocurrent providing higher signal-to-noise ratio;
- A high atomic number Z for better interaction with incident X-ray radiation;
- High resistivity and low leakage current for lower noise current;
- High intrinsic mobility-lifetime $\mu\tau$ product to increase the fraction of charge carriers which successfully reach the electrodes before recombination;
- Homogeneous and defect-free medium to enhance charge transport properties;
- Electrodes that would effectively perform charge collection process and would provide a uniform electric field across the medium.

Currently the most commonly used semiconductor-based (or *solid-state*) X-ray detectors are based on inorganic semiconductors, such as silicon, germanium, gallium arsenide, cadmium telluride CdTe and cadmium zink telluride (CZT) [14], [12]. Based on these materials, different device configurations can be developed. A basic example of an imaging X-ray detector is represented by a strip reverse bias detector used in Particle Physics [15]. Its configuration is composed of numerous

small strip-like diodes integrated on the same wafer and connected to its own readout channel. The particle or a photon position is determined by the channel output signal.

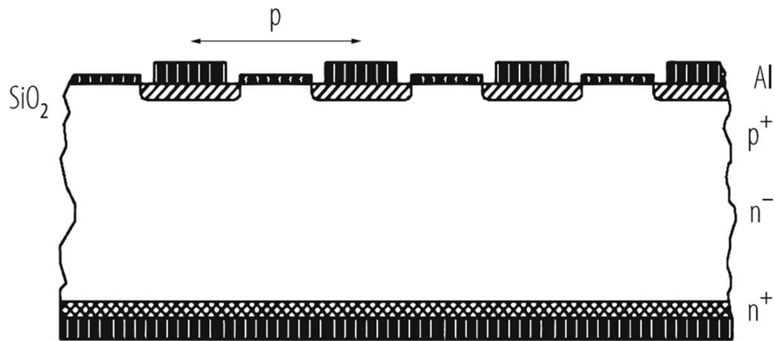

Figure 1.9 Cross section of a Si strip detector built on lightly P-doped (n-) silicon bulk material. Strips are highly B-doped (p+) and the backside is highly P-doped (n+) (Christian W. Fabjan, 2020).

Another imaging detector architecture is represented by a pixelated structure illustrated in Fig. 1.10. Here a pixelated semiconductor sensor is connected directly with a silicon readout chip with numerous solder particle array, thus, each sensor pixel is connected to a channel of readout electronics on the chip. Such design allows to acquire direct X-ray detection from each individual pixel creating a whole radiation image [12]. The hybrid pixel detector structure is of particular concern, because since the readout chip and sensor are separate, the sensor material can be freely chosen from the available range of valid semiconductor materials. It allows us to subsequently focus on commonly used inorganic semiconductors for the sensor pixel array relying on the same detector architecture [15], [12].

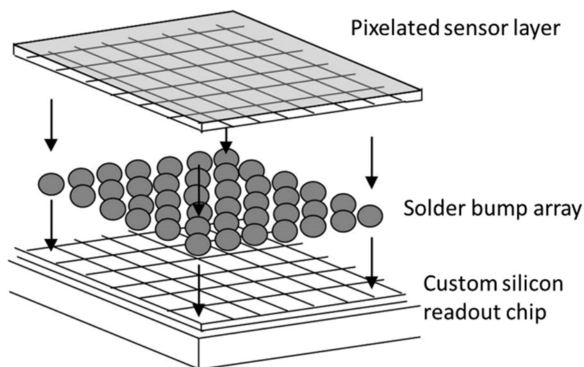

Figure 1.10 Schematic representation of the hybrid pixel detector structure. The pixelated sensor layer is connected to the readout chip with the array of solder bumps. Such structure provides output signal from an individual pixel [12].

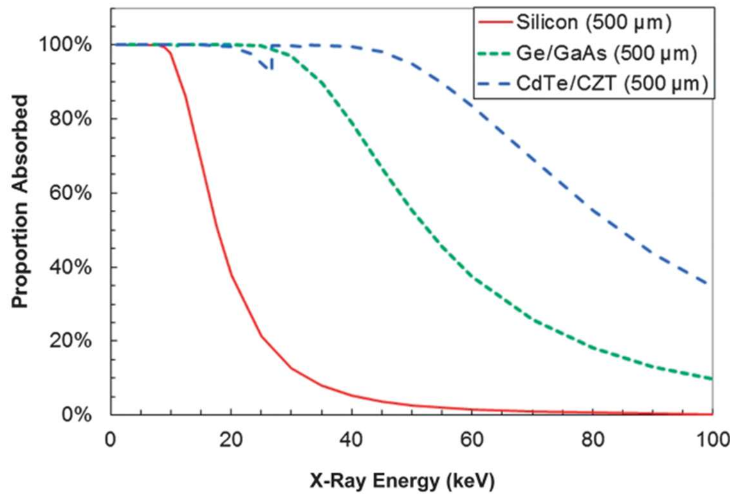

Figure 1.11 Photoelectric X-ray absorption efficiency of common sensor semiconductor materials of 500 µm thickness. The notch in the curve at 30 keV occurs because, while X-ray absorption tends to decrease with increasing photon energy, sudden increase in absorption rate occurs due to photoelectric absorption in the *K*-shell of the atoms [12].

- **Silicon**

Silicon nowadays is the major material used for semiconductor because of verified silicon wafer fabrication, near-perfect crystal homogeneity, robustness and low leakage current in a silicon *pn*-junction. The main disadvantage of the semiconductor is the low detection efficiency due to the low-Z and low attenuation fraction provided (Fig. 1.11, the red curve). For instance, in a 450 µm thick silicon sensor its absorption rate abruptly decreases from 84% to 47% from 12 keV to 17 keV [16]. This makes silicon inappropriate for X-ray measurements involving hard X-rays [12].

Efficient detection of hard X-ray photons can be achieved by using germanium, gallium arsenide GaAs, cadmium telluride CdTe and cadmium zinc telluride CZT. On the other hand, the crystal homogeneity of compound semiconductors is typically lower than for a pure element, such as Ge or Si. Besides, higher number of defects in compound semiconductors [17] might trap additional amount of charge carriers reducing significant part of photocurrent and altering the electric field applied within the semiconductor medium [18]. Consequently, fabrication of large-pixel sized X-ray detectors using compound semiconductors is limited by their less homogeneous structure.

- **Germanium**

Similarly to silicon, germanium is a single-crystal semiconductor, which can be produced using conventional methods, for example, the Czochralski pulling technique [19]. The main drawback of this semiconductor is its low band gap energy, which is below 0.7 eV at room temperature (300K) [20]. This significantly increases leakage current from thermally generated charge carriers; therefore,

an additional cooling system must be integrated to guarantee a low noise level. Normally, the temperature is reduced to 77 K through the use of an insulated dewar in which a reservoir of liquid nitrogen is kept in thermal contact with the detector [1].

The germanium-based detector working principle relies on a *pin*-diode structure [12], in which a *p*- and *n*-regions are separated by an intrinsic region to increase the depletion region [18]. The n^+ contact can be formed by diffusion of Li atoms into the wafer. The p^+ contact on the opposite site is normally made by B implantation [21].

Although bulkier and more expensive than silicon-based detectors, the single crystal germanium-based detectors, are successfully used in hard X-ray and gamma-ray measurements. Current developments in both sensor technology and readout electronics have led to more compact systems (10-mm-thick Ge layer), demonstrating energy resolutions similar to the silicon detectors, providing an alternative to silicon for a larger energy scale. A large variety of Ge sensor configurations are used for X-ray applications, depending on requirements of a specific experiment. The sensors are generally planar with thickness up to 20 mm with segmentation patterns applied in one or two dimensions (strip or pixel) [12], [21].

- **Gallium arsenide**

Gallium arsenide (GaAs) has been studied as a radiation detector since the early 1960s. It was the first compound semiconductor operated at room temperature that demonstrated sufficient gamma-ray resolution. At room temperature the band gap energy of GaAs is 1.42 eV [22], which results in low thermally generated leakage current compared to narrower band gap semiconductors, such as Si and Ge. The average ionization energy of GaAs is 4.3 eV/e-h pair [1], which indicates that acceptable energy resolution can be provided at room temperature operation. Since the atomic numbers of Ga (Z=31) and As (Z=33) bracket that of Ge, the expected X-ray and gamma-ray interactions and detection efficiency per unit mass shall be similar to germanium-based sensors. Although GaAs-based detectors output good energy resolution, electric field distortions and charge carrier trapping defects in combination with difficulty of production have prevented the mass realization of bulk GaAs spectroscopic detectors [1].

Nevertheless, due to relatively wide band gap, GaAs can be used for radiation detection in rough conditions, for example, at high temperatures and at external radiation without the need for cooling system and shielding. GaAs-based detectors are successfully employed in space missions, such as for X-ray fluorescence spectroscopy measurements on Mercury and Jupiter. Another application of GaAs is the electron spectroscopy [22].

- **Cadmium telluride**

Cadmium telluride (CdTe) is also a high-*Z* semiconductor (*Z*=48 for Cd and 52 for Te) with a sufficiently large band gap energy of 1.52 eV, which makes it appealing material for high-energy X-rays and gamma-rays detection. The probability of photoelectric absorption of gamma-rays per unit pathlength in CdTe is roughly 4-5 times higher than in Ge, and 100 times higher than in Si [1]. On the other hand, poor charge carrier properties and disparity between electrons and holes are typical of CdTe ($\mu_e\tau_e = 10^{-3}$ cm^2V^{-1} and $\mu_h\tau_h = 10^{-4}$ cm^2V^{-1}). Such low values of mobilities-lifetime products are due to the presence of impurities and defects that act as trapping sites. [23]. For example, the mean distance before trapping is on the order of 10 cm for electrons and 1 cm for electrons, which is lower than in Si and Ge [12].

Detector-grade CdTe crystals can be fabricated by first growing polycrystalline CdTe ingots from a Te-rich melt, and then progressively recrystallizing the material by the travelling heater method (THM). Using such approach, single crystal of undoped CdTe can be reliably produced [12]. Alternative growth methods may include the Bridgman technique [1]. In order to compensate crystal impurities and defects, CdTe crystals are usually doped with Cl, resulting in high-resistivity *p*-type semiconductor, while the *n*-type crystal is obtained by doping with indium (In) atoms. CdTe detectors are normally fabricated with Schottky contacts using metals with a high work function, such as gold and platinum (Fig. 1.12) [23].

CdTe with the *pn*-junction architecture exhibit low leakage current (~nA) even at applied voltage of 100 V. It means that such detectors perform high energy resolution while applying large electric fields to suppress electric field distortions caused by trapping states. However, two main disadvantages limit the success of CdTe sensors as spectroscopic detectors. The first one is called the *polarization* phenomena which represents time instability of a CdTe detector under applied voltage. The polarization phenomena lead to time degradation of the spectroscopic performance of CdTe. One of the methods to minimize the efficiency decrease is the operation of the detector at low temperatures. The second disadvantage of CdTe detectors is the difficulty of fabrication of pixelated structures with the indium electrode for imaging detectors. Aluminum has been found to be appropriate alternative as electrode in pixeled CdTe sensors without increasing leakage current [23].

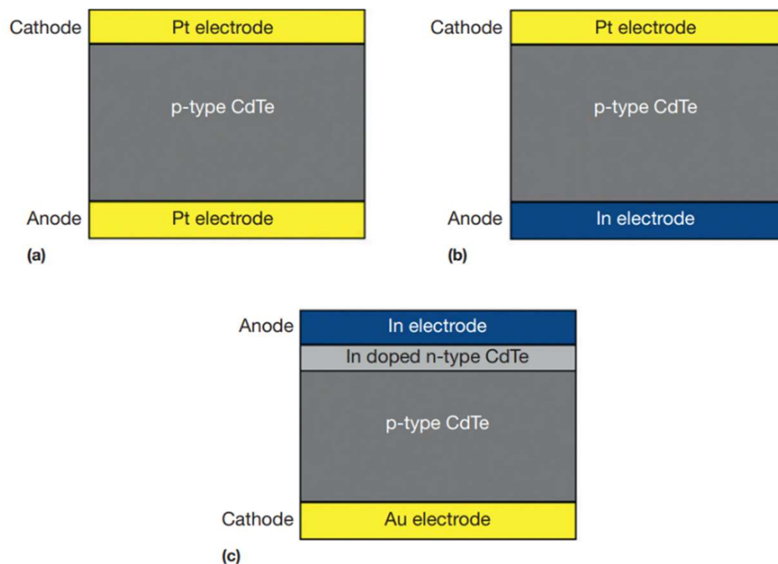

Figure 1.12 Typical CdTe detector configurations: (a) Pt/CdTe/Pt Schottky structure (ohmic contacts); (b) In/CdTe/Pt Schottky structure (rectifying contacts); (c) In/CdTe/Au *pn*-structure [23].

- **Cadmium zinc telluride**

Cadmium zinc telluride (CZT) $Cd_{1-x}Zn_xTe$ ($0<x<0.2$) is also considered a good semiconductor for X-ray detection due to its properties, such as: band gap energy of 1.5 eV sufficient to reduce thermally generated noise, thus increasing energy resolution; high atomic number (Cd(48), Zn(30) and Te(52)); absence of negative polarization effect (unlike CdTe); possibility to grow high-resistivity single crystals; relatively good charge transport properties [24]. The measured mobilities are 1350 $cm^2V^{-1}s^{-1}$ for electrons and 120 $cm^2V^{-1}s^{-1}$ for holes. Similar to CdTe, the measured lifetime of holes (50-300 ns) is much shorter than that of electrons (100 ns-10 µs) [1].

Different methods are used for CZT crystal growth. The high-pressure Bridgman technique produces large polycrystalline CZT ingots, which can then be diced to obtain single crystals of a few cubic centimeters. This can provide CZT for spectroscopic detectors, however, imaging detectors usually require larger single-crystal areas. For this purpose, the THM growth technique can be employed [12], [25].

In this section only a few commonly used inorganic semiconducting materials were described. More broad variety shall also include silicon carbide (SiC), mercuric iodide (HgI_2), diamond and other crystalline semiconductors. Even though these materials provide satisfactory performance for X-ray detection, they still suffer from numerous limitations, such as mechanical rigidity, stiffness and difficulty to grow large-scale crystalline structures, which prevents their employment onto flexible widespread substrates. This makes the inorganic solid-state detectors impossible to deposit them onto

curved surfaces making them inappropriate to some specific applications such as personal dosimetry during radiological measurements.

For this reason, scientific community is actively developing novel semiconducting materials that would provide efficient detection performance, in combination with flexibility, large-scale and low-cost production of semiconductor-based X-ray detectors. The goal of the next chapter is to provide a thorough review on specific semiconductors that are being currently examined as prominent materials for thin-film X-ray detectors.

Chapter 2 Thin-film X-ray detectors based on organic semiconductors and transition metal dichalcogenides

In previous chapter I provided a general overview on X-rays and their interaction with matter. Besides, conventional X-ray detectors based on inorganic semiconductors were briefly discussed. In this chapter I will discuss X-ray detectors based on thin-film semiconductors made by organic semiconducting small molecules and transition metal dichalcogenides (TMDCs).

First, I will discuss basic device architectures of the detectors, such as a photodiode and a phototransistor. Since the phototransistor structure was actually used in the experimental part of my research, a detailed overview on a thin-film field effect transistor and its electrical properties will also be provided.

Once the device architecture is presented, a direct X-ray detection mechanism named photoconductive gain, will be described. This mechanism is of particular interest, since it greatly enhances the sensitivity of low-*Z* organic semiconductors and more in general it rules the detection mechanism of most of the disordered microcrystalline thin film-based detectors. Finally, I will focus in detail on the two semiconductors employed as active layers in the detectors that I characterized under X-rays: 2D MoS_2 thin films and a novel organic semiconductor denoted as TMTES blended with polystyrene PS.

2.1 Device architecture of thin-film X-ray detectors

Nowadays, thin-film X-ray detectors constitute the domain that is still quite poorly studied. Different semiconducting materials are being examined to integrate in the X-ray detectors before their further pixelization into large-scale X-ray sensors. For the implementation of these materials as the active layer (also called as *absorbing layer* or *active channel*) of the detector, different architectures can be employed. Such architectures can be classified as photoconductors, photodiodes and phototransistors. Each architecture has its own different variations depending on the layer and electrode structure. In particular, the geometry of the photodetectors can be either *vertical* or *co-planar* [14]. In the vertical geometry the absorbing layer is sandwiched between two electrodes, whereas in the co-planar geometry the absorbing layer is directly exposed to the incident radiation. While the vertical geometry is convenient to use in a pixelated matrix, the latter one is easier to fabricate and does not depend on the thickness of the active channel.

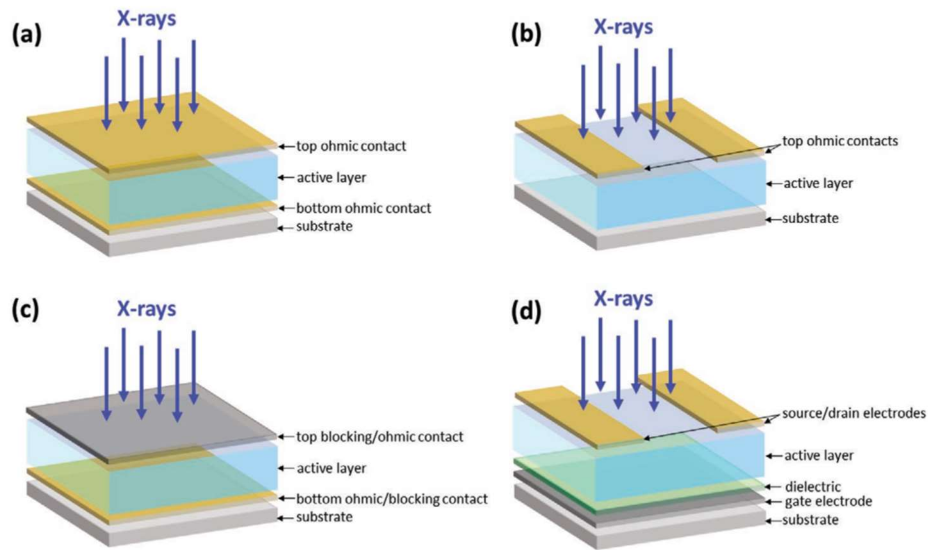

Figure 2.1 Schematics of four typical architectures for direct X-ray detectors: (a) Vertical photoconductor architecture; (b) co-planar photoconductor architecture; (c) photodiode architecture; (d) phototransistor architecture [14].

Photodiodes are vastly used, since this architecture is based on a well-known reverse biased *pn*-junction, which minimizes dark current increasing the signal-to-noise ratio. A phototransistor represents more complex structure however, it provides more freedom to tune the detector properties and to optimize them for specific conditions. Specifically, by biasing the gate electrode with voltage above the threshold value, it is possible to increase the charge carrier density in the active channel, which will enhance its performance due to so-called *photoconductive gain* mechanism, which will be discussed in the next sections [14].

2.2 Thin Film Transistors

Before discussing the X-ray detection mechanisms in the active channel of a phototransistor, it is important to first know the main electrical properties of a thin film transistor (TFT), on which a phototransistor is based on. The working principle of a TFT lies in the creation of a conductive layer with majority charge carriers (holes or electrons for *n*- or *p*-type semiconductor, respectively) between the *source* and *drain* electrodes by applying an electric field between the active channel and the *gate* electrode separated by an insulator (Fig. 2.2). Usually, the source electrode is referred to ground, thus, the gate voltage can sometimes be denoted as the gate-source voltage or V_{GS}. This is called the *common source configuration* [26]. The channel length L is the distance between the source and drain pads and the channel width W is the geometrical width of the channel.

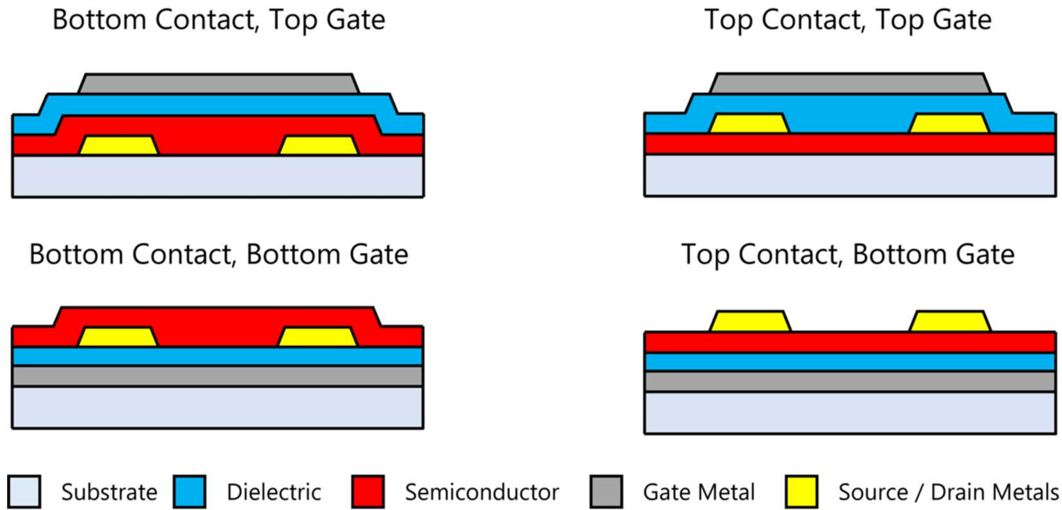

Figure 2.2 Schematic cross-section diagrams of TFTs with different configurations of the gate, source and drain electrodes. The dielectric layer always separates the gate from semiconductor acting as a planar capacitor and switching on and off a conductive channel in the semiconductor with an applied electric field [27]

A TFT is operated by switching between two modes. The OFF state is the state, in which the conductive layer is absent, thus, the active channel is highly resistive and the current I_{DS} between the drain and source is nearly zero (the contribution is only due to small leakage current through the insulator and thermally induced current between drain and source). The *accumulation* [26] mode or the ON state, is the state, in which the inversion conductive layer is formed, thus, I_{DS} starts to increase. The larger $|V_{GS}|$ is, the larger the accumulated charge density will be and thus, the larger $|I_{DS}|$ will flow between drain and source [18], [26].

2.2.1 Transfer and output characteristics of a TFT

The main electrical characteristics of a thin-film transistor are extracted from the transfer and output characteristics of the transistor (Fig. 2.3). As V_{GS} is applied, the charge accumulation near the gate is induced, however, I_{DS} does not start to increase until a *threshold* voltage $V_{GS} = V_{th}$ is reached. At this point, the conductive channel is formed and the drain-source current is non-zero. Once the current starts to flow, two regimes are possible depending on the drain-source voltage V_{DS}:

- *linear* regime: $|V_{DS}| \ll |V_{GS} - V_{th}|$
- *saturation* regime: $|V_{DS}| > |V_{GS} - V_{th}|$

In linear regime, I_{DS} follows the Ohm's law and is linearly proportional to V_{DS} at fixed V_{GS}. As $|V_{DS}|$ increases, the conductive channel becomes more depleted at the drain electrode resulting in the *pinch-off* effect. At this moment a FET is operated in the saturation regime.

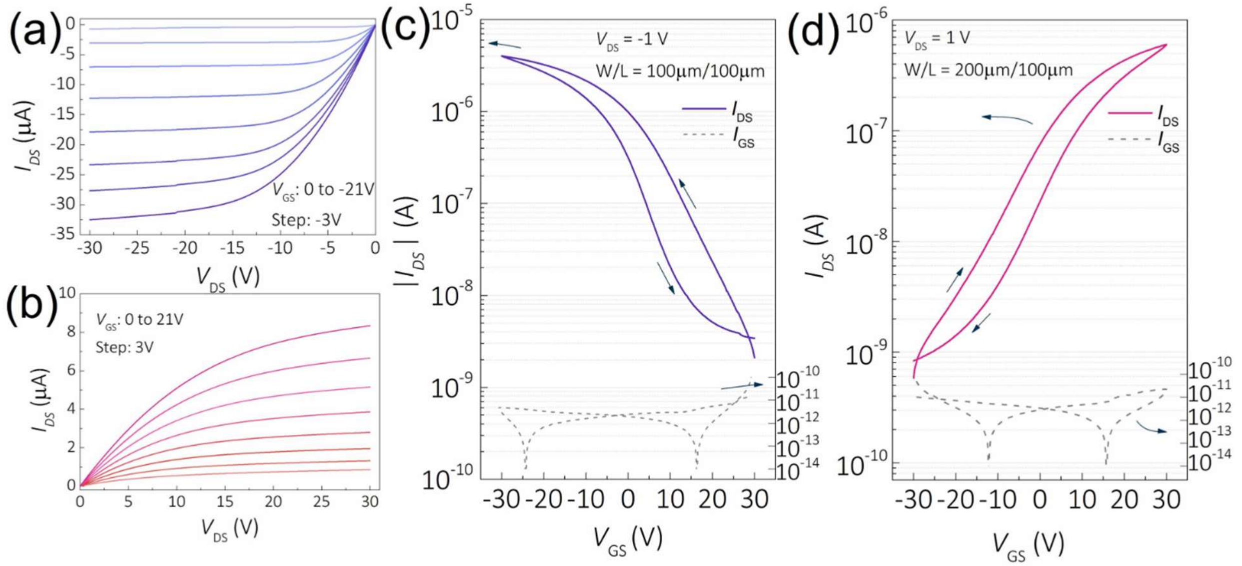

Figure 2.3 Output and transfer characteristics of *p*- and *n*-type TFTs. Output characteristics for (**a**) *p*-type SnO TFT and (**b**) *n*-type bilayer TFT; transfer characteristics for (**c**) *p*-type SnO TFT and (**d**) *n*-type bilayer TFT [28].

In the linear regime, the $|I_{DS}|$ (V_{DS}) dependence behaves according to the formula:

$$|I_{DS}| = \frac{W\mu C_i}{2L}[2(V_{GS} - V_{th})V_{DS} - V_{DS}^2] \qquad 2.1$$

or, taking into account that $|V_{DS}| \ll |V_{GS} - V_{th}|$:

$$|I_{DS}| = \frac{W\mu C_i}{L}(V_{GS} - V_{th})V_{DS}, \quad |V_{DS}| \ll |V_{GS} - V_{th}| \qquad 2.2$$

where W and L are the width and length of the active channel, respectively, μ is the mobility of the charge carriers in the conductive layer and C_i is the dielectric capacitance per unit area. In the saturation regime, $|I_{DS}|$ is almost constant (if we omit the channel length modulation effect) and does not depend on V_{DS}:

$$|I_{DS}| = \frac{W\mu C_i}{2L}(V_{GS} - V_{th})^2, \quad |V_{DS}| > |V_{GS} - V_{th}| \qquad 2.3$$

Using the $|I_{DS}|$ versus V_{GS} behaviour in saturation regime, we can calculate both the mobility μ and threshold voltage V_{th} by plotting $\sqrt{|I_{DS}|}(V_{GS})$:

$$\sqrt{I_{DS}} = \sqrt{\frac{WC_i\mu}{2L}}V_{GS} - \sqrt{\frac{WC_i\mu}{2L}}V_{th} = AV_{GS} - B \qquad 2.4$$

$$\mu = \frac{2L}{WC_i} A^2 \qquad 2.5$$

$$V_{th} = -\frac{B}{A} \qquad 2.6$$

$$C_i = \frac{\varepsilon_o \varepsilon_r}{d} \qquad 2.7$$

where d is the thickness of the insulating layer, ε_r is the relative permittivity of the insulator and $\varepsilon_0 = 8.854 \cdot 10^{-1}$ F/m is the permittivity of vacuum.

Another important electrical parameter of a TFT is the *subthreshold swing SS*, which is defined as the inverse of the slope of the $\log(|I_{DS}|)$ (V_{GS}) curve. *SS* measures the gate capability of switching the ON regime at low voltage supply from V_{GS}. Small value of *SS* indicated that just a small change of the gate voltage is required to switch ON the transistor. Supposing that in the subthreshold region I_{DS} increases exponentially, the subthreshold swing can be calculated according to the formula:

$$SS = \frac{1}{\frac{d \log|I_{DS}|}{d|V_{GS}|}} = \log(10) \frac{k_B T}{q} \left(1 + \frac{C_D}{C_i}\right) \qquad 2.8$$

where C_D is the depletion channel capacitance and q is the elementary charge [29], [30].

For an ideal thin-film transistor, $C_D \ll C_i$ in the subthreshold region and thus, *SS* is ~60 mV/dec at room temperature. However, most TFTs are fabricated on thick SiO_2 substrates as insulating layers, with large interface trap density, resulting in large *SS* values (~ a few hundred mV/dec). Although unrealistic in practical applications, also large values of C_i can be achieved by using ionic gated transistors, which reduces *SS* close to 60 mV/dec and mobility reaching close to the limitation by phonon scattering, thus, making the ionic transistors efficient to quantitatively characterize the electronic properties of 2D materials. Besides, the interfacial traps between 2D channels and SiO_2 also induce unwanted hysteresis in the transfer characteristics of a device. This can be improved by stacking or encapsulating of the 2D materials with an insulating 2D material, such as hexagonal boron nitride (hBN) [30].

The final important electrical parameter of a TFT is the ON/OFF ratio, defined as the ratio of the $|I_{DS}|$ in the ON-state and OFF-state. Typical values of the ON/OFF ratio for TFTs vary in the range of $10^6 – 10^8$ [31]. This is indicative of switching performance of the device between the conduction regimes and characterizes $|I_{DS}|$ amplification when the ON-state is induced:

$$ON/_{OFF} = \frac{|I_{DS}^{ON}|}{|I_{DS}^{OFF}|} \qquad 2.9$$

In conclusion, this section sums up the main electrical parameters of a thin-film transistor, which include the mobility of charge carriers in the conductive layer μ, threshold voltage V_{th}, subthreshold swing *SS* and ON/OFF ratio. In the experimental part, these parameters were calculated for each phototransistor used for X-ray detection and compared with the values from literature.

2.3 X-ray detection mechanism for semiconducting thin-film X-ray detectors

As was mentioned in Chapter 1, the main outcome of the interaction of X-ray photons with a semiconductor is the creation of electron-hole pairs by photoelectric absorption or Compton effect. By applying an electric field inside the semiconductor, it is possible to separate the electron-hole pairs and to collect the charges by the respective electrodes thus, measuring photocurrent. The magnitude of the maximum photocurrent can be described by the formula:

$$I_{CC} = \Phi n q \qquad 2.10$$

where q is the elementary charge, Φ is the photon absorption rate, n is the number of generated electron-hole pairs per absorbed photon. The photon absorption rate Φ can be calculated according to the Lambert-Beer equation:

$$\Phi = \Phi_0[1 - \exp(-\mu_0 t)] \qquad 2.11$$

where $\mu_0 = (\mu/\rho) \times \rho_0$ is the linear attenuation coefficient, μ/ρ is the mass attenuation coefficient of the absorbing material, ρ_0 is the absorber density, t is the interaction length within the material and Φ_0 is the incident photon flux [14].

2.3.1 Charge collection and Photoconductive gain

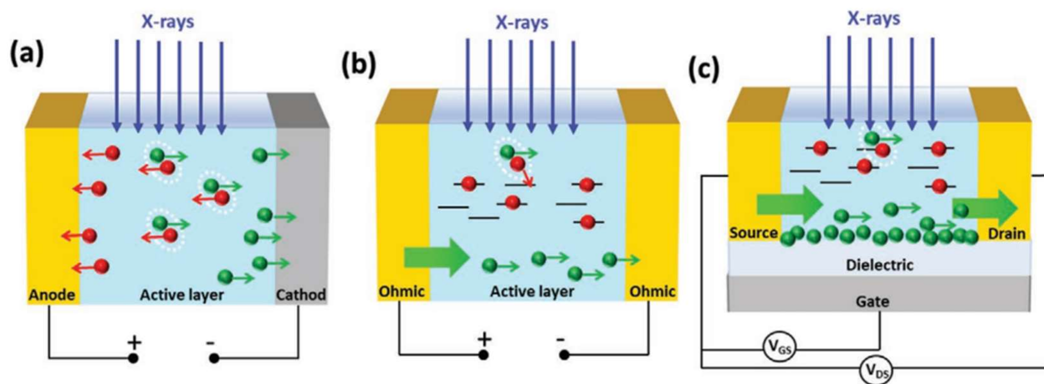

Figure 2.4 Schematics for the direct X-ray detection processes: (**a**) Charge collection in photodiode architecture; (**b**) Photoconductive gain in photoconductor architecture; (**c**) Photoconductive gain in phototransistor architecture [14].

For semiconductors exhibiting a significant number of traps for minority charge carriers, the X-ray detection mechanism includes two simultaneous processes (Fig. 2.4). Charge collection was

already introduced in Chapter 1 regarding X-ray detectors based on inorganic semiconductors. Similarly for organic semiconductors, when X-ray radiation directly impinges on the active channel, X-ray photons create electron-hole pairs, which are then separated by an applied electric field and thus, additional charge carriers are collected by the electrodes. In order for the charge carriers to reach the collecting electrodes, it is important that the recombination time is sufficiently high and that the density of traps is low. Consequently, charge collection mechanism is dominant for 2D organic semiconductors of high purity and homogeneity [14].

The second mechanism introduces *photoconductive gain* (Fig. 2.4(b, c), Fig. 2.5) and occurs along with the charge collection process. This mechanism amplifies the photogenerated current by the factor G, leading to the photo-to-electrical efficiency exceeding 100 % and providing high sensitivity to the X-ray radiation. Photoconductive gain mechanism occurs when radiation-generated, free charge carriers accumulate and pass several times through the semiconductor active channel before recombination sets in. This amplification process is activated by the trapping of minority charge carriers during their migration in the semiconductor under the applied field. The factor G can be expressed as the ratio between the recombination time τ_r – characteristic of the trap states, and the transit time τ_{tr} of free moving carriers:

$$G = \frac{\tau_r}{\tau_{tr}} = \frac{\mu V \tau_r}{L^2} \qquad 2.12$$

where L is the channel width, μ is the charge carrier mobility and V is the applied bias across the active channel. τ_r and τ_{tr} represent respectively the time of recombination of the *minority* charge carriers trapped in the active layer, that is, the minority carrier lifetime in a trap, and the transit time of the *majority* carrier to travel across the active channel of the detector [14].

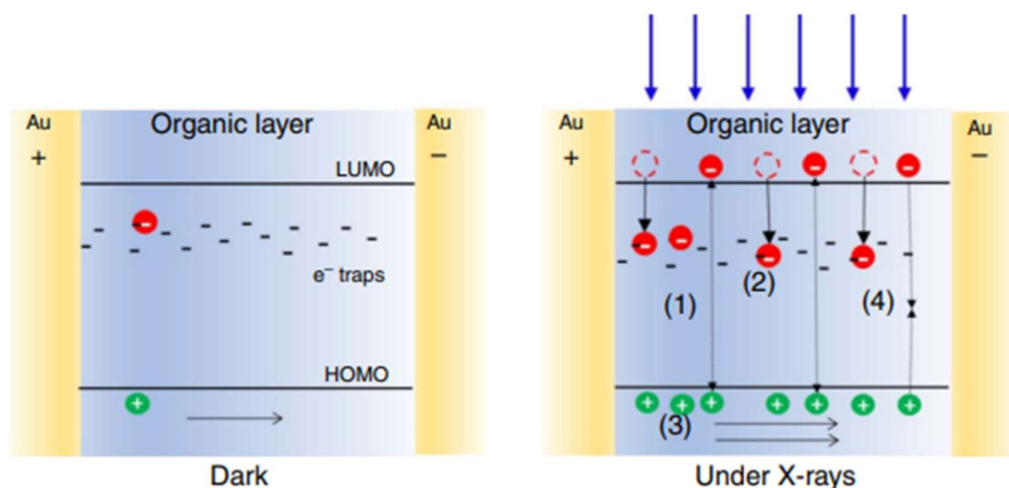

Figure 2.5 Schematics of the process of modulation of the conductivity induced by X-rays exposure of TIPS-pentacene thin films: (***left***) in the dark (absence of X-rays) the conductivity is due to the intrinsic carriers; (***right***) under X-ray radiation: (**1**) additional electrons are generated; after generation holes drift along the electric field until they reach the collecting electrode while (**2**) electrons remain trapped in deep trap states withing the organic material. (**3**) To guarantee charge neutrality, holes are continuously emitted from the injecting electrode. AS a consequence, for each electron-hole pair created, more than one hole contributes to the photocurrent leading to the photoconductive gain effect. (**4**) Recombination process takes place, counterbalancing the charge photogeneration in the steady-state [32].

The photoconductive gain mechanism has been proposed to interpret high sensitivity in thin-film organic photoconductors based on solution processed bis-(triisopropylsilylethynyl)pentacene (TIPS-pentacene) and derivatives [32]. As was mentioned in Chapter 1, the cross-section of photoelectric absorption is proportional to Z^n, where $4 < n < 5$, as well as Compton scattering is linearly proportional to Z. As a result, materials with high atomic number Z perform more efficient interaction with X-ray photons and therefore, possess high sensitivity. On the other hand, organic thin-film X-ray detectors are based on semiconductors with both low atomic number and interaction volume, which leads to extremely low absorption of X-rays.

Approximately 0.0015 % of incident radiation was absorbed by 100 nm thick TIPS-pentacene films. As a result, due to low photon absorption, the obtained photocurrent was calculated to be $|I_{CC}^{max}| < 2$ pA. At the same time, the observed photocurrent was about two orders of magnitude higher than the theoretical value [32]. It means that some amplification mechanism must be involved.

Since TIPS-pentacene is a p-type semiconductor, a different behaviour can be assumed for photogenerated holes and electrons. Holes drift along the active layer reaching the collecting electrode, while electrons get trapped and act as "doping centers". Due to the ohmic nature of the electrical contacts, charge neutrality is sustained in the active channel. Therefore, for each hole collected by the electrode, another hole is injected in the channel. As a result, for one electron-hole

pair created, more than one hole contributes to the X-ray induced photocurrent before recombination takes place. Such amplification phenomenon results in the photoconductive gain [14].

Besides photoconductors, phototransistors based on organic semiconductor thin films have also been demonstrated to detect X-rays with high sensitivity due to enhancement of the photoconductive gain effect through the gate polarization (Fig. 2.4(c)). As mentioned in the previous section, the gate voltage sweeps to progressively switch on the conductive channel in the transistor, that is, towards more negative/positive values of V_{GS} for *p*-type/*n*-type semiconductor, the charge density in the transistor's active channel increases, leading to the enhancement of minority carriers accumulation and majority carriers conduction. Furthermore, majority charge carriers are more easily injected from the electrodes due to the lowering of the contact resistance. Therefore, in over-threshold condition τ_{tr} decreases, which leads to the increase of the photoconductive gain [14].

2.4 X-ray Sensitivity

As was discussed in previous sections, an X-ray detector's efficiency performance is determined by numerous parameters, such as the atomic number Z of the semiconductor, its band gap energy and bulk resistivity. Nonetheless, from a technological standpoint, hereafter our attention focuses on the *sensitivity* of the detector. This parameter will further serve as the benchmark for evaluation of the efficiency of our device.

The sensitivity of an X-ray detector is denoted by S and characterizes the ability of a detector to react to certain amount of X-rays by generating photocurrent in the active channel. Although there are several formulas describing sensitivity, the basic method to calculate S is based on the dependence of photocurrent I_{PH} on dose rate DR. First, one has to measure the photocurrent created by incident X-rays with certain dose rate. Typically, the photocurrent is the difference between the current I_{DS}^{X-ray} across the active channel during X-ray radiation and the current I_{DS}^{dark}, when the radiation is absent. The entity of dose rate is the amount of X-ray radiation energy per unit mass of the absorber material and per unit second of irradiation. Then, once several values of I_{PH} at different DR are obtained, the resulting plot is fitted with linear function. Finally, sensitivity is defined the derivative, of the linear plot [14]:

$$S = \frac{dI_{PH}}{dDR}, \quad I_{PH} = I_{DS}^{X-ray} - I_{DS}^{dark} \qquad 2.13$$

However, often it is more convenient to study the sensitivity of a thin-film detector without being tied to the geometry of the active channel and with focusing only of the semiconductor properties. In this case, it is common to calculate sensitivity per unit area or per unit volume of the active channel:

$$\frac{S}{Area} = \frac{1}{A} \cdot \frac{dI_{PH}}{dDR} \quad 2.14$$

or:

$$\frac{S}{Volume} = \frac{1}{V} \cdot \frac{dI_{PH}}{dDR} \quad 2.15$$

where A and V are the respectively area and the volume of the active channel. The SI unit of photocurrent is $[I_{PH}] = A = {C}/{s}$, the SI unit of dose rate is $[DR] = {Gy}/{s}$, therefore the SI unit of sensitivity is $[S] = \frac{[I_{PH}]}{[DR]} = \frac{C}{Gy}$. For the case of sensitivity per unit area or unit volume, the unit is usually expressed as: $\left[\frac{S}{Area}\right] = \frac{C}{Gy \cdot cm^2}$, $\left[\frac{S}{Volume}\right] = \frac{C}{Gy \cdot cm^3}$.

It is noteworthy to mention that dose rate is inversely proportional to the square of distance r from an X-ray source:

$$DR = \frac{const}{r^2} \quad 2.16$$

Consequently, while using an X-ray source for measuring the sensitivity of a thin-film detector, the dose rate must be properly calibrated accordingly to the distance between the X-ray source and the device. For example, if one knows the dose rate DR_1 at distance r_1 from the source, the dose rate DR_2 at distance r_2 can be calculated as follows:

$$DR_2 = DR_1 \cdot \left(\frac{r_1}{r_2}\right)^2 \quad 2.17$$

2.5 Organic and hybrid semiconductor-based X-ray detectors: State of the Art

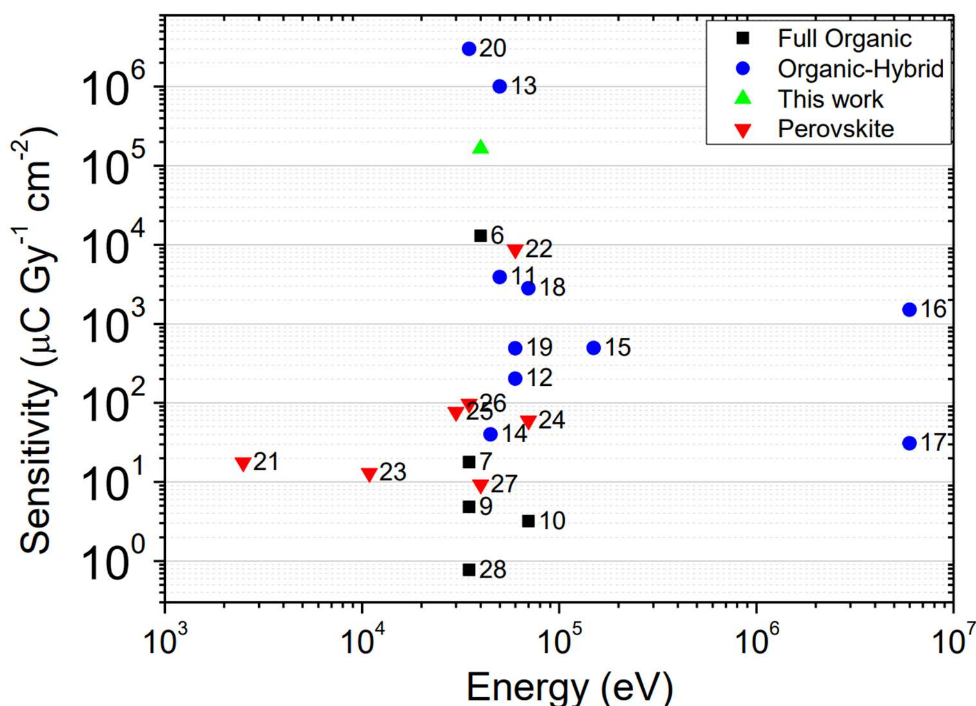

Figure 2.6 Comparison of top sensitivity for organic, hybrid semiconductor and perovskite-based detectors [33].

To estimate the performance of different thin-film direct X-ray detectors, from large multitude of organic and hybrid semiconductors we will regard several materials that are currently under investigation. When it comes to thin-film photovoltaics, among the most prominent are perovskite-based X-ray detectors. Recent studies on such devices have been primarily concentrated on identifying technological approaches to improve film thickness, specifically radiation absorption, at the same time ensuring a sufficient μτ product to uphold optimal charge collection efficiency. The highest sensitivity reported for a perovskite-based detector was found to be 1.22×10^5 μC/(Gy·cm^2) for a 800 μm thick $MAPbI_3$ wafer fabricated by a heating-assisted press method [34].

Another example of a direct thin-film organic X-ray detector is based on bis-(triisopropylsilylethynyl)pentacene (TIPS-pentacene) with the photoconductor architecture. The device was fabricated while drop casting onto flexible poly(ethyleneterephtalate) (PET) substrate. While biasing the X-ray detector with 0.2 V, the highest sensitivity value was evaluated as 77×10^3 nC/(mGy·cm^3) [32]. On the other hand, in [35], TIPS-pentacene blended with polystyrene organic field effect transistors (OFETs) were used as X-ray detectors and exhibited the one of the highest (for

the time of publication) sensitivities reported among organic X-ray detectors of 1.3×10^4 μC/(Gy × cm^2) while being biased at V_{SD} = -20 V and V_{GS} = -15 V.

Regarding hybrid semiconductors, in [36] a thin-film direct X-ray detector with the photodiode architecture was made of hybrid semiconductor consisting of organic bulk heterojunction (BHJ) of poly(3-hexylthiophene-2,5-diyl) (P3HT) and [6,6]-Phenyl C_{71} butyric acid methyl ester ($PC_{70}BM$), blended with nanoparticles (NPs) of Bi_2O_3 to increase the attenuation fraction of the active layer. The X-ray source was a medical linear accelerator. The sensitivity of such devices was estimated to be 1712×10^3 μC/(Gy × cm^3) under 50kV soft X-rays and ~30×10^3 and ~60×10^3 μC/(Gy × cm^3) under 6 and 15 MV hard X-rays, respectively. The sensitivities were obtained at -10 V applied to the photodiode.

2.6 Overview on X-ray detectors based on TMTES:PS

In some works previously reported in literature [35], regarding X-ray detectors in the form of *p*-type organic field effect transistors (OFETs) based on TIPS-pentacene blended with polysterene (PS), the devices already demonstrated excellent sensitivity comparable to the perovskite-based detectors. The organic semiconductor (OSC) thin films were fabricated by the solution shearing technique of high processing capacity, known as the *bar-assisted meniscus shearing* (BAMS) (Fig. 2.8) method, which outputs large scale crystalline films. In the reported study, it was concluded that the organic-based detector efficiency strongly depends on the grain size and grain boundaries and also on the mobility of the active channel. Regarding the former in combination with photoconductive gain mechanism, films with smaller crystal domains exhibited better performance due to increase of the density of traps for minority charge carriers (in case of TIPS-pentacene electrons are the minority carriers), which enhanced photoconductive gain and thus, sensitivity. At the same time, the active channel mobility can be improved by reducing the density of traps for the majority charge carriers (for TIPS-pentacene, holes are the majority carriers). The density of traps for majority carriers generated at the dielectric/semiconductor interface can be decreased by using OSC:PS blends, as thin film deposition induces vertical phase separation, creating a lower PS layer that passivates the interfacial majority carriers traps and again, enhances the majority charge carrier mobility also contributing to the sensitivity [32], [33]. In fact, while acting on the density of minority carriers density enlarges the τ_r, working on the transport properties and the mobility allows to reduce τ_{tr}. The combination of these two approaches improves the gain factor as discussed in the previous section.

Another approach to enhance the performance of the X-ray detector is based on the improvement of the semiconductor hole transport properties. For this purpose, a similar *p*-type OSC 1,4,8,11-tetramethyl-6,13-triethylsilylethynyl pentacene (TMTES) blended with PS was analyzed.

The molecular structure of TMTES closely resembles that of TIPS-pentacene (Fig. 2.7). Nevertheless, thin films of TMTES deposited with the BAMS method resulted in completely different crystal packing arrangement, characterized by a herringbone packing motif. The PS implementation reduced the density of traps for majority charge carriers present at the dielectric interface, which led to the mobility improvement. Furthermore, the TMTES semiconductor possesses stronger intermolecular packing compared to the TIPS structure, which also enhanced μ. As a result, the density of traps was reduced due to the PS layer, which led to the enhancement of the mobility up to 2.5 $cm^2/(V \cdot s)$. The new device performed outstanding sensitivity of $(4.5 \pm 0.05) \times 10^{10}$ $\mu C/(Gy \cdot cm^3)$, which exceeded that of TIPS-pentacene detector by one order of magnitude. Consequently, the sensitivity of the TMTES:PS device was reported to be the highest of a fully organic X-ray detector [33].

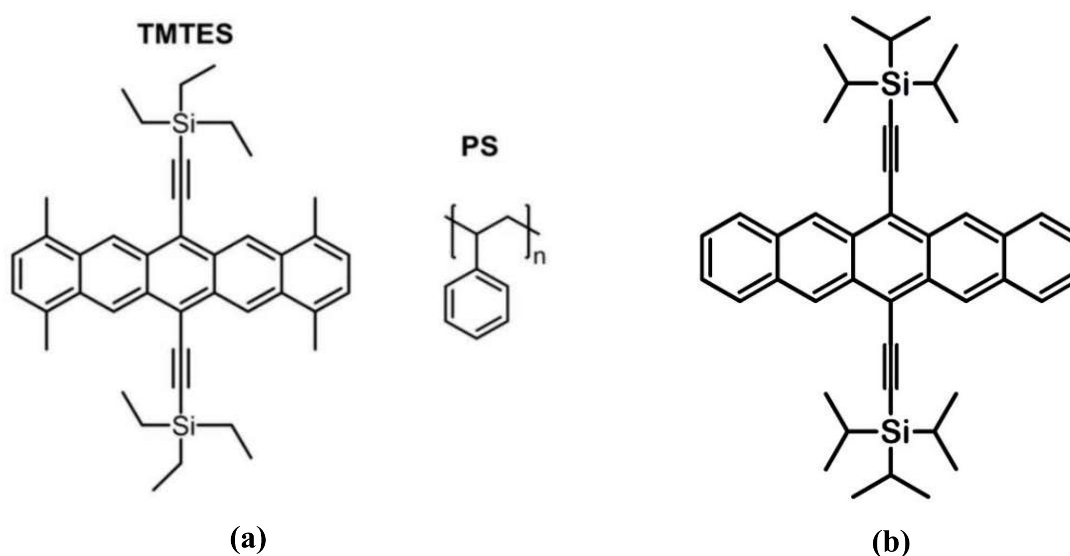

Figure 2.7 (**a**) Molecular structure of TMTES and PS [33]; (**b**) Molecular structure of TIPS-pentacene [37].

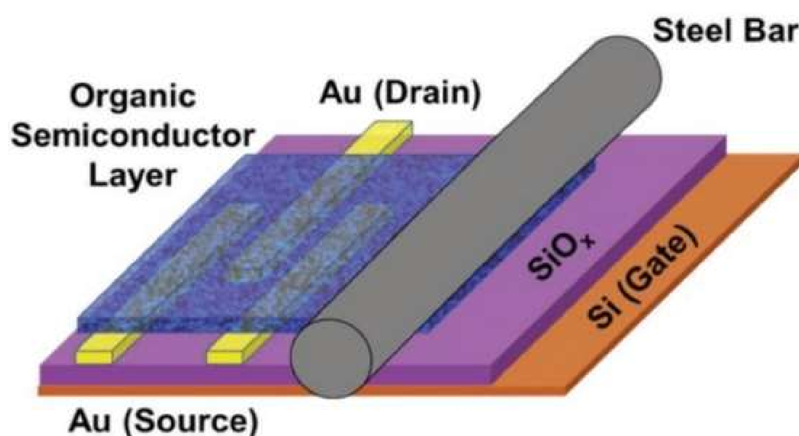

Figure 2.8 Schematics of the BAMS technique for the deposition of the active layer [33].

Since the experimental part of our research regarding TMTES:PS X-ray detectors will be also compared to the results from this work [33], it is important to transmit more in detail the conditions in which the TMTES:PS based devices were characterized. Ambient conditions were sustained during the thin film deposition by BAMS. It was found that the use of combination of small molecule OSCs blended with insulating polymers can ease the solution processability resulting in thin films with improved electrical performance and device stability. The selection of PS as a binding polymer was based on its low relative permittivity, good solubility in organic solvents, cost-effectiveness and its weak interaction with organic semiconductors. Different ratios between TMTES and PS were considered during the TMTES:PS thin film preparation. As a result, the finest thin film properties were attained by using a 2:1 ratio of TMTES to PS (PS with a molecular weight of 280 KDa). The solution was deposited at 105 °C on Si/SiO_2 substrates with interdigitated Au electrodes treated with a self-assembled monolayer of 2,3,4,5,6-pentafluorobenzenethiol (PFBT). The thickness of the TMTES:PS films was estimated as 32±7 nm [33].

In order to view the chemical map of the TMTES:PS thin films, Time-of-Flight Secondary Ion Mass Spectroscopy (ToF-SIMS) was applied for both horizontal and vertical dimensions. As a result, no horizontal phase separation was observed. At the same time, during vertical profiling, the signal from TMTES notably decreased, whereas the PS ion signal increased, exhibiting larger concentration of PS molecules closer to the SiO_2 substrate [33].

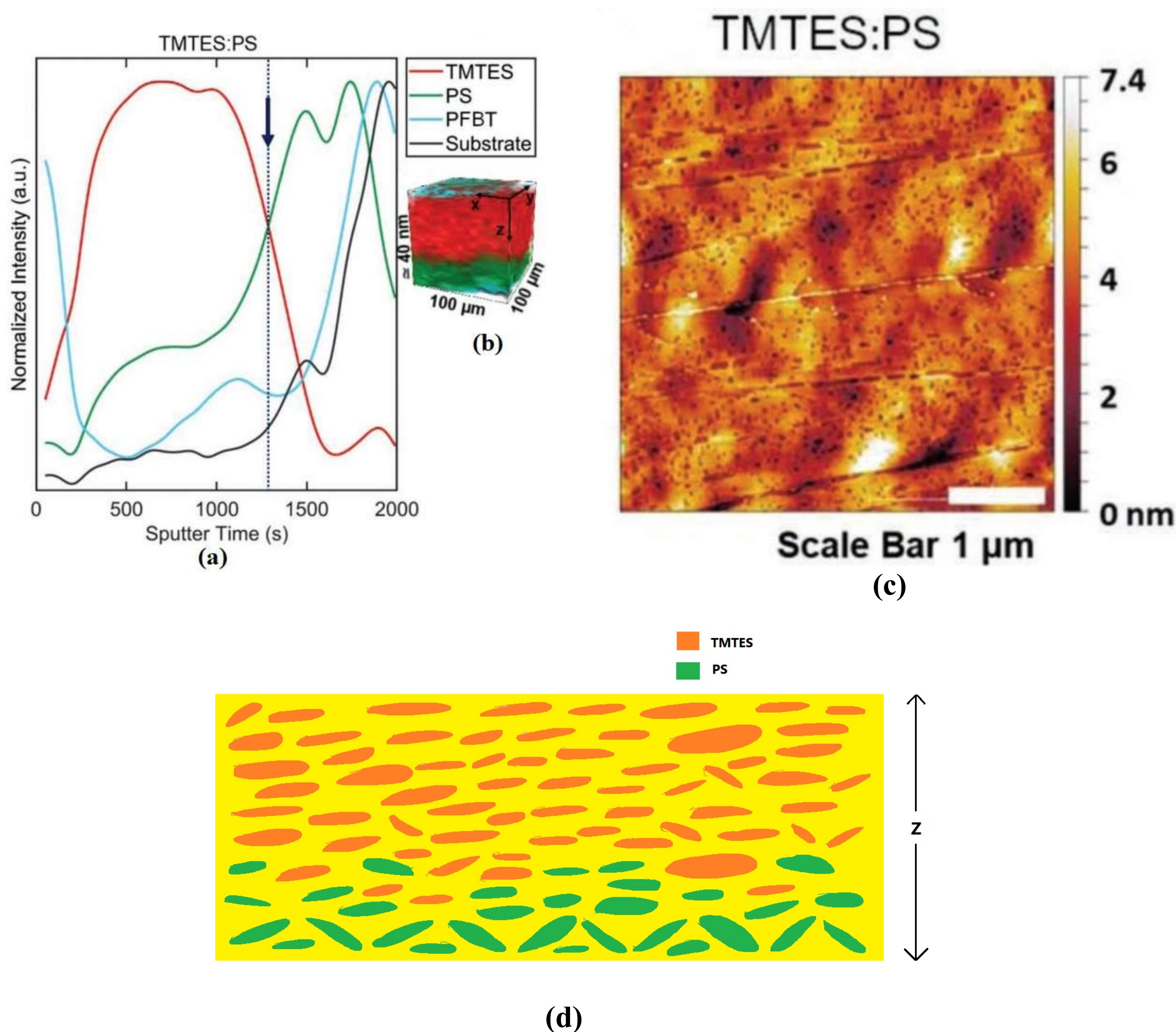

Figure 2.9 (**a**) ToF-SIMS study of the TMTES:PS thin films. Normalized (to maximum) ToF-SIMS depth profile obtained in the active channel area of the OFET starting from the surface and reaching the SiO_2 substrate (black curve). The TMTES signal (red curve) includes the SiC^-, $SiCH^-$, SiC_2H^-, $SiC_5H_2^-$, $SiC_7H_2^-$ species; the PS signal (green curve) includes the $C_3H_3^-$,$C_4H_3^-$,$C_5H_3^-$,$C_6H_3^-$, $C_7H_3^-$ species; the PBFT signal (light blue curve) includes the F^- and S^- species. (**b**) 3D rendering of the same species of the (**a**) panel, as the sputter time is proportional to Z-profiling of the layers. The analyzed thickness (40±12 nm) was multiplied by a factor 2.5×10^4 to better appreciate the multilayer architecture in the 3D rendering. Dashed line and arrow indicate the TMTES:PS transition region. (**c**) AFM topography image of a TMTES:PS thin film [33]. (**d**) Simplified vertical cross-section of a TMTES:PS thin film. PS molecules (green) are concentrated at the bottom, while TMTES (orange) are located in the top part of the film.

Both TMTES and TMTES:PS thin films underwent electrical characterization under ambient conditions as active layers in OFETs. As a result, OFETs with TMTES:PS as the active layer exhibited better performance compared to those based solely on TMTES. The former operated within a lower voltage window of 5 V and displayed excellent electrical characteristics with reduced hysteresis and significantly less dependence of the mobility on V_{GS}. The threshold voltage V_{TH} for TMTES:PS based devices approached 0 V (ranging from -0.5 to -1 V), providing further evidence of benefit of using

PS together with the semiconductor. Additionally, the density of traps for the majority charge carriers (in this case holes), was estimated to be (3.9±0.9) × 10^{11} e/(V·cm^2), which is one order of magnitude lower than that for the TMTES films (~10^{12} e/(V·cm^2)). This observation confirms that adding the insulting PS to TMTES compound results in reduction of interfacial traps for majority charge carriers [33].

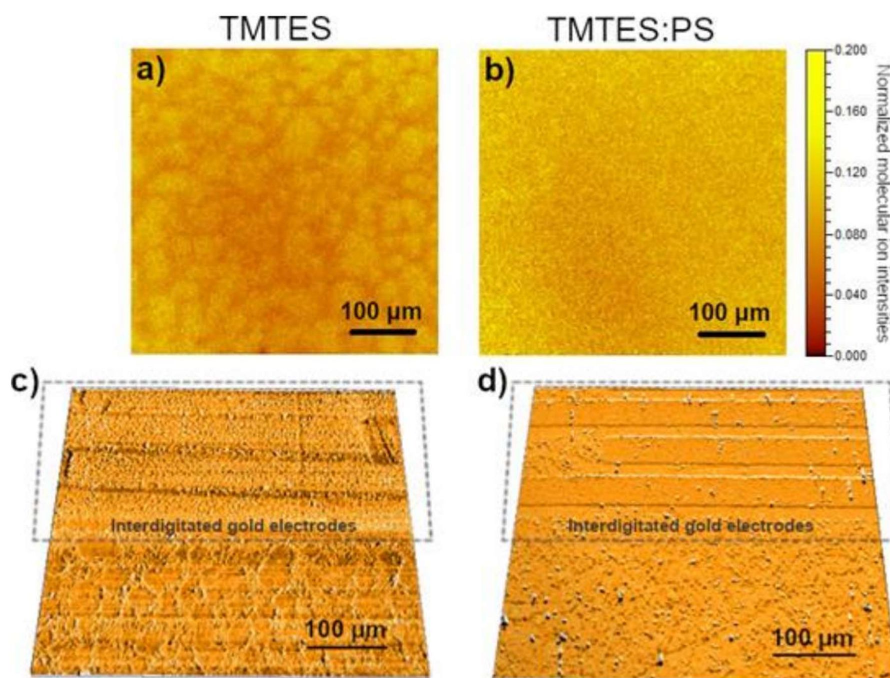

Figure 2.10 ToF-SIMS 2D surface chemical maps of TMTES and TMTES:PS thin films deposited by BAMS at high coating speed. Normalized (to total counts) sum of $Si_2C_{42}H_{50}^+$ (m/z = 610.34), $Si_2{}^{13}CC_{41}H_{50}^+$ (m/z = 611.35), $Si_2{}^{13}C_2C_{40}H_{50}^+$ (m/z = 612.35), $^{30}SiSi^{13}CC_{41}H_{50}^+$ (m/z = 613.34), $^{30}SiSi^{13}C_2C_{40}H_{50}^+$ (m/z = 614.35), and $^{30}SiSi^{13}C_3C_{39}H_{50}^+$ (m/z = 615.35) secondary ion signals from (**a**) TMTES and (**b**) TMTES:PS surface acquired outside the interdigitated electrodes. 3D surface height profiles maps of (**c**) TMTES and (**d**) TMTES:PS films with the interdigitated gold electrodes [33].

Finally, detectors based on TMTES:PS exhibited a notably high average mobility of 2.6 ± 0.6 cm^2/(V·s) with the maximum value of 3.1 cm^2/(V·s). Such mobility values in combination with previously mentioned electrical characteristics of TMTES:PS thin films rank among the best reported for this semiconductor. It is noteworthy that the films were fabricated using a low-cost and high throughput BAMS technique which is a significant advantage in terms of mass production [33].

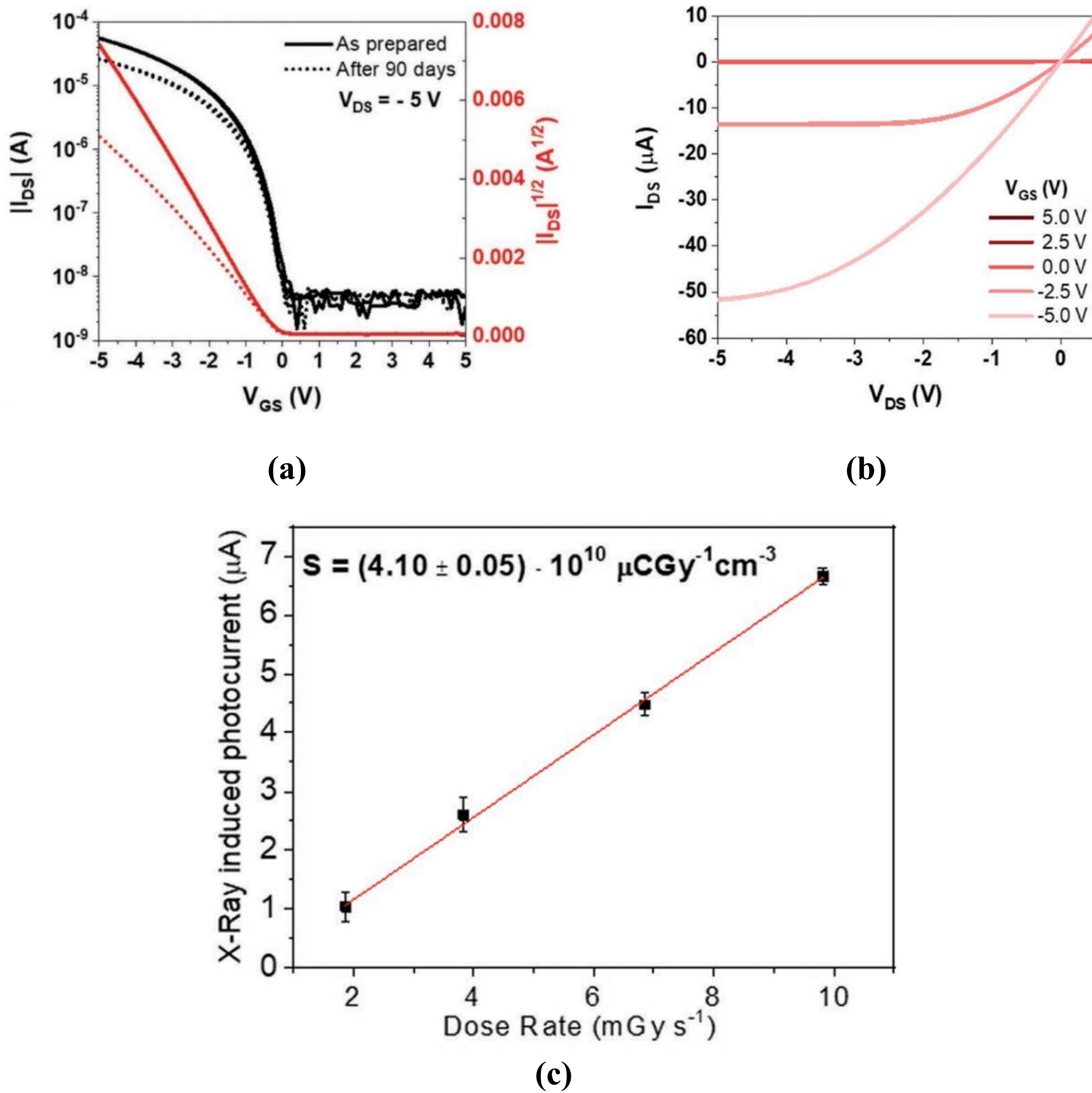

Figure 2.11 Electrical and X-ray performance of the TMTES:PS based OFETs. (**a**) Transfer characteristics in saturation regime; (**b**) output characteristics; (**c**) X-ray induced photocurrent as a function of the dose rate. The sensitivity is calculated as the slope of the linear fit of the experimental points [33].

Such remarkable electrical properties of TMTES:PS based OFETs deposited by the BAMS technique allowed to presume these devices to perform efficiently as X-ray detectors. For this purpose, the sensitivity of the TMTES:PS based OFETs was measured under X-ray in the form of periodic pulses (on/off beam switches) of different dose rate. During the X-ray exposure, the devices were biased to operate in saturation regime (V_{DS} = -15 V and V_{GS} = -20 V). The current I_{DS} flowing between the source and drain was measured during the on/off beam switching cycles. The photocurrent was measured as the difference between the values of I_{DS} during X-ray radiation and in the dark. The resulting signal was amplified by the photoconductive gain effect (discussed in previous

sections), which occurs due to minority carriers traps and which allows low-Z thin-film organic semiconductors to perform high sensitivity. According to its definition, the sensitivity of TMTES:PS based OFETs was calculated as the slope of the linear fit to the dependence of the photocurrent $|I_{PH}|$ on the X-ray dose rate. By these calculations, the sensitivity of the TMTES:PS based detectors was estimated as $(4.10 \pm 0.05) \times 10^{10}$ μC/(Gy·cm^3). Such value was considered as the highest sensitivity value documented for an X-ray detector based on fully organic active layer, which also surpassed the sensitivity of the majority of the sensors based on perovskite films. Additional advantage of the TMTES:PS based detectors in comparison with those based on lead-halide perovskites, is that it fully matches human tissue equivalent absorbance of ionizing radiation. This feature paves the way for TMTES:PS based X-ray imaging detectors in numerous medical dosimetry applications [33].

2.7 Overview on 2D transition metal dichalcogenides

2.7.1 Crystal structure and energy gap

Recently great attention has been drawn by 2D transition metal dichalcogenides (TMDCs) in the thin-film optoelectronics field. TMDCs compose a large class of inorganic layered materials, which perform a variety of different electronic properties from semiconductivity to superconductivity, which makes TMDCs quite perspective materials for nanoelectronics, thin-film flexible electronics and power conversion domain [38], [39].

TMDCs have the **MX_2** stoichiometry, where M stands for a transition metal (M = Mo, W, Ti, Nb etc.) and X means a chalcogen (X = S, Se, Te etc.). The general structure of a TMDC represents a sandwich-layer structure, in which a layer of transition metal atoms is placed between two layers of hexagonally packed chalcogen atoms, thus, forming a periodic **X-M-X** layer order (Fig. 2.12). The bulk crystal of TMDC consists of the X-M-X layers bound together with weak van der Waals forces. [38], [40].

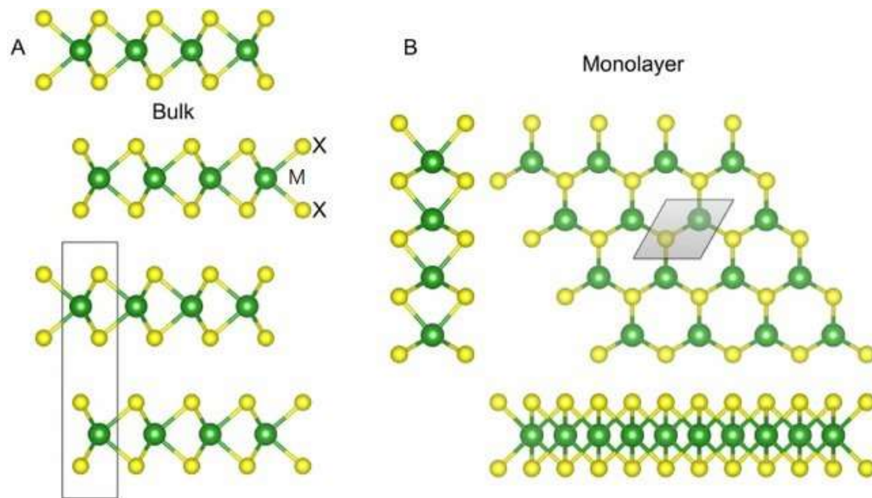

Figure 2.12 The atomic structure of TMDCs of 2H polytype. M stands for a transition metal, X signifies chalcogenide. In (**A**) a bulk structure with its unit cell (indicated by a rectangle) is depicted. In (**B**) a monolayer structure is depicted by an X-M-X layered configuration. Distinct monolayers are bound together into a bulk structure by van der Waals forces [41].

Among the diverse multitude of different TMDC compounds, our attention shall now focus on **MoS_2**, which is particularly attractive for the field of thin-film electronics. The crystal structure of MoS_2 can be categorized into four polytypes, depending on the atomic stacking configurations: 1H, 1T, 2H and 3R (Fig. 2.13). The 2H-polytype is thermodynamically favoured by naturally occurring bulk MoS_2 and represents the S-Mo-S layers stacked in hexagonal symmetry (from the top view) with each Mo atom covalently bonded with neighbouring six S atoms [38]. In contrast, in the 1T-polytype, which is metastable [42], forms a tetragonal symmetry with an octahedral metal coordination, as the layers are offset from each other. The 2H-MoS_2 structure exhibits semiconducting properties, whereas the 1T-MoS_2 is metallic. The metastable 1T-MoS_2 can be readily transformed to 2H phase via intralayer atomic gliding under specific conditions [38] [43].

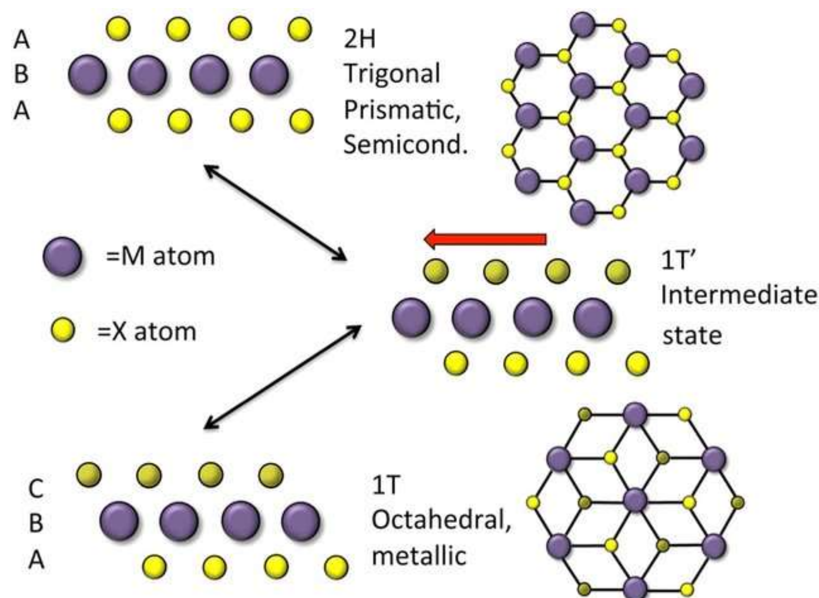

Figure 2.13 Schematics of the 2H- and 1T-polytypes of MoS_2. the 2H phase is trigonal prismatic and the material behaves as a semiconductor. The 1T phase is octahedral and the material is metallic. The 1T' phase represents an intermediate state [44].

Recent progress in the characterization of nanoscale materials has created new possibilities to thoroughly study the electrical and optical properties of 2D TMDCs by means of computational modelling tools. Utilizing the first-principle density functional theory (DFT), it has become possible to calculate the band structure of MoS_2 both as bulk and as a monolayer (Fig. 2.14).

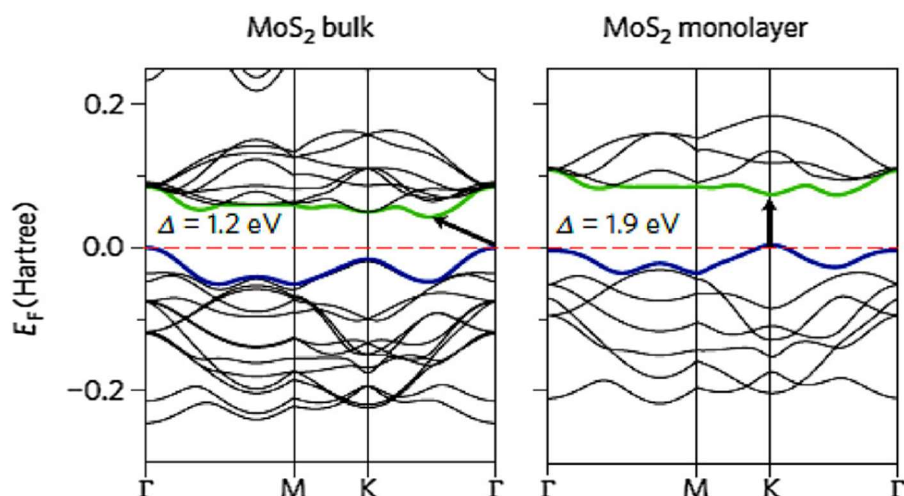

Figure 2.14 Band structures for bulk and monolayer MoS_2 calculated with the first-principles DFT. The pointer indicates the band gap (direct for monolayer and indirect for the bulk), the red dashed lines indicate the Fermi level. The top of the valence band and the bottom of the conduction band are highlighted in blue and green, respectively [38].

As a result, it was revealed that the MoS_2 crystal possesses an indirect band gap of 1.9 eV at the Γ-point. While decreasing the number of layers for MoS_2, the band gap energy gradually decreases, thus, in a monolayer MoS_2 the band gap is direct and it has the value of 1.2 eV.

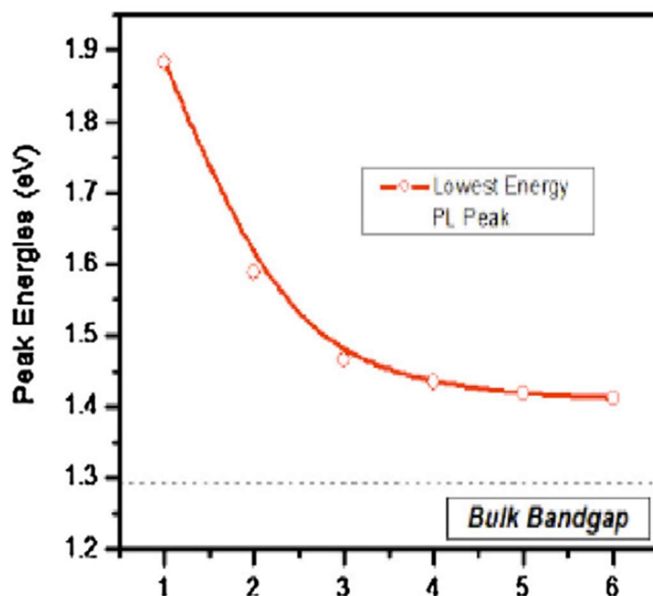

Figure 2.15 Band gap energy of MoS_2 as a function of layers. the dashed line shows the (indirect) band gap energy of bulk MoS_2 [38].

2.7.2 Fabrication methods of 1L-MoS_2

Before discussing the role of 1L-MoS_2 as an active layer in X-ray detector, it is of good practice to first regard different fabrication methods of the monolayer, which typically include mechanical exfoliation, chemical vapour deposition, RF sputtering and various liquid phase preparations.

- **Exfoliation method**

The mechanical exfoliation (ME) technology involves the "peeling" or "cleaving" of bulk crystals by using an adhesive tape or rubbing the crystals against a solid surface. As a top-down technique, ME has been widely applied to produce single- or few-layer MoS_2 (and TMDCs in general) thin films from their bulk counterparts. As previously mentioned, in TMDCs layers are bonded together along the vertical axis with weak van der Waals forces, which allows to perform easy exfoliation due to weak interlayer forces. Consequently, the ME technique can be used to produce a few-layer MoS_2 film with thickness of approximately 3-10 nm. Nevertheless, while ME enables the fabrication of clean and high-quality MoS_2 thin films, this method is limited to research purposes only is not applicable to large-scale production [38].

Beside the mechanical method, a thermally activated metal-mediated exfoliation method is available. The fundamental concept behind this exfoliation technique lies in the cleaving a parent MoS_2 crystal onto a metal surface by overcoming van der Waals interlayer forces, such that the bottom layer will remain on the surface through MoS_2-metal interaction. Gold (Au) has proven to be highly effective in exfoliating layered materials including TMDCs by gold affinity towards chalcogen-based compounds [45]. The illustrated process of thermally activated metal-mediated process is depicted in Fig. 2.16 utilizing MoS_2 as the test material. The exfoliation initiates by exposing MoS_2 and Au surfaces, bringing them together on a hotplate. The process concludes by peeling off the MoS_2 parent crystal, resulting in large-area MoS_2 layers exfoliated onto gold. The annealing step is normally conducted at 200 °C, while performing output of worse quality at lower temperatures [46].

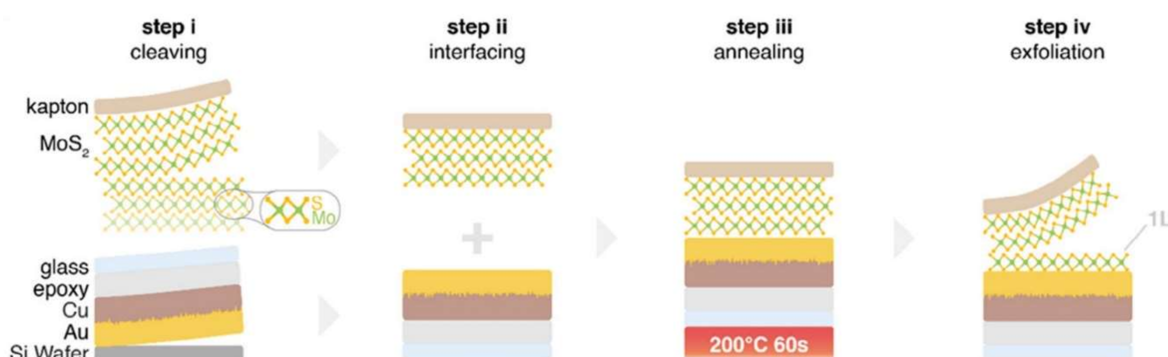

Figure 2.16 Schematic illustration of thermally activated metal-mediated exfoliation process of a MoS_2 thin film on a gold surface [46].

Often the resulting MoS_2 thin film is produced in the form of flakes with the area of a few mm^2. And basically, it would not disturb the characterization of the detectors based on such flakes in laboratory conditions. However, because of weak attachment between the flake and a substrate, the mechanical exfoliation imposes a risk to lose or damage MoS_2 flakes while moving the substrate or rotating it during an experiment. Therefore, it is vital to treat the samples with ME-fabricated MoS_2 nanosheets with great carefulness.

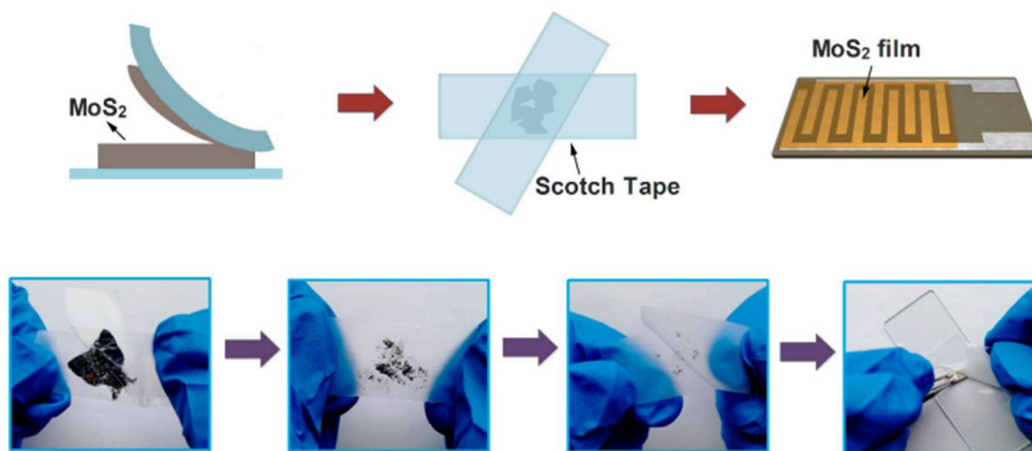

Figure 2.17 Schematic representation of the fabrication of MoS2 thin films by mechanical exfoliation (with the use of a scotch tape) [47].

- **Chemical Vapour Deposition (CVD) method**

Although mechanical exfoliation represents quite reliable and easy-to-perform method of TMDC thin film deposition, it loses all its potential when it comes to mass production and real-world applications. In this case, an alternative deposition technique should be used to output large-scale TMDCs nanosheets. Chemical vapour deposition (CVD) stands out as a good candidate for this purpose, as it has been widely adopted for the mass production of devices based on III-V and III-N materials. Despite its apparent simplicity, this technique continues to be one of the most extensively utilized methods for synthesizing thin films of TMDCs and in particularly, of MoS_2. Numerous positive reviews on the applying of the CVD method relatively to MoS_2 have already been published, which promotes the further research on this fabrication technique [48].

The working principle of CVD is depicted in Fig. 2.18. Precursors, consisting of either only sulfur S or both S and Mo, are delivered in gaseous form to a substrate, which is maintained at high temperature. At this temperature, the necessary chemical mechanisms for MoS_2 deposition onto the substrate takes place. While the substrate is typically held in horizontal position in most reports, is usually suffers from the film thickness gradient along the direction of the flow, leading to non-uniform deposition and challenges in determining the growth parameters of the film. To overcome this issue, the development of vertical CVD reactors takes place, since this configuration allows for easier control and homogeneity of temperature and precursor throughout the substrate surface [48].

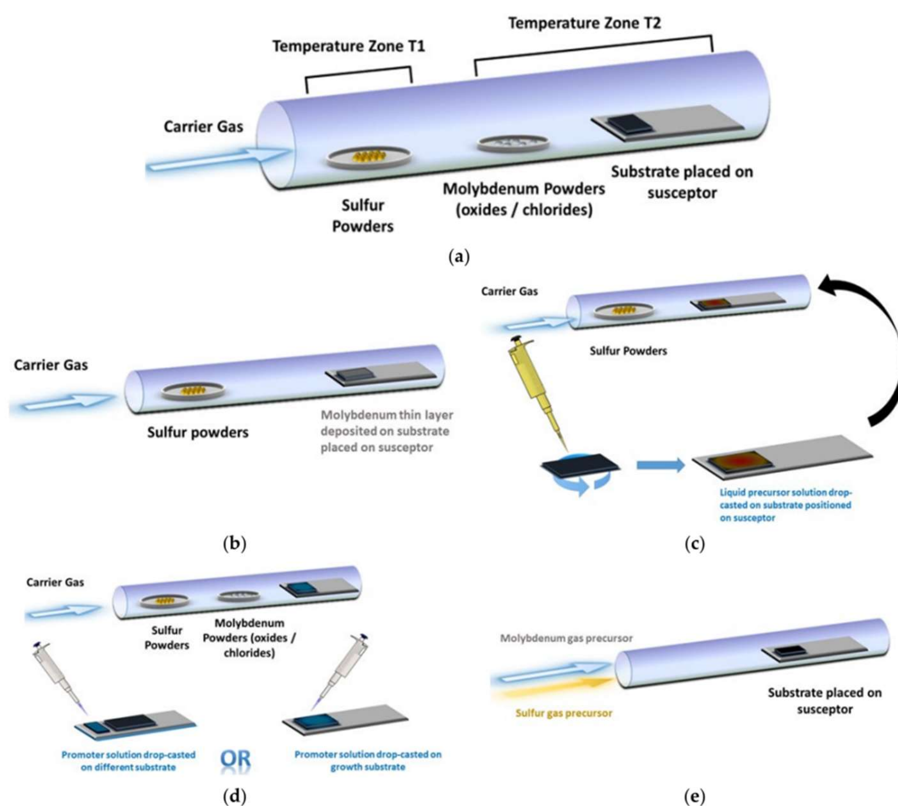

Figure 2.18 Schematic representation of the CVD tube in different configurations for MoS_2 thin film growth: (**a**) with solid precursors separated from each other; (**b**) with solid Mo precursor deposited on the substrate in advance; (**c**) with liquid Mo precursor deposited on the substrate; (**d**) with solid precursors and drop-casted promoters (either on the growth substrate or on a different substrate); (**e**) with gaseous precursors [48].

A common procedure starts with the reduction of contamination from external air and O_2 within the CVD tube by purging the system with inert gas multiple times before initiating the growth process. A typical CVD process depends on the phase form of the used precursors (solid, liquid or gaseous) and can be roughly divided into the following steps:

1) Converting the precursors (Mo and S) into a gaseous state and absorbing them into the inert carrier gas by evaporation or as sublimation powders;
2) Transporting the reactive species using the carrier gas to reach the substrate;
3) Diffusing the precursors toward the substrate surface;
4) Adsorption of the precursors at the surface, leading to the synthesis of the MoS_2 thin film [48].

In the standard horizontal setup, a quartz tube with dimensions of approximately 1 m in length and a diameter of 2-5 cm is employed. Heating is achieved through a resistor element wrapped around the tube. The MoS_2 deposition process requires the temperature in the range of 600-800 °C. In certain instances, an additional heating zone in the range of 100-200 °C is required for the S precursor. For

improved reproducibility and control, it is more convenient to independently heat this supplementary zone, where the S precursor is initially located. Alternatively, it is feasible to directly deposit the Mo precursor onto the substrate, either in solid form or as a liquid solution. Growth promoters may be added on the growth substrate or on a separate substrate to enhance the processibility. Lastly, the use of gaseous precursors eliminates the need to place the precursors inside the tube before initiating the process [48].

2.7.3 Overview on electrical properties of MoS_2-based TFTs

The semiconductor-like behaviour of MoS_2 subsequently led to its testing in FETs as an active channel. As a result, recent research conducted withing the group of Ji Heon Kim, has evaluated the main electrical parameters of a top-gate FET based on monolayer MoS_2 in ambient conditions. In this study thin MoS_2 flakes with different number of layers (N_{layer} = 1, 3 and 6) were fabricated by mechanical exfoliation and then transferred onto highly *n*-doped silicon wafers with SiO_2 dielectric of 300 nm on top. The gold (Au) collecting drain and source electrodes of 50 nm were deposited by conventional photolithography, electron-beam evaporation and lift-off technique. The electrical characterization of the samples was performed at room temperature after vacuum annealing at 120 °C for 4 hours. As a result, the average subthreshold swing *SS* was found to be 0.92, 0.92 and 1.41 V/dec for 1L-, 3L- and 6L-MoS_2, respectively. The ON/OFF ratio was calculated as ~10^6 for all the transistors. Finally, the field-effect electron mobility μ increased with increasing of N_{layer} ranging from ~10 to 18 $cm^2/(V{\cdot}s)$ [49].

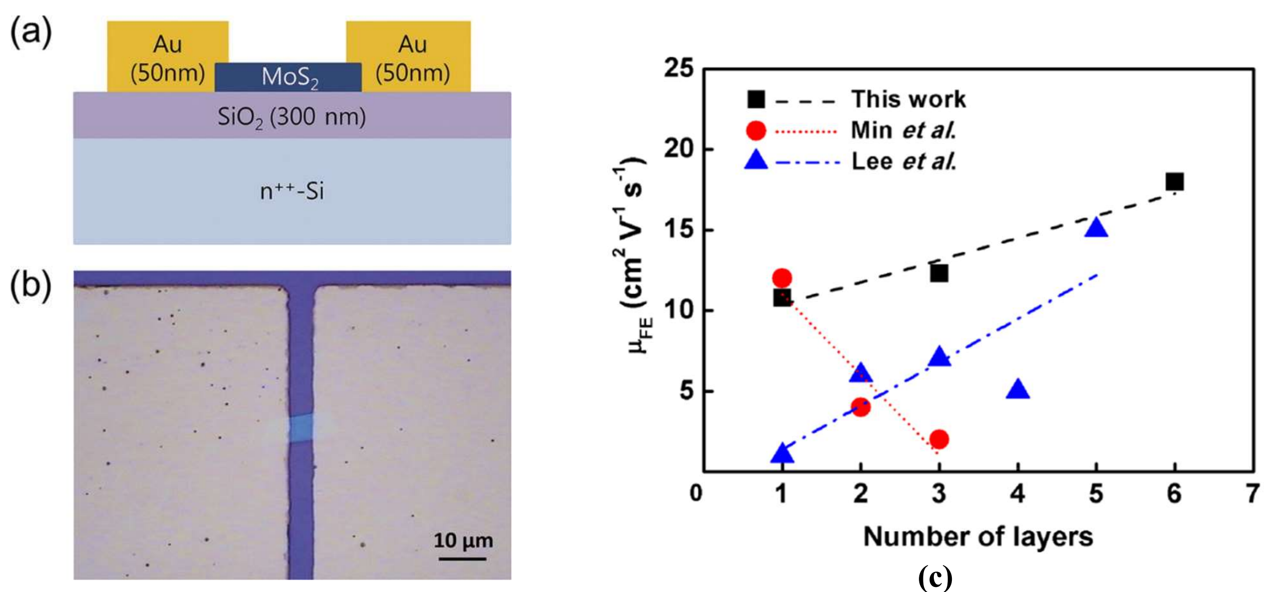

Figure 2.19 (**a**) Schematic cross-section of a MoS_2 thin-film transistor with bottom-gate architecture; (**b**) optical micrograph of the representative MoS_2 transistor; (**c**) field-effect mobility of the MoS_2 FET as a function of N_{layer} [49].

Alternative investigation of 1L-MoS_2 application in TFTs was undertaken by Zongyou Yin *et al.* In this experiment a monolayer MoS_2 film was deposited onto a Si with 300 nm of SiO_2 insulating layer by applying the scotch-tape based mechanical exfoliation method. The height of the MoS_2 single-layer film was measured by AFM and resulted in 0.8 nm (the channel length and width were estimated as 2.1 µm and 2.6 µm, respectively), which aligned with previous findings. The transistor device (Fig.2.20) was produced by deposition of Ti/Au drain and source electrodes onto the substrate by photolithography process, where the gate electrode was presented by the Si wafer. According to the results, the ON/OFF ratio was found to be ~ 10^3, whereas the calculated field-effect mobility of was 0.11 $cm^2/(V\cdot s)$. The mobility was claimed to be lower than expected, which was assumed to occur because of trap states at the SiO_2 surface in the bottom gate TFTs. The reduction of such trapping states in the bottom gate dielectric is expected to enhance the mobility of the MoS_2-based thin-film transistors [50].

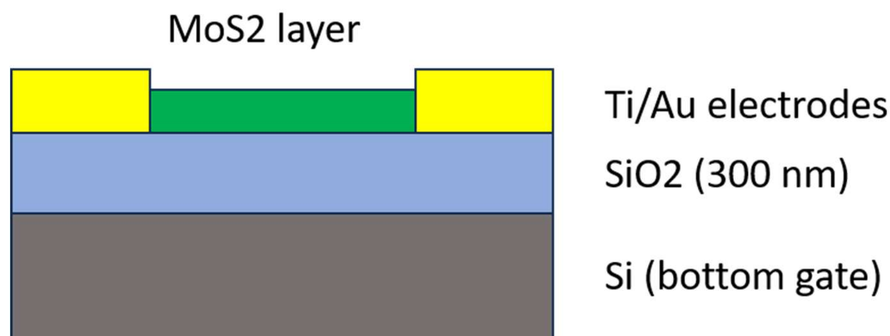

Figure 2.20 Schematic cross-section of thin-film transistors based on a single-layer MoS_2 thin film and characterized within the research conducted by Zongyou Yin *et al.* in [50].

Similar mobility values for a MoS_2 active channel were obtained in the research conducted by Hai Li *et al*., where of the single- and multilayer MoS_2 nanosheets (from 1 to 4 layers) were deposited onto Si/SiO_2 (300 nm of SiO_2) substrates by mechanical exfoliation technique. Analogously to the aforementioned study, the average thickness of a MoS_2 monolayer film was estimated to be 0.8 nm, whereas the thickness of the multilayer nanosheets was calculated as 1.5, 2.1 and 2.9 nm for 2, 3 and 4 layers, respectively. By electrical characterization of the obtained TFTs, the average mobility was evaluated to range from 0.03 to 0.22 $cm^2/(V\cdot s)$ increasing proportionally to the number of layers. Additionally, the ON/OFF ratio for each N_{layer} was found to be ~10^3 [51].

An increased mobility for single-layer MoS_2-based TFTs was found within the group of B. Radisavljevic. The transistors were initially produced through the scotch tape-based mechanical exfoliation method, transferring MoS_2 monolayers onto degenerately doped Si substrates covered with a 270 nm thick SiO_2 insulting layer. The active channel was estimated to be 0.65 nm thick, while

the length and width parameters were 1.5 µm and 4 µm, respectively. Electrical contacts were fabricated using electron-beam lithography followed by deposition of gold electrodes with thickness of 50 nm. Subsequently, the samples underwent annealing at 200 °C to eliminate resist residue and to reduce contact resistance. Resultantly, the MoS_2 monolayer devices exhibited a typical mobility μ in the range of 0.1 - 10 $cm^2/(V\cdot s)$ [52].

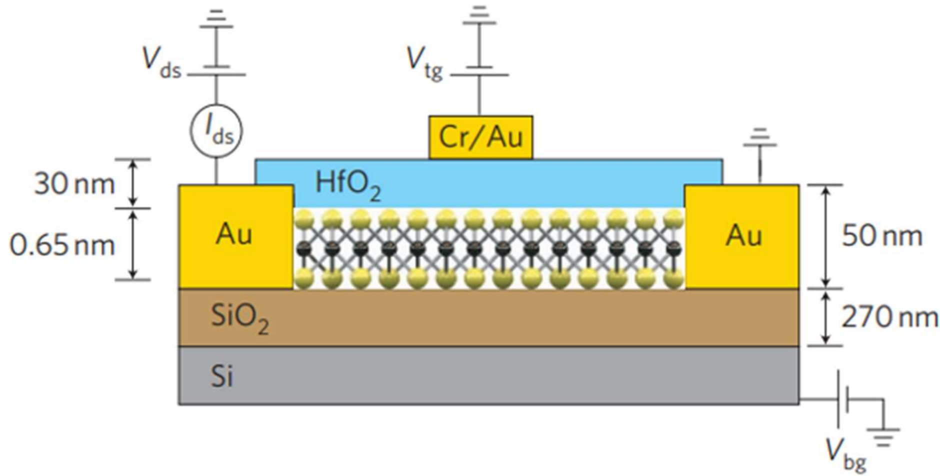

Figure 2.21 Schematic representation of a thin-film transistor with the top-gate configuration with a HfO_2 layer adjusted to the gate to enhance the device mobility [52].

Motivated by theoretical predictions suggesting mobility improvement through dielectric screening, the research group modified the transistor configuration by applying atomic layer deposition to add a 30 nm thick HfO_2 layer as a local top gate (Fig. 2.21). Subsequent electrical characterization at room temperature revealed the average low-field effect mobility of approximately 217 $cm^2/(V\cdot s)$ and an ON/OFF ratio proportional to 10^6. Additionally, analyzing the transfer characteristics of the modified TFTs, the subthreshold slope *SS* was estimated to be 74 mV/dec for a V_{DS} of 500 mV. Despite the notable enhancement in TFT performance with the use of HfO_2 layer, the electrical parameters obtained in my research will be compared to those achieved from the TFTs without the HfO_2 layer.

2.7.4 Overview on the performance of 1L-MoS_2 direct X-ray detectors

Apart from applications in exclusively thin-film electronics field, MoS_2 is also represents a prominent active material in photodetectors [39]. Nevertheless, despite the numerous studies focused on the photodetection properties of this semiconductor, it has not been extensively investigated as ionizing radiation detectors yet. Only a few works provide information about the employment of MoS_2-based devices for the detection of X-rays. As an example of a comprehensive examination of

MoS_2 applications for X-ray detection, in subsequent sections I would like to focus on the research conducted by Professor Taffelli *et al*. and described in [39]. The goal of the study was to showcase the effective employment of thin-film MoS_2 as a potential semiconducting material for direct X-ray detection. For this purpose, the group realized a planar detector based on a photoconductor architecture, implementing a monolayer MoS_2 (1L-MoS_2) as the active layer. The device was exposed to X-rays within the energy range of 10-100 keV. Furthermore, they compare the direct and indirect X-Ray detection performed by the MoS2 monolayer by the coupling a scintillator film to induce light-matter interaction in the visible light spectrum. This strategy resulted in increase of photocurrent by converting a small fraction (~4 %) of the radiation into the visible spectrum.

The 1L-MoS_2 thin films were fabricated with the exfoliation of a MoS_2 bulk crystal through a thermally activated metal-mediated process already described in the previous section. With this process, 1L-MoS_2 was acquired on a thin Au film. After that a monolayer MoS_2 film was then covered with a polystyrene film of ~1 μm via spin coating. The gold film was then etched leaving the MoS_2 monolayer embedded in PS, which was then transported to the substrate through wet transfer. The resulting X-ray detector was constructed on a soda-lime glass substrate, where gold (Au) electrodes with the thickness of 100 nm were deposited thermal evaporation. The active channel was created by the MoS_2 and was supposed to have the area of 1×0.3 mm^2 determined by the area between the collecting electrodes. The thickness of the active channel was evaluated as 0.9 nm. The scintillator film with the thickness of 0.2 nm, was based on polydimethylsiloxane (PDMS) containing gadolinium oxysulphide doped with terbium (Gd_2O_2S:Tb) and was deposited on top of the PS film, thus, resulting in the layered structure depicted in Fig. 2.22(c) [39].

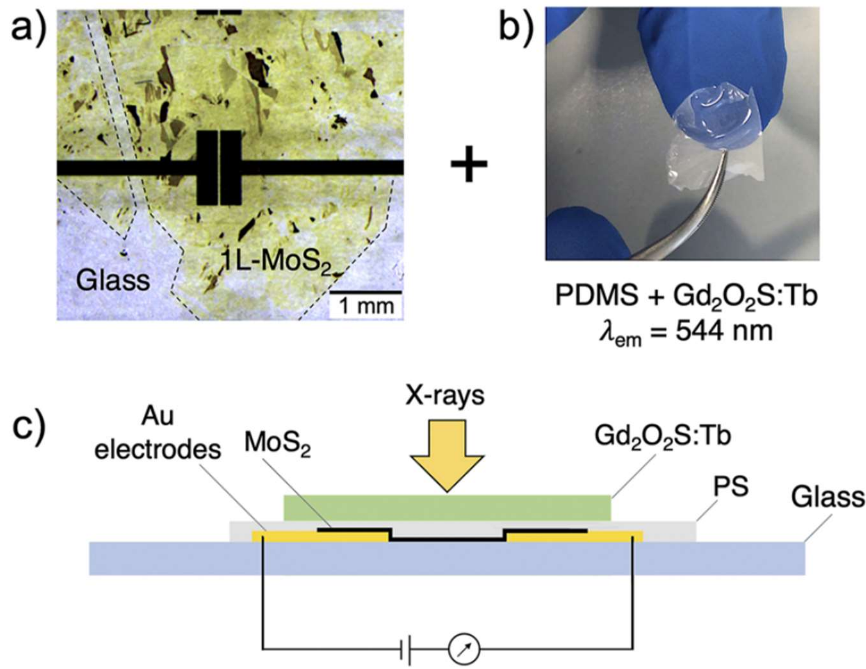

Figure 2.22 (**a**) An optical image taken with a microscope of the top view of the X-ray detector device based on 1L-MoS_2. The dashed line outlines the MoS_2 flake, under which the Au electrodes are deposited; (**b**) An image of the scintillator film based on PDMS and loaded with Gd_2O_2S:Tb; (**c**) A schematic cross-section of the 1L-MoS_2-based X-ray detector [39].

The fabricated MoS_2 detector then underwent X-ray testing to test its sensitivity. The active channel was constantly biased under V_{bias} = 5 V. The X-rays were generated by a tungsten anode ($W_{K\alpha}$ = 59 keV) operated at peak voltages of 40, 100, 150, 195 kV filtered with 3 mm of copper to remove the low-energy part of the spectrum. The radiation was performed in the form of periodic pulses of 20 s in the *on*-regime and 40 s in the *off*-regime. The X-ray response of the MoS_2 detector was measured both with and without the scintillator film placed on top of the detector. The PS layer on top of MoS_2 was estimated to absorb less than 0.01 % of the incident radiation, therefore, it was not supposed to deteriorate the obtained data from the active channel [39].

Consequently, the photoresponse exhibited an increase of up to three times when incorporating the scintillator film onto the detector. The amplification was ascribed to the generation of additional visible photon from the scintillator through indirect X-ray photoconversion. Furthermore, the MoS_2 detector consistently demonstrated a photoresponse to incoming X-rays over subsequent irradiation cycles, which indicated the reproducibility of the measurements [39].

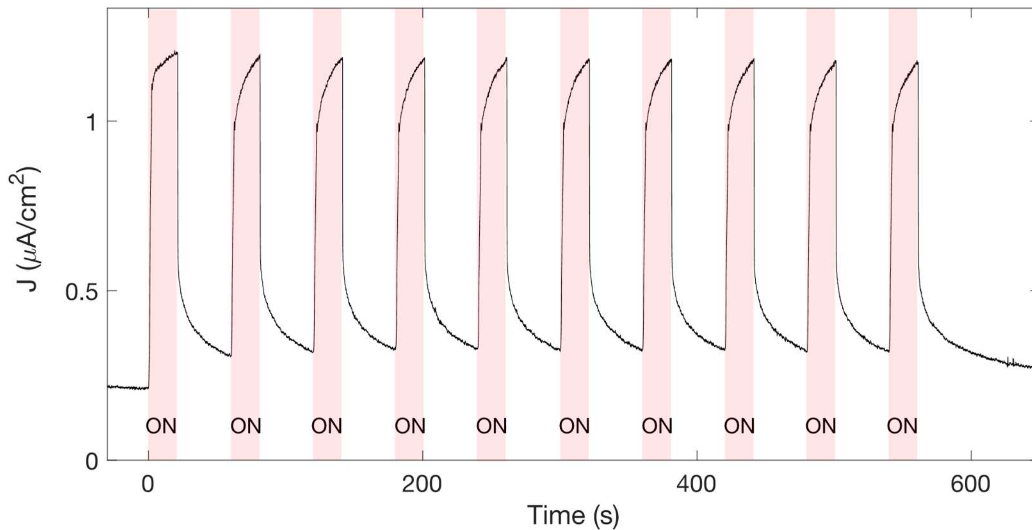

Figure 2.23 Current density of the detector based on 1L-MoS_2 incorporating the scintillator during subsequent irradiations for 20 s of X-rays produced at 100 kV and dose rate 7.05 mGy/s. The detector was operated at 5 V during the measurement [39].

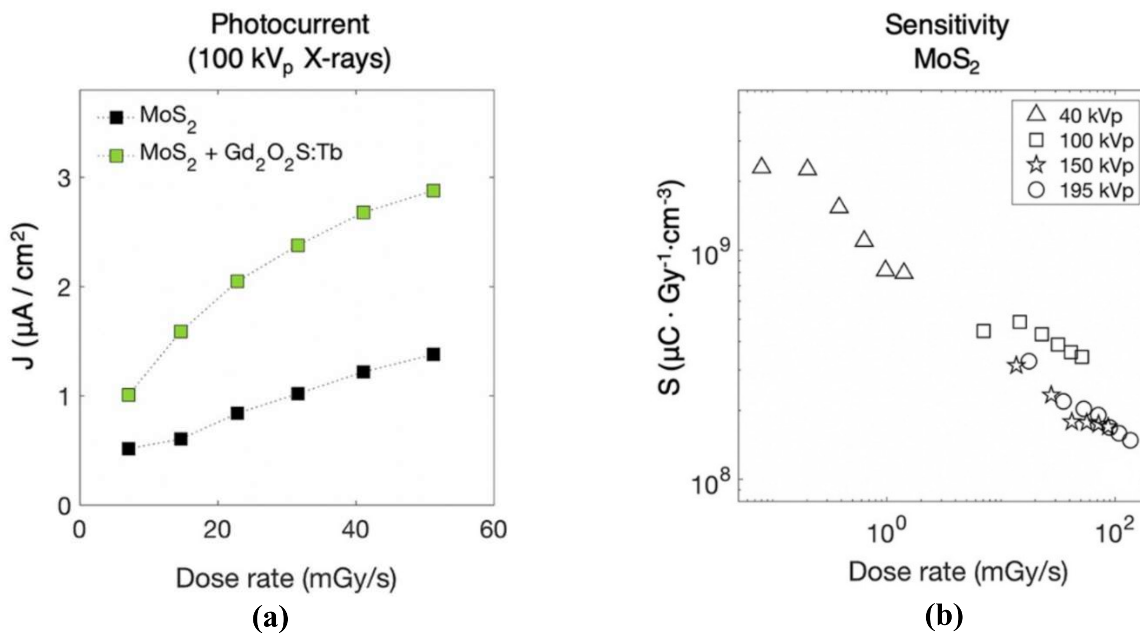

Figure 2.24 Performance of the MoS_2-based photodetectors under X-rays: (**a**) X-ray photocurrent density as a function of the X-ray dose rate operating the source at 100 kV. The black markers correspond to the 1L-MoS_2-based photoconductor, while the green markers represent the device incorporating the scintillator film. (**b**) Sensitivity of 1L-MoS_2 under different X-ray energies and dose rates. The detector was operated at 5 V during these measurements [39].

As a result, the sensitivity per unit volume was evaluated to be within the range of 10^8-10^9 μC/(Gy·cm^3) with the maximum value of 2.3×10^9 μC/(Gy·cm^3). The sensitivity per unit area was

estimated to be in the order of 10-100 μC/(Gy·cm^2). Furthermore, it was discovered that the addition of a scintillator film based on Gd_2O_2S:Tb enhanced the photocurrent up to a factor 3 relatively to that generated by the photodetector based solely on a MoS_2 thin film. Even though the scintillator film was also present in the measurements, the fraction of incident radiation absorbed by the scintillator was less than 4 %, which is negligibly small to introduce the indirect detection mechanism [39].

According to these numbers, we can conclude that TMDCs, in particular, monolayer MoS_2, can be competitive (in relation to fully-organic based) semiconductors for flexible and large area radiation detectors based on semiconducting thin films. Even though TMDCs have not yet been so widely studied as organic-based X-ray detectors, it is evident that MoS_2-based X-ray detectors are promising alternatives to conventional inorganic sensing devices.

Chapter 3 Experimental Methods

The experimental part is divided into two sections. The first part is focused on the characterization of MoS_2-based phototransistors, whereas the second dealt with TMTES:PS-based phototransistors. For each semiconductor materials, the correspondent study included a full electrical characterization of the devices and subsequent characterization of the detectors under X-ray radiation. The MoS_2 based X-ray detectors have the top-contacts bottom-gate phototransistor architecture while the TMTES:PS-based devices are bottom-contacts bottom gate OFETs. In both the classes of devices, the gate electrode is formed by a Si wafer while the dielectric layer is made by Silicon dioxide.

In this chapter I firstly describe the experimental setup employed during my thesis work. Then, I the architecture of the MoS_2-based detectors and their fabrication methodology will be discussed. After that I will describe the electrical characterization procedure and which electrical parameters were calculated. Finally, the characterization of the devices under X-ray radiation will be discussed in detail. Analogously, in the second part of this chapter I will describe the similar procedure of IV-characterization and examination under X-rays for the TMTES:PS devices.

3.1 Experimental setups

In this section I will describe the experimental setups that were used for electrical characterization and X-ray measurements for both detector batches. The protocols and equipment described in this section, were employed for both MoS_2 and TMTES:PS based devices characterization.

- **Faraday cage**

The electrical characterization was performed inside a Faraday cage (Fig. 3.1) to prevent the illumination of the samples during the measurements and to screen the electromagnetic noise coming from the external.

All the operations were controlled through an optical microscope (Fig. 3.1(a)). The three terminals of the transistors have been electrically connected by tungsten tips mounted over three micromanipulators which allow micrometric movements in the three directions. In order to apply a voltage between the pads and to measure the current between them, a 2-channel source measure unit (SMU) Keysight B2912A was employed (Fig. 3.1(b)), where Ch1 was referred to gate (G) and Ch2 was referred to drain (D). The source (S) pad was referred to ground and was connected to both channels through a “Low Force” port. The G and D connection was realized with triaxial cables, whereas S was connected to the SMU with two coaxial cables.

(a)

(b)

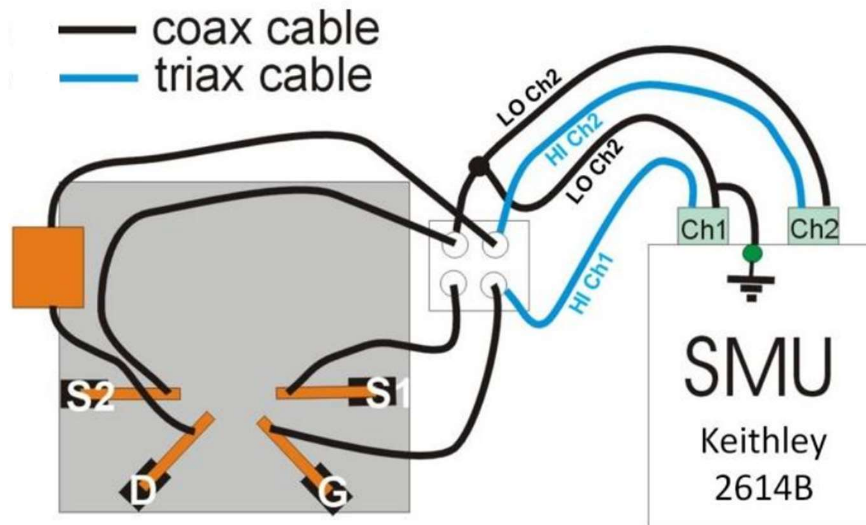

(c)

Figure 3.1 Experimental setup for electrical characterization of the MoS_2 and TMTES:PS samples: (**a**) Faraday cage and conductive tips mounted over micromanipulators; (**b**) SMU instrument (Keysight B2912A) to measure the current-voltage behaviour of a transistor; (**c**) schematic diagram of the electrical connections and the cables use during the electrical characterization of both MoS_2 and TMTES:PS samples.

It is noteworthy to mention again that such configuration was applied to both batches of MoS_2 and TMTES:PS samples. The SMU was operated by a computer through a customized software, developed specifically for such measurements. During the electrical characterization, for each transistor transfer characteristics ($I_{DS}(V_{GS})$ and $I_{GS}(V_{GS})$) in linear and saturation regimes and output characteristics ($I_{DS}(V_{DS})$ and $I_{GS}(V_{DS})$) were measured.

- **X-ray measurements**

For the characterization of the samples under X-rays, I used a compact X-ray tube with a tungsten (W) target anode (Fig. 3.2). The Hamamatsu power source operates the X-ray tube with the voltage between the electrodes in the range $V_{X-ray} \in [40, 150]$ kV and with the current of incident electrons in the range $I_{X-ray} \in [10, 500]$ µA. As a result, the maximum energy of the outcoming photons is in the range between 40 keV and 150 keV depending on the tube biasing. The exit for the X-rays is covered with a beryllium (Be) window. To control the dynamics of the incoming radiation, the X-ray beam is switched on/off with a mechanical lead shutter placed in front of the Be window. Both the X-ray tube and the shutter are operated via a the "MFX Control Software", where different parameters ($V_{X\text{-}ray}$, $I_{X\text{-}ray}$, shutter on/off frequency) are set up. Additional parameter "Acquisition time" (time between two subsequent electrical acquisition) was set as 500 ms during the measurements.

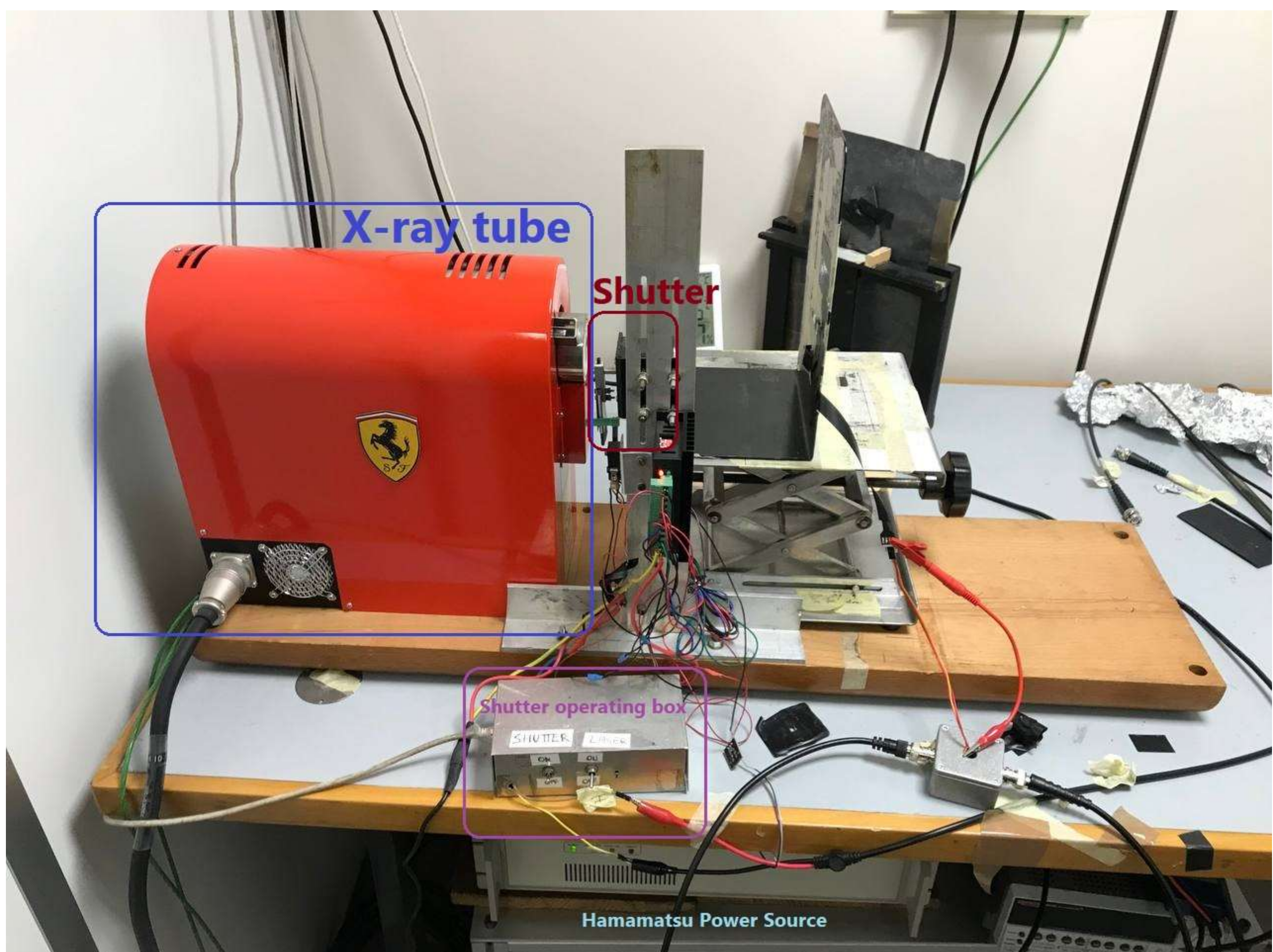

Figure 3.2 Experimental setup for the characterization of a phototransistor under X-ray radiation.

During X-ray exposure, MoS_2 and TMTES:PS phototransistors were placed in different experimental boxes, which act both as Faraday cages and allow the electrical connection of the

devices. Their detailed description will be provided in the sections regarding the X-ray measurement procedure. To monitor the current (I_{DS} and I_{GS}) and apply bias (V_{DS} and V_{GS}) in the devices, another 2-channel SMU Keithley 2614B was used, where similar configuration was presented: chA was connected to G, chB was connected to D, while S was referred to the ground through connection to both channels.

(a)

(b)

(c)

Figure 3.3 Fragments of the experimental setup for X-ray measurements: (**a**) Hamamatsu power source unit for the X-ray tube; (**b**) Lead shutter in front of the Be window of the X-ray tube; (**c**) Keithley SMU for electrical readout of a phototransistor under X-ray radiation.

Beside exclusively experimental equipment for the X-ray irradiation, in this section I also would like to mention the calibration plot (Fig. 3.4) that is used to convert the X-ray tube characteristics, such as $I_{X\text{-}ray}$ and $V_{X\text{-}ray}$, into the absorbed dose rate DR values. This plot was used during the calculations of the sensitivity for both MoS_2 and TMTES:PS X-ray detectors described in Chapter 4. The intensity of the radiation emitted by the tube was initially calibrated employing the output of a commercial BARRACUDA Si-based X-ray analyzer placed at the distance of 50 cm from the chassis (front edge of the red shell) of the X-ray tube.

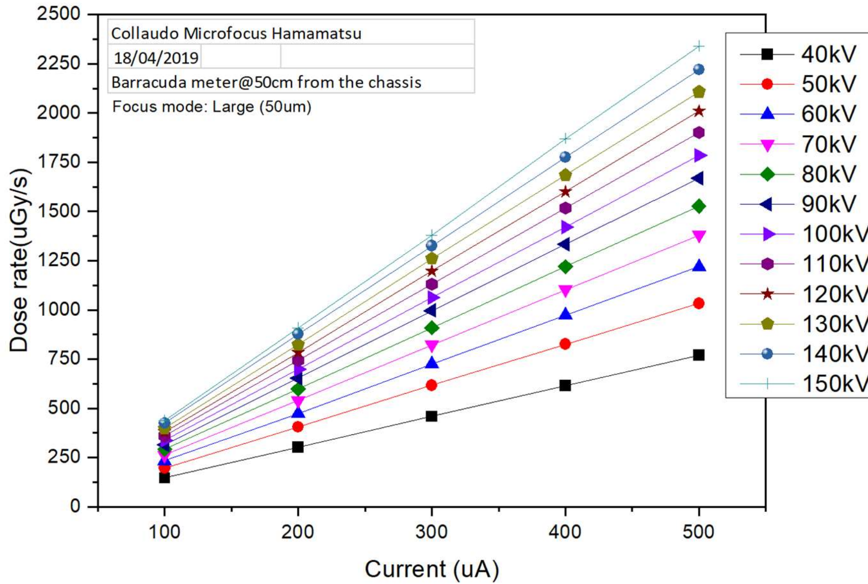

Figure 3.4 Calibration plot for the Hamamatsu X-ray tube used in the experiment. This plot allows to determine the absorbed dose rate in (µGy/s) from the values of $I_{X\text{-}ray}$ and $V_{X\text{-}ray}$ operated in the X-ray tube. The provided data will be used for the sensitivity calculations of both the MoS_2- and TMTES:PS-based phototransistors.

The calibration plot might be employed when it is necessary to calculate the dose rate for a detector at different distance from the chassis. As for any electromagnetic radiation, the intensity **I** of X-rays decreases with inverse proportionality of the square of the distance r between the source and the target:

$$DR \sim \mathbf{I} \sim \frac{1}{r^2} \qquad 3.1$$

By using such dependence, it become possible to calculate the absorbed dose rate at any distance between the X-ray tube and a detector. For example, if we denote dose rate provided by Fig. 3.4 as DR_1 at a distance of r_1 = 50 cm from the chassis, the unknown dose rate DR_2 at a distance r_2 can be extracted through the proportion:

$$DR_2 = DR_1 \times \left(\frac{r_1}{r_2}\right)^2 \qquad 3.2$$

- **Glovebox**

Both the MoS_2 and TMTES:PS phototransistors were not encapsulated, therefore, the active channel of a device was prone to become contaminated with air and to degrade due to the direct contact with the environment. In order to avoid intense degradation of the semiconductors due to oxygen and water, after each experimental session, the samples were placed in a glovebox filled with nitrogen and almost-zero concentration of oxygen. Moreover, the samples were stored in dark to prevent photo-oxidization.

3.2 MoS2 Samples

The batch of the MoS_2-based phototransistors (Fig. 3.5(a)) contains 11 Si substrates (denoted as *samples*) with one or more transistors (*devices*) fabricated on each substrate (Fig. 3.5(b)). Each device has the top-contact and bottom-gate architecture and it is deposited on a substrate made of a Si wafer, which also forms the gate electrode and which has a silicon oxide SiO_x layer on top serving as an insulating layer in a phototransistor. On top of the SiO_x layer a benzocyclobutene (BCB) film of 50 nm thick is deposited. On such multilayer structure several MoS_2 flakes are placed via mechanical exfoliation. Finally, drain and source electrodes made of chromium (Cr) and gold (Au) with thicknesses of 3 nm and 45 nm respectively, are deposited to the MoS_2 flakes, which in this configuration form an active channel. Each device has an active channel with the length L and width W, which are determined by the geometry of collecting electrodes, and with the thickness, which is defined by the thickness of a certain MoS_2 flake. It is noteworthy to stress out that some MoS_2 flakes can have dimensions different from the area between the electrodes, for example, a semiconducting nanosheet can be larger or shorter than the defined width W (Fig. 3.5(d)), or have a non-regular shape. Such imperfections must be taken into account during calculating electrical parameters of a device, since they might distort the obtained parameter from its real value. These devices have been fabricated by Dr. Adrian Tamayo at the University of Strasburg under the supervision of Professor Samorì.

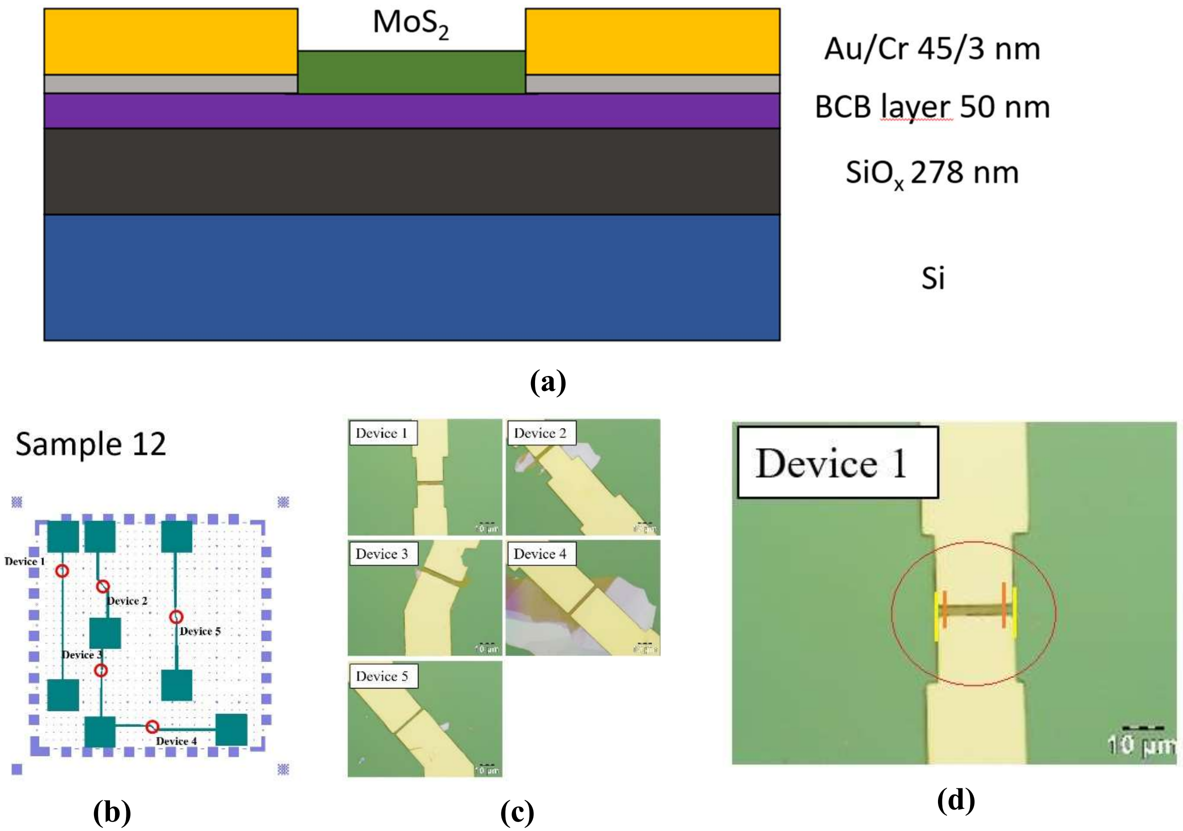

Figure 3.5 (**a**) Schematic cross-section of a MoS_2-based phototransistor; (**b**) map of a single substrate (sample) with a group of the devices; (**c**) optical images of MoS_2 active channels in each device; (**d**) active channel of a phototransistor denoted as Sample12_device1. The orange and yellow lines indicated the edges of the MoS_2 flake and pf the Au Pads, respectively.

3.2.1 Electrical characterization of the MoS_2 phototransistors

The electrical characterization was accomplished by using the mentioned Faraday cage (see above). First, the transfer characteristics in saturation regime (denoted as *trf_Sat*) were acquired while keeping V_{DS} at 1 V by sweeping the gate voltage V_{GS} from -60 V to 60 V with the step of 0.5 V. Once the transfer characteristics demonstrated that the device worked properly, the output characteristics was performed by varying V_{DS} from 0 V to 1 V with the step of 0.1 V, while V_{GS} varied from -30 V to 60 V with the step of 10 V, so that 10 curves were obtained. In its turn, the output characteristics allowed me to identify the V_{DS} range for linear and saturation regimes of the device. Finally, by setting a V_{DS} value in the linear regime (typically it was ~0.1 V), the transfer characteristics in linear regime (denoted as *trf_Lin*) was performed. To summarize, the whole electrical characterization could be described in the following steps:

1) **trf_Sat**: $V_{DS} = 1$ V, $V_{GS} \in [-60, 60]$ V, step = 0.5 V;
2) **Output**: $V_{DS} \in [0, 1]$ V, step = 0.1 V, $V_{GS} \in [-30, 60]$ V, step = 10 V;
3) **trf_Lin**: $V_{DS} \sim 0.1$ V, $V_{GS} \in [-60, 60]$ V, step = 0.5 V.

3.2.2 Characterization of the MoS_2 phototransistors under X-rays

After the initial IV characterization, the MoS_2-based devices were exposed to the X-ray radiation from the X-ray tube. The devices were placed at the distance of 30 cm from the Be window of the X-ray tube (measured with a meter). The general protocol for each device was the following:

1) First, to acquire the transfer characteristics in saturation regime in the dark (without incident radiation) to verify that the phototransistor works properly.
2) If the device operates correctly, the X-ray radiation was turned on. The goal of the X-ray measurements is to calculate the sensitivity of the MoS_2 active channel. For this purpose, a photocurrent due to impinging photons should be measured at different dose rate values. In order to generate X-ray radiation with varying dose rate, the X-ray tube voltage is kept at $V_{X\text{-}ray}$ = 150 kVp, while the X-ray tube current $I_{X\text{-}ray}$ is sequentially equal to 500 µA, 400 µA, 300 µA, 200 µA and 100 µA. During each radiation exposure, the shutter performs the on/off switching cycle, such that the radiation impinges on the device for 10 seconds (*on*-mode) and then is shut for 10 seconds (*off*-mode) by the shutter. As a result, at least four radiation pulses (depicted as photocurrent peaks of I_{DS} and I_{GS}) of 10 seconds each should be registered. After the last X-ray pulse, the device is kept in the dark for at least 60 seconds.

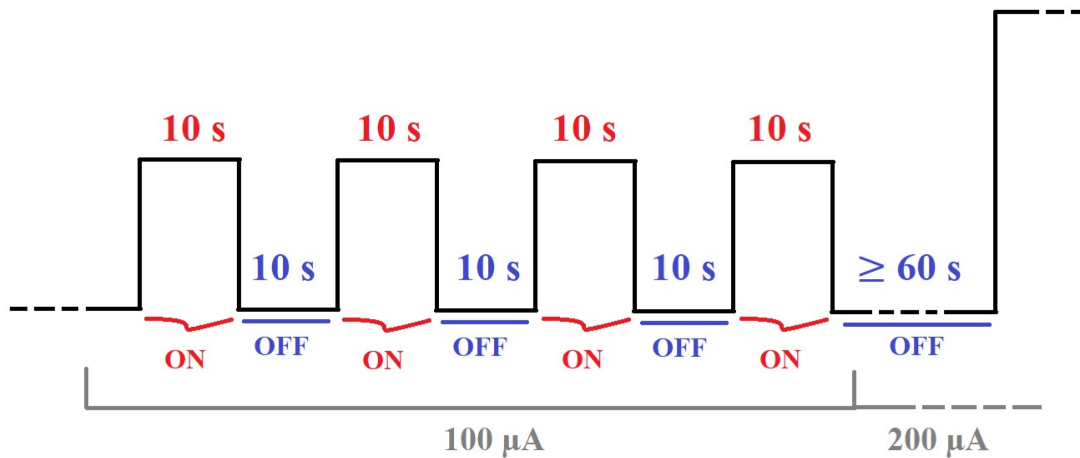

Figure 3.6 Schematic representation of an irradiation exposure at $I_{X\text{-}ray}$ = 100 µA. By using the shutter, the X-ray radiation is performed in the form of pulses of 10 seconds long. Normally four pulses are collected. After each irradiation sweep the device is kept in the dark for 60 seconds or more.

3) While performing the X-ray pulses, the MoS_2 devices are bised in saturation regime with voltage between source and drain V_{DS} = 1 V. The gate voltage V_{GS} is varied in the range from -50 V to 50 V to (i) study the detecting response of the device as a function of the biasing conditions and to (ii) keep I_{DS} in the order of ~10^{-6} A.

Once indicating the following rules, we started the X-ray exposure procedure. The devices were placed and electrically connected inside the Nextron experimental box depicted in Fig. 3.7.

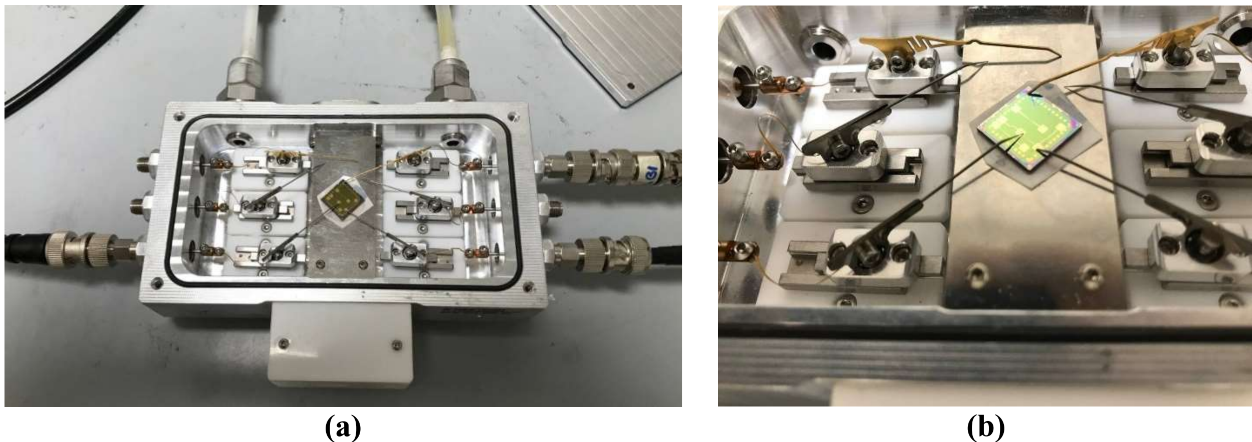

(a) **(b)**

Figure 3.7 (**a**) Nextron box for the X-ray measurements of the MoS_2-based detectors; the box is equipped with six micromanipulators for the electrical connections. (**b**) A close view to the MoS_2 detector placed in the Nextron box; in order to avoid connection of the Si substrate with metallic surface, the device is deposited on a parafilm sheet.

In order to prevent the MoS_2 detector degradation due to visible light illumination and the increasing of the dark current due to light absorption, the Nextron box was also covered with Al foil during the whole characterization procedure to keep the device in dark. Before the irradiation cycles, each device performed transfer characteristics in saturation regime. The results of the MoS_2-based detectors and analysis of their performance under X-rays will be provided in the next chapter. In the next sections I will discuss the experimental procedure relation to the TMTES:PS-based X-ray detectors.

3.3 TMTES:PS samples

This section will be focused on the study of X-ray detectors based on the TMTES:PS organic semiconductor. It is noteworthy to mention that this research is basically a continuation of a previous study regarding TMTES:PS based X-ray detectors [33]. The fabrication process of the TMTES:PS based X-ray detectors was carried out at the *Institute de Ciencia de Materials de Barcelona* (ICMAB) within the research group of Dr. Marta Mas-Torrent.

3.3.1 Fabrication methods

Before the deposition of the organic semiconductor blend, the drain and source electrodes were fabricated via thermal evaporation of 5 nm of chromium (Cr) (acting as adhesion layer) followed by 40 nm of gold (Au) onto a heavily *n*-doped silicon (Si) wafer (provided by Si-Mat) with a 200 nm thick layer of SiO_2. After the film deposition, interdigitated Au/Cr electrodes were patterned by photolithography process. The resulting devices were designed in the form of a pixel with the active area $A = 4.25 \times 10^{-3}$ cm^2 made with the channel length $L = 25$ μm and the channel width $W = 2500$ μm, thus, keeping the width/length ratio equal to 100. The substrates were then cleaned by sonication with acetone and isopropanol in HPLC grade and then dried under nitrogen flow.

The surface of the source and drain Au/Cr electrodes was then chemically modified with a self-assembled monolayer (SAM) of 2,3,4,5,6-pentafluorothiophenol (PFBT, obtained from Sigma-Aldrich). The Au surfaces were exposed to a UV ozone cleaner for 25 minutes and then immersed in a 15×10^{-3} M solution of PFBT in isopropanol for 15 minutes. Finally, the prepared substrates were cleaned with pure isopropanol to remove the excess PFBT and dried with a nitrogen flow.

Once the substrates for the active channel deposition was completed, the organic semiconductor preparation took place. 1,4,8,11-Tetramethyl-6,13-triethylsilylethynyl pentacene (TMTES) and polystyrene (PS) of 280 000 g/mol (or 280 kDa) were employed with further treatments. The TMTES and PS solutions were prepared in anhydrous chlorobenzene with a final concentration of 2.0 % w/w. For blended solutions, the TMTES and PS solutions were mixed in a TMTES:PS ratio of 17:3, 9:1, 19:1 and 39:1. Before the deposition, the blends were heated to the temperature of used for the coating process. The TMTES:PS semiconducting layer was deposited on the prepared substrates via the Bar-Assisted Meniscus Shearing (BAMS) technique. The BAMS deposition procedure was conducted at 105 °C and with a coating speed of 10 mm per second. It is important to point out that the whole device fabrication process was performed under ambient conditions with no post-thermal treatments of the samples.

After the fabrication process, the prepared devices were placed in a plastic box filled with nitrogen and transferred to the Department of Physics at the University of Bologna. The whole batch consists of four sets of the phototransistors classified by the TMTES:PS ratio, which has values of 17:3, 9:1. 19:1 and 39:1. The molecular weight of PS in all devices is the same and equals to 280 kDa. Each set with a specific TMTES:PS ratio includes two Si substrates (*samples*), each of which accommodates four phototransistors (*devices*) with common gate represented by the heavily *n*-doped Si wafer (Fig. 3.8(b)). In total, the whole batch is composed of 32 devices, 8 for each TMTES:PS ratio deposited on two substrates.

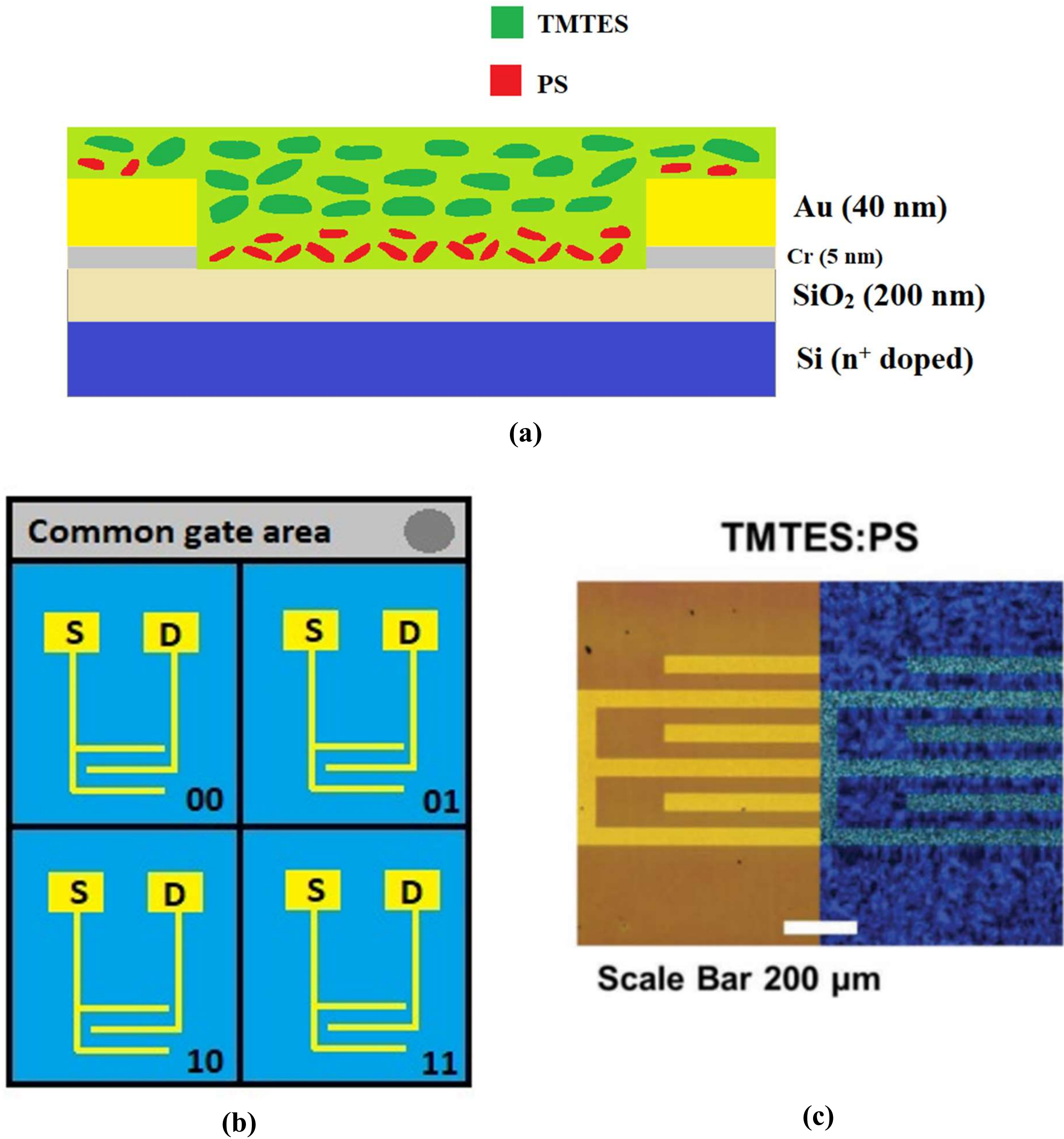

Figure 3.8 (**a**) Schematic cross-section of a TMTES:PS based phototransistor. (**b**) A single substrate (*sample*) configuration. Four phototransistors (*devices*) are arranged in a matrix and are denoted by the numbers 00, 01, 10, and 11. The common gate area (grey circle) indicates a surface of the Si wafer, which is used as the gate electrode. (**c**) Optical microscope image (left) and cross-polarized optical microscope image (right) of the TMTES:PS thin film deposited by BAMS on a Si/SiO_2 substrate with the interdigitated Au electrodes [33].

3.3.2 Electrical characterization

Similarly to the first part of the research related to the MoS_2 detectors, the TMTES:PS devices initially were electrically characterized. To perform this characterization, we used the same Faraday cage and the SMU, which had also been exploited for the MoS_2 phototransistors.

The electrical characterization of TMTES:PS devices included the output characteristics of a device and the transfer characteristics in both saturation and linear regimes, where the voltage sweep was performed forward and backward. Initially, the devices with the highest quantity of PS indicated by the TMTES:PS ratio of 17:3 were characterized, then subsequently reducing the proportion by considering the ratios of 9:1, 19:1 and finally of 39:1. First, we achieved the output characteristics in order to determine the regions for the linear and saturation regimes. Since the TMTES:PS organic semiconductor is a *p*-type semiconductor, the drain-source voltage V_{DS} was operated at values below zero. For the devices with the TMTES:PS ratio of 17:3 and 9:1, V_{DS} ranged starting from 0 V to -10 V with the step of 0.5 V. The gate voltage V_{GS} was swept from 5 V to -5 V with the step of 2.5 V. The linear regime was determined at V_{GS} ~ -0.5 V. The next step was to obtain the transfer characteristics in saturation and in linear regimes (*trf_Sat* and *trf_Lin*). For this purpose, the gate voltage V_{GS} ranged from 5 V to -5 V with the step of 0.1 V, whereas V_{DS} was fixed at -10 V for the saturation regime and at -0.5 V for the linear regime.

When we moved to the devices with the TMTES:PS ratio of 19:1 and 39:1, I extended the bias range both for V_{GS} and V_{DS} because of the greater no-ideality of the OFET (i.e. Vth shifted from 0V). For this purpose, the output characteristics were performed at V_{DS} ranging from 0 V to -20 V with the step of 0.5 V, whereas V_{GS} changed from 10 V to -15 V with the step of 5 V. The transfer characteristics in saturation and linear regimes were obtained by fixing V_{DS} at -10 V and -0.5 V, respectively, and sweeping V_{GS} from 20 V to -15 V with the step of 0.1 V. As a whole, the IV characterization procedure can be schemed as follows:

1) **Output**: $V_{DS} \in [0, -10]_{st=0.5}$ V, $V_{GS} \in [5, -5]_{st=2.5}$ V – for TMTES:PS = 17:3 and 9:1
   $V_{DS} \in [0, -20]_{st=0.5}$ V, $V_{GS} \in [10, -15]_{st=5}$ V – for TMTES:PS = 19:1 and 39:1

2) **trf_Sat**: $V_{DS} = -10$ V, $V_{GS} \in [5, -5]_{st=0.1}$V – for TMTES:PS = 17:3 and 9:1
   $V_{DS} = -10$ V, $V_{GS} \in [20, -15]_{st=0.1}$V – for TMTES:PS = 19:1 and 39:1

3) **trf_Lin**: $V_{DS} = -0.5$ V, $V_{GS} \in [5, -5]_{st=0.1}$V – for TMTES:PS = 17:3 and 9:1
   $V_{DS} = -0.5$ V, $V_{GS} \in [20, -15]_{st=0.1}$V – for TMTES:PS = 19:1 and 39:1

3.3.3 Characterization under X-rays

The TMTES:PS devices were exposed to X-rays. The X-ray tube and the SMU were the same that had been employed for the MoS_2 detectors. As previously mentioned, my goal was to continue and go deeper on previous research on TMTES:PS based phototransistors as X-ray detectors. To place a TMTES:PS sample and electrically connect it, conductive silver paste and another experimental box were employed. In order to avoid the excitation of the active channel under visible light, the connection procedure was performed in the room illuminated by yellow light (i.e. no blue light).

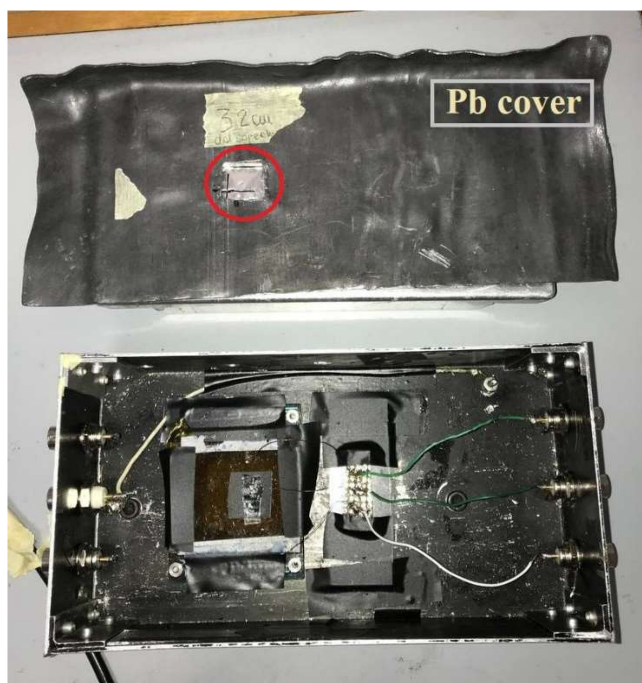

(a) **(b)**

Figure 3.9 Experimental setup for the X-ray characterization of the TMTES:PS TFTs: (**a**) a box for the X-ray detectors covered with a lead plate; the red circle indicates the window through which incoming X-ray radiation impinges on the detector. (**b**) silver paste RS 186-3600 to provide rigid connection between the micromanipulators and the device electrodes.

After a TMTES:PS based phototransistor was properly placed in the lead box (Fig. 3.9), it was mounted in front of the X-ray tube at the distance of 17 cm between the sample and the chassis of the X-ray tube. The X-ray measurement strategy was basically the same as for the MoS_2 samples and included the following steps:

1) Initially, the transfer characteristics in saturation regime are collected in the dark to test the performance of a phototransistor.
2) Once it is verified that the device works properly, the X-ray radiation with different dose rate is induced. The biasing voltage in the X-ray tube is fixed at $V_{X\text{-}ray}$ = 40 kVp. The current between the cathode and the anode is equal to $I_{X\text{-}ray}$ = 500 μA, 350 μA, 200 μA and 100 μA. The incident radiation is emitted in the form of periodic pulses of 60 seconds in *on*-mode and 60 seconds in *off*-mode. At least four photocurrent peaks should be registered. To obtain stable dark current of a phototransistor and also to test the repeatability and stability of the detector. The first photocurrent peak should not be considered as a reliable signal, since during the first X-ray pulse, the photogenerated charge carriers start to fill traps in the active channel, which reduces the collected signal.
3) During the X-ray measurements, the phototransistor is biased at gate voltage V_{GS} = -2.5 V and at drain-source voltage V_{DS} = -10 V.

Chapter 4 Results for MoS_2-based X-ray detectors

4.1 Electrical characterization of the MoS_2 detectors

The MoS2-based detectors described in Section 3.2 were firstly characterized by electrical measurements and the following parameters have been extracted from the acquired curves:

- ON/OFF ratio
- Subthreshold swing (*SS*)
- Mobility of the majority charge carriers μ
- Threshold voltage V_{th}

According to Eq. 2.9, The ON/OFF ratio is calculated via transfer characteristics in saturation regime and it is defined as the ratio between the current $\left|I_{DS}^{ON}\right|$ in the ON regime and the analogous current $\left|I_{DS}^{OFF}\right|$ in the OFF regime of a transistor. To evaluate the ratio, I decided to regard the highest $|I_{DS}|$ value as the ON-regime current, whereas the OFF-regime current was calculated as the average current in the V_{GS} range before the subthreshold region of $|I_{DS}|$ starts. To summarize:

$$\frac{ON}{OFF} = \frac{\left|I_{DS}^{ON}\right|}{\left|I_{DS}^{OFF}\right|} \qquad 4.1$$

$$I_{DS}^{ON} = I_{DS}^{max}\big|_{[-60,+60]\,V}$$

$$I_{DS}^{OFF} = \langle I_{DS}\rangle_{[-60\,V,\ subthreshold]}$$

The subthreshold swing *SS* was extracted from the same transfer characteristics in saturation regime. According to Eq. 2.8, *SS* is calculated as the inverse of the slope of the linear fit of I_{DS} (V_{GS}) in the subthreshold region. In order to calculate the mobility μ and threshold voltage V_{th} of a TFT, I plotted the function of $\sqrt{I_{DS}}\,(V_{DS})$ and fitted it with a linear function. According to Eq. 2.5 and also to Eq. 2.6 from Chapter 2, the slope and intercept of the linear fit allowed me to extract μ and V_{th} for a single device:

$$\sqrt{|I_{DS}|} = AV_{GS} - B, \quad A = \frac{d\sqrt{|I_{DS}|}}{dV_{GS}} \quad \rightarrow \quad \mu = \frac{2L}{WC_i}A^2, \quad V_{th} = -\frac{B}{A}$$

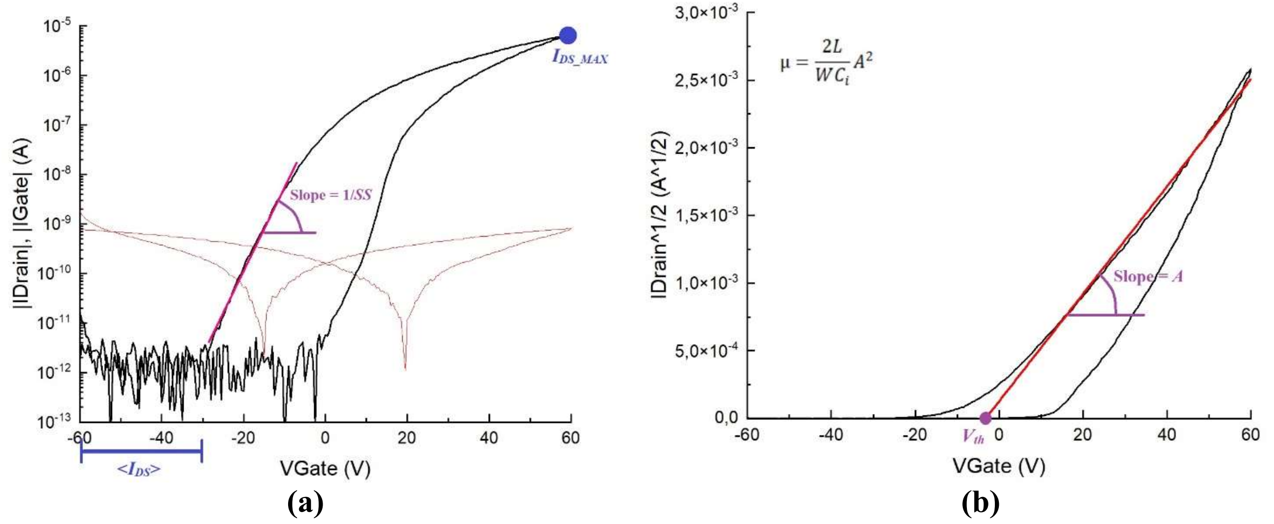

(a) **(b)**

Figure 4.1 Transfer characteristics in saturation regime of a typical MoS_2 TFT, from which electrical parameters are calculated. The forward sweep (from -60 V to +60 V) is considered. In (**a**) the $|I_{DS}|(V_{GS})$ is depicted; the subthreshold region is fitted with a linear function (pink line), whose slope is the inverse of the subthreshold swing SS; the ON/OFF ratio was evaluated as the ratio between the maximum I_{DS_MAX} value and the average value $<I_{DS}>$ in the OFF regime. In (**b**) the $\sqrt{I_{DS}}\,(V_{GS})$ dependence is fitted with a linear function (red curve). The slope A is used to determine the mobility μ, whereas the threshold voltage V_{th} is determined as the intersection of the linear fit with the V_{GS} axis.

According to these equations, the main four electrical parameters were calculated for each working device from its transfer characteristics (Fig. 4.1). As a result, the average ON/OFF ratio estimated as $(0.3 \pm 0.2) \times 10^6$, has the order of magnitude of 10^5 for the major part of the batch. The subthreshold swing SS has the average value of 4.3 ± 1.3 V/dec. The average threshold voltage was estimated over the whole set to have the average value of $-(10 \pm 2)$ V.

Lastly, to calculate the mobility μ for each TFT, firstly, I evaluated the dielectric capacitance per unit area C_i of a device. Since a typical device structure includes two insulating layers of BCB (50 nm thick) and SiO_x (278 nm thick), normally a series of two planar capacitors should be considered. Nevertheless, due to superior thickness of the SiO_x layer, the total dielectric capacitance per unit area was approximated to that of solely SiO_x insulator according to Eq. 2.7:

$$C_i = \frac{\varepsilon_0 \varepsilon_r}{d}$$

where $\varepsilon_0 = 8.85 \times 10^{-1}$ F/m is the permittivity of vacuum, ε_r is the dielectric constant of SiOx and d is the thickness of the insulating layer. Considering SiO_2 as the dielectric material for the MoS_2-based devices, the dielectric constant at room temperature was estimated as $\varepsilon_r = \varepsilon_r(\mathrm{SiO_2}) = 3.9$ [53], [54]. The thickness of the SiO_2 insulating layer is $d_{SiO2} = 278$ nm for each device in the batch. Therefore, the capacitance per unit area was calculated to be $C_i = 0.0124$ μF/cm^2 for all MoS_2-based detectors.

Once the capacitance per unit area C_i was found and since the active channel length L and width W had been provided by Professor Tamayo group, the calculation of the mobility μ was finally accomplished. As a result, the average mobility was estimated as 0.5 ± 0.2 $cm^2/(V \cdot s)$. For a more concise overview, the results of the IV characterization of the MoS_2-based X-ray detectors are presented in a table below.

ON/OFF	*SS* (V/dec)	V_{th} (V)	μ ($cm^2/(V \cdot s)$)
$(0.3 \pm 0.2) \times 10^6$	4.3 ± 1.3	$-(10 \pm 2)$	0.5 ± 0.2

Table 1 Electrical characterization results for the MoS_2-based TFTs. The quantities are averaged over the whole batch, the errors indicated represent the standard deviation error.

4.2 X-ray measurements of the MoS_2-based detectors

Prior to the calculation procedure, it is necessary to convert the applied characteristics of the X-ray tube, such as the current $I_{X\text{-}ray}$ and the voltage $V_{X\text{-}ray}$ that were applied during the X-ray emission, to the dose rate *DR* values. Such operation was fulfilled with a *calibration plot* which had been formerly obtained in the laboratory and which was presented in Section 3.1 (Fig. 3.4). The dependence of *DR* on both $I_{X\text{-}ray}$ and $V_{X\text{-}ray}$ was calculated by using Eq. 3.2 from for $V_{X\text{-}ray} = 150$ kV in relation to the distance of 32 cm between the chassis and a MoS_2 sample. The results are provided in

Table 2.

$V_{X\text{-}ray}$ (kV)	$I_{X\text{-}ray}$ (µA)	*DR* (mGy/s)
150	100	1.1
	200	2.2
	300	3.4
	400	4.6
	500	5.7

Table 2 Dose rate *DR* calculated at different $I_{X\text{-}ray}$ and $V_{X\text{-}ray}$ at the distance of 32 cm from the chassis of the X-ray tube.

In order to obtain the highest photocurrent from I_{DS}, the photoconductive gain must be taken into consideration. As was mentioned in Section 2.3.1 in Chapter 2, in phototransistors the increasing the gate polarization V_{GS} leads to the enhancement of the photoconductive gain G, which in its turn increases the photocurrent signal. At the same time, increasing V_{GS} also leads to the rise of drift dark current, which shall hide the relatively small photocurrent ($I_{PH} \sim 10^{-10}$ A) due to the larger order of $|I_{DS}|$ magnitude. As a result, some kind of "trade-off" between the photoconductive gain and the magnitude of $|I_{DS}|$ must be accomplished. To do this, we made a condition to keep drain current in the order of $I_{DS} \sim 10^{-6}$ A for each MoS_2 device by operating V_{GS} is a corresponding range. In certain cases,

the required I_{DS} order of magnitude was obtained by biasing the device at V_{GS} in the range of [30 – 40] V. After the measurement of the detector's response to X-rays, the transfer characteristics in saturation regime were measured for each TFT in dark in order to see if any degradation of the device was present. As shown in Fig. 4.2(a), the performance of a typical device did not really change after the irradiation, indicating a good tolerance to X-rays.

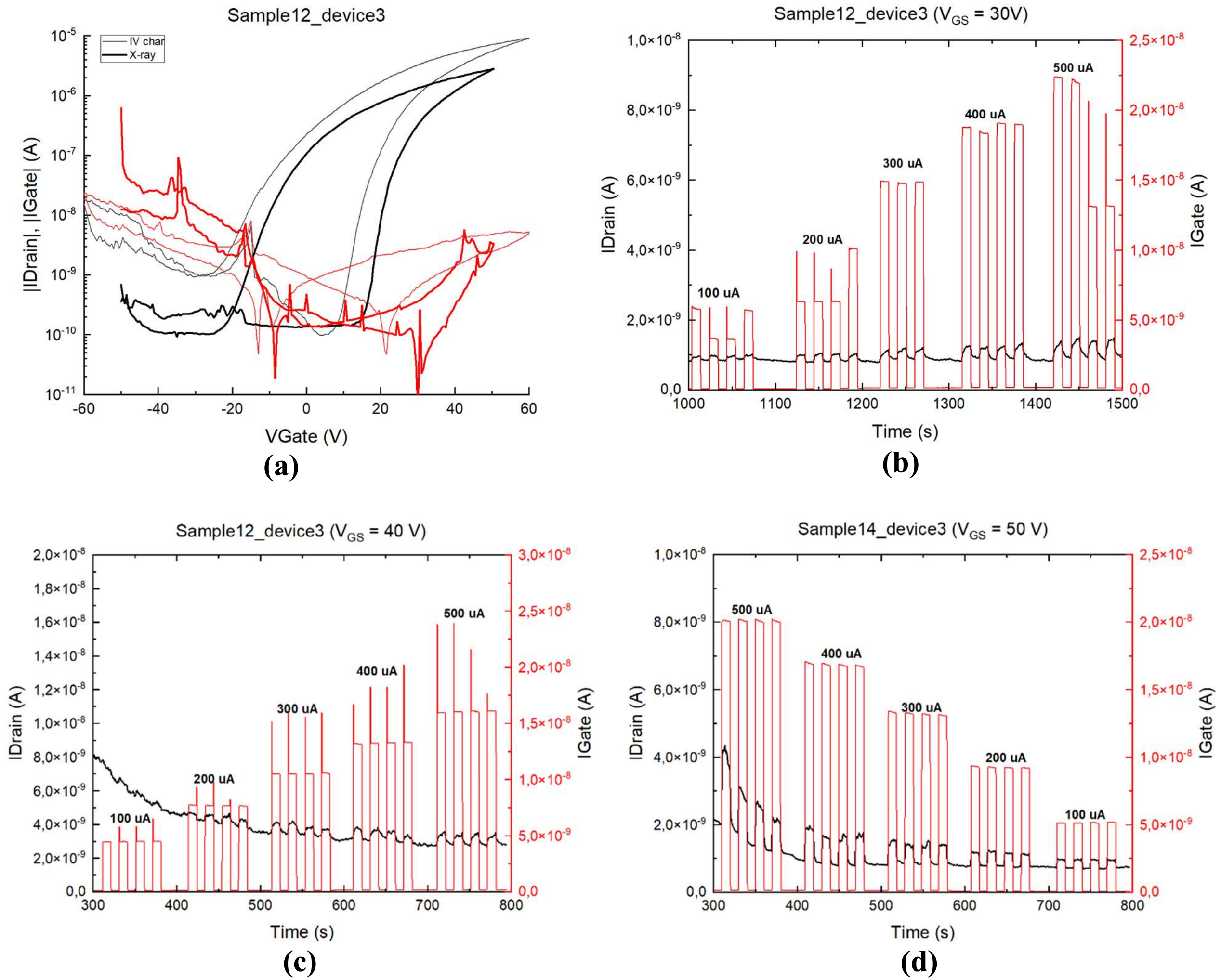

Figure 4.2 X-ray characterization results: (**a**) transfer characteristics in saturation regime for a photodetector *Sample12_device3* obtained during the electrical characterization (gray curve) and after the X-ray measurement (black curve). (**b**) and (**c**) depict the DC characterization at V_{GS} pf 30 and 40 V, respectively, of the *Sample12_device3* TFT under X-ray pulses indicated by peaks in I_{DS} (black curve) and I_{GS} (red curve). (**c**) demonstrates the X-ray characterization at V_{GS} = 50 V for a photodetector denoted as *Sample14_device3*.

To study the effect of V_{GS} on the X-Ray response, I varied the biasing of the gate electrode as follow: V_{GS} = 30 V, V_{GS} = 40 V, V_{GS} = 50 V. Typical photoresponse is depicted in Fig. 4.2 for the MoS_2 detectors denoted as *Sample12_device3* (Fig. 4.2(b, c)) and *Sample14_device3* (Fig. 4.2(d)). The drain voltage has been kept constant (V_{DS} = 1 V). According to the analysis strategy indicated in Chapter 3, the obtained $I_{DS}(t)$ curves were normalized with a polynomial function of degree 2 or an

exponential function. For each set of peaks corresponding to specific dose rate, the average photocurrent I_{PH} was calculated. After that the dependence of the average photocurrent I_{PH} on the dose rate was fitted with a linear function, as reported in Fig. 4.3 for each V_{GS}.

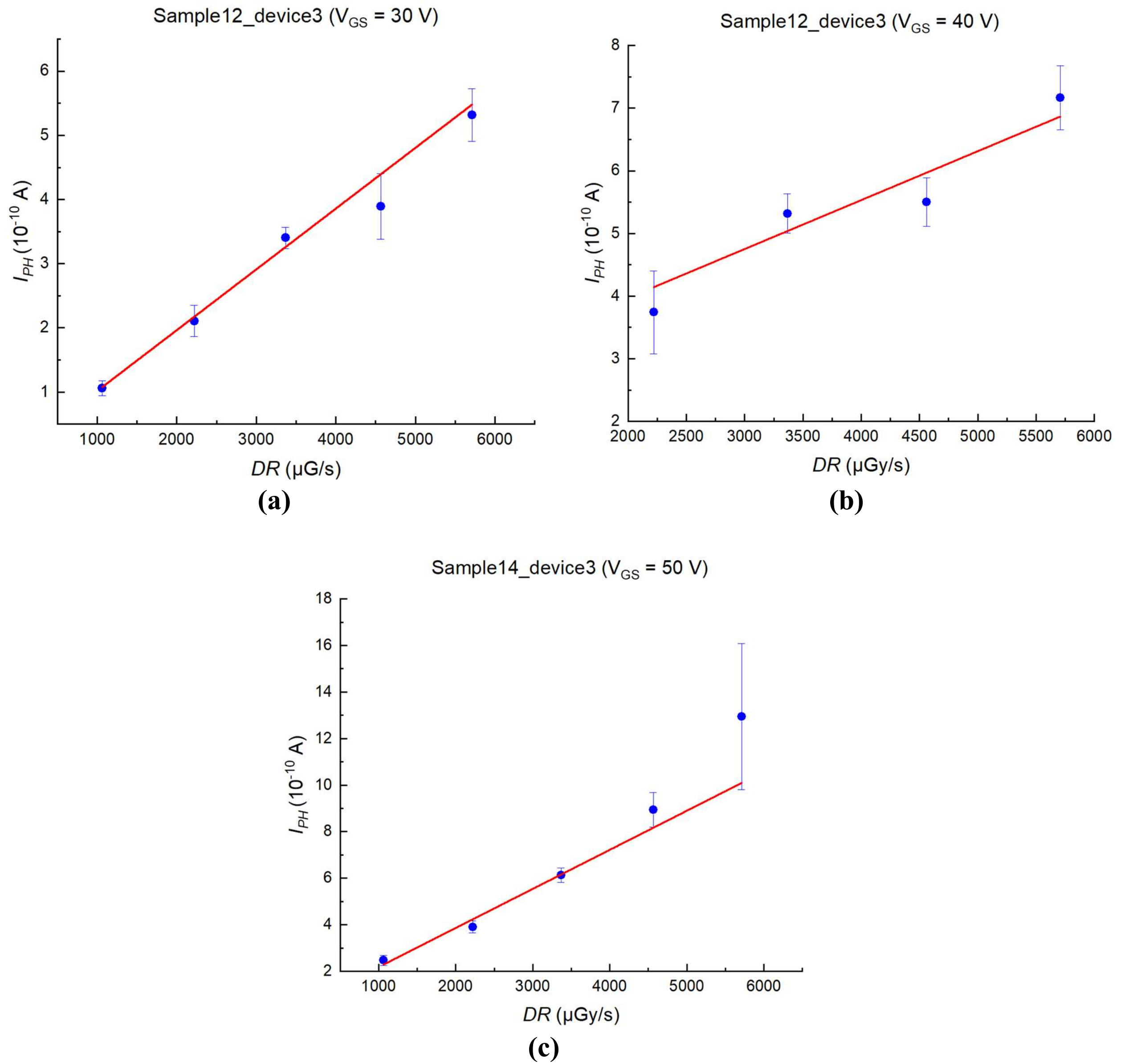

Figure 4.3 Photocurrent dependence on the dose rate for the aforementioned photodetectors *Sample12_device3* at V_{GS} = 30 V (**a**) and V_{GS} = 40 V (**b**) and *Sample14_device3* at V_{GS} = 50 V.

Subsequently, the average sensitivity per unit volume was found to lie in the range between 10^{11} and 10^{12} μC/(Gy·cm^3) for each photodetector under analysis. For example, the device denoted as *Sample12_device3* exhibited the sensitivity of (3.8 ± 0.2) × 10^{11} μC/(Gy·cm^3) with the gate being biased at V_{GS} = 30 V and that of (3.1 ± 1.0) × 10^{11} μC/(Gy·cm^3) at V_{GS} = 40 V. Similarly, the sensitivity of another device called *Sample14_device3* was estimated as (6.5 ± 0.7) × 10^{11} μC/(Gy·cm^3).

The further objective of the X-ray characterization was to calculate the sensitivity of a device for different V_{GS} and to extract possible relation between S and V_{GS}. For this purpose, the previously mentioned device *Sample12_device3* was considered due to its superior performance. The TFT was exposed to the ionizing radiation under the constant V_{DS} bias of 1V and the gate voltage of V_{GS} = 1, 2, 3, 5, 10, 15, 20, 25, 30, 35, 40, 45 and 50 V. The result is presented in Fig 4.4.

As seen, the order of magnitude of the sensitivity per unit volume is consistently equal to 10^{11} μC/(Gy·cm^3), reaffirming the remarkable efficiency of the MoS_2-based detectors. Nevertheless, with the elevation of V_{GS}, a reduction of the device sensitivity is observed. Such phenomenon of sensitivity lowering might be attributed to high deviation of the photocurrent due to increase of thermally induced noise signal at high V_{GS}. However, a more probable explanation for the decrease in sensitivity is the deterioration of the device performance due to the introduction of additional trapping states for majority carriers by the incident radiation. This hypothesis is further supported by the slower saturation of the photocurrent signal at higher gate voltage (Fig. 4.4(c)), which indicates an increased number of traps hindering the collection of the photogenerated charges.

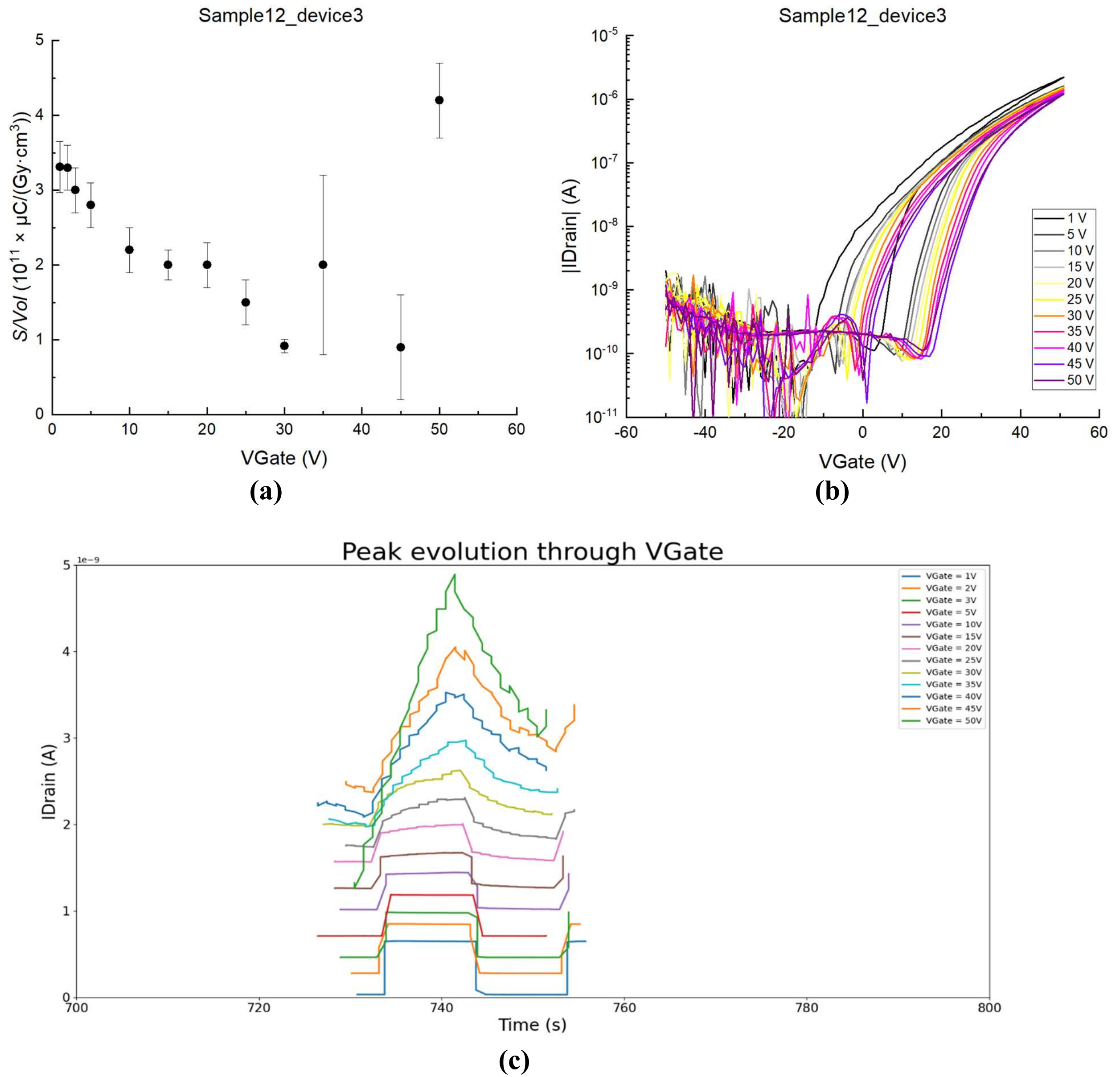

Figure 4.4 X-ray characterization of the MoS_2 photodetector *Sample12_device3* biased at V_{DS} = 1 V and at different gate voltage V_{GS}: (**a**) sensitivity per volume as a function of V_{GS}; (**b**) transfer characteristics in saturation regime after each X-ray measurement; (**c**) evolution of the photocurrent peak form with increasing of V_{GS}.

As V_{GS} increases, the photocurrent peak form also changes from the rectangular one to the angular shape with slower increase of I_{DS} at impinging radiation and slower relaxation, when the radiation is switched off. The explanation of such tendency could be the enlarged number trapping states induced by irradiation, thus, reducing the collected photocurrent with postponed saturation.

To test the device performance during the X-ray measurement, its electrical characterization was carried out after each radiation cycle. As seen from Fig. 4.4(b), along with the measurements, the transfer characteristics curve slightly shifts with the approximate step of 1-2 V in the positive V_{GS} direction, while the maximum value of I_{DS} at V_{GS} = 50 V moderately decreases by 1 µA between the

initial and final obtained transfer characteristics. Such tendency could signify the constant, yet non-dramatic degradation of the MoS_2 performance under X-rays.

4.3 Comparison with literature

To assess the reliability of both electrical and X-ray characterization outputs for MoS_2-based photodetectors, reference is made to papers which were already highlighted in Chapter 2. According to Hai Li *et al.*, the charge carrier mobility in fabricated TFTs ranged from 0.03 to 0.22 $cm^2/(V \cdot s)$ for the number of MoS_2 layers from 1 to 4, respectively. Additionally, the ON/OFF ratio was exceeding 10^3 with the tendency to decrease for a monolayer MoS_2 film [51]. In line with the aforementioned findings, Zongyou Yin and colleagues reported mobility of 0.11 $cm^2/(V \cdot s)$ for a single-layer MoS_2-based FET, with an estimated ON/OFF ratio of the order of $\sim 10^3$ [50].

In contrast, the research conducted B. Radisavljevic *et al.*, present a distinct scenario, where they examined thin-film transistors based on monolayer MoS_2 films. In their study, the typical mobility increased by one order of magnitude, ranging from 0.1 to 10 $cm^2/(V \cdot s)$, with an ON/OFF ratio proportional to 10^6 [52]. Finally, in the work carried out by Ji Heon Kim *et al.*, reported superior mobility values, ranging from 10 to 18 $cm^2/(V \cdot s)$ by varying the number of MoS_2 layers from 1 to 6. The measured transfer curves exhibited a high ON/OFF ratio of the order of magnitude $\sim 10^7$. Additionally, the average subthreshold swing *SS* values for 1L, 3L and 6L MoS_2 TFTs were calculated as 0.92, 0.92 and 1.41 V/dec, respectively [49].

As one can see, the electrical characteristics of thin-film transistors based on MoS_2 mono- and multilayer active channel display noticeable variety on orders of magnitude across different studies. Such discrepancy may be attributed to the inherent instability of few-layer MoS_2 films that could be caused by imperfections induced by the commonly used mechanical exfoliation deposition method for TMDC-based TFTs fabrication. Regarding specifically the results obtained for the MoS_2 TFTs in my research, the average mobility of 0.5 ± 0.2 $cm^2/(V \cdot s)$ aligns well with the reported intervals from outer studies. The measured average ON/OFF ratio also lies within the range of 10^3-10^6, adding credibility to the calculated value. Nevertheless, because of significant deviation in electrical parameters, additional investigations into the performance of MoS_2-based TFTs are required.

In evaluating the efficiency of MoS_2 photodetectors exposed to X-ray radiation, it is convenient to compare the device sensitivity with the findings reported by Tafelli *et al.* in [39]. This research is already discussed in Chapter 2 and regarded MoS_2 monolayer structures in photoconductor X-ray detectors. The photodetectors operated in conjunction with a scintillator film, which absorbed minimal amount of X-rays (less than 4%), which allows to approximate the detection mechanism to the direct one. Nonetheless, the presence of the film still increased the total photocurrent by a factor

of 3. Consequently, the sensitivity per unit volume for such device was estimated to be proportional to 10^8-10^9 μC/(Gy·cm^3) with the maximum sensitivity value of 2.3×10^9 μC/(Gy·cm^3). By comparing the photoconductor performance with the characterized MoS_2 TFTs, it is seen that the latter have the average sensitivity exceeding that reported by Taffelli *et al.* by 2 orders of magnitude. This difference in sensitivity may be attributed to variations in the density of charge carrier traps between the samples, which could be induced by the differences in the semiconductor deposition conditions. Furthermore, the device architecture may also influence calculated sensitivity values, the X-ray detection pergformance by the field effect induced by the gate electrode.

4.4 Side Effects of the MoS_2 device characterization

Even though the MoS_2-based photodetectors yield satisfactory properties, some non - ideality issues have also occurred along with the measurements. First of all, the majority of the devices performed hysteresis of different extent (Fig. 4.5) during their electrical characterization. It is noteworthy to mention that the hysteresis loop was present mainly in the transfer characteristics, while the output characteristics did not exhibit any difference in I_{DS} versus V_{DS} behaviour at constant V_{GS} between forward (from -60 V to +60 V) and backward (from +60V to -60 V) sweeps of V_{DS}. The explanation to such phenomenon could be a high density of traps in the MoS_2 semiconducting layer, which could lower the density of free charge carriers in the conductive channel when a TFT is switched to the ON-regime during the forward sweep. Therefore, when the gate voltage starts to decrease during the backward sweep, charge carriers become trapped decreasing the I_{DS} current in relation to that during the forward sweep. The high density of traps can also be confirmed by quite long relaxation of I_{DS} in the DC characterization of a TFTs upon X-ray exposure. In particular, before an initial X-ray pulse, an X-ray detector was held in the dark for some time to stabilize the drain-source current, until it becomes more or less constant with time. In case of the MoS_2-based X-ray detectors, 10 minutes was the time needed for the current to stabilize, while it decreased down to some orders of magnitude (from ~10^{-6} A to ~10^{-9} A). Such slow relaxation can also represent significant amount of trapping states that become filled up by the majority charge carriers along their path between the drain and source.

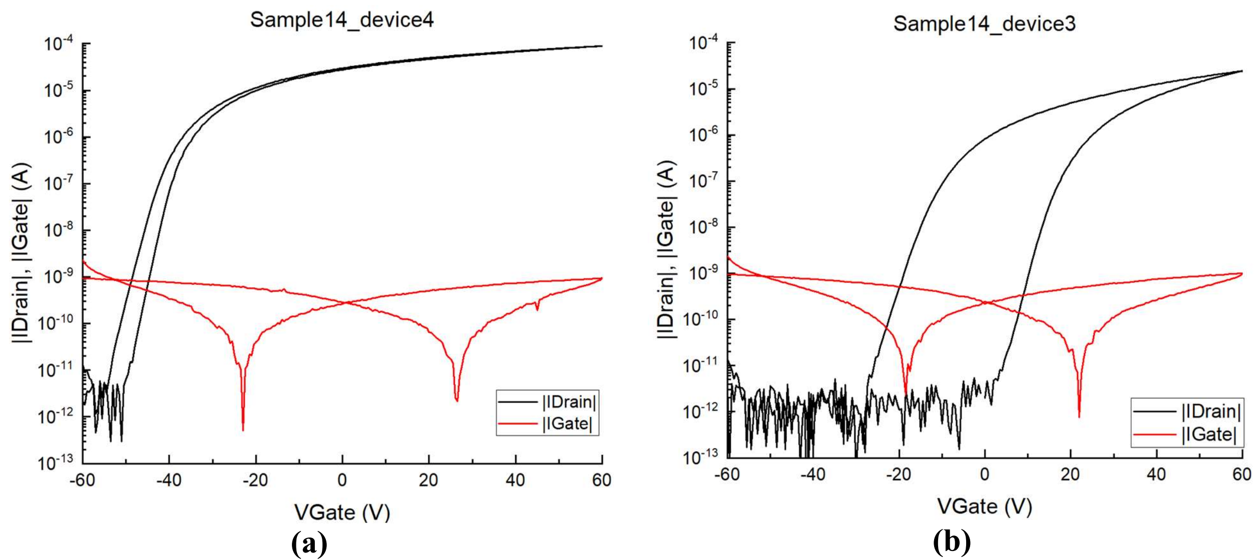

Figure 4.5 Transfer characteristics in saturation regime (indicated as *trfSat*) of two MoS_2-based TFTs denoted as *Sample14_device4* (**a**) and *Sample14_device3* (**b**) constructed on the same Si/SiO_x substrate. The red curves describe the behaviour of the leakage current $|I_{GS}|$ through the insulating layer. The left graph depicts a small hysteresis, while in the right graph the hysteresis loop is particularly large.

The hysteresis phenomenon noticeably complicates the calculation of different electrical parameters, such as subthreshold swing (*SS*) or threshold voltage V_{th}. As it was discussed in Section 2.2.1, their values are based on the slope and the intercept of a linear fit applied to the I_{DS} curve, which now represents typically two shifted curves. To overcome the uncertainty of the analysis of the curves, it was decided to fit the forward sweep part (from -60 V to +60 V) of a hysteresis loop.

More interestingly, five samples from the characterized set demonstrated an anomalous effect: when the X-ray radiation is switched on, the drain-source current I_{DS} decreases at greater slope than in the dark. Such tendency can be noticed for *Sample6_device1* or *Sample1_device3* at $I_{X\text{-}ray}$ = 500 μA (Fig. 4.6). In these examples I_{DS} evolves in the form of “steps” that are directed downwards. Alternatively, I_{DS} can abruptly fall down when the X-ray radiation impinges on a device, and rises up again, when the radiation is shut. Such cases are presented for *Sample12_device4* and *Sample14_device4*.

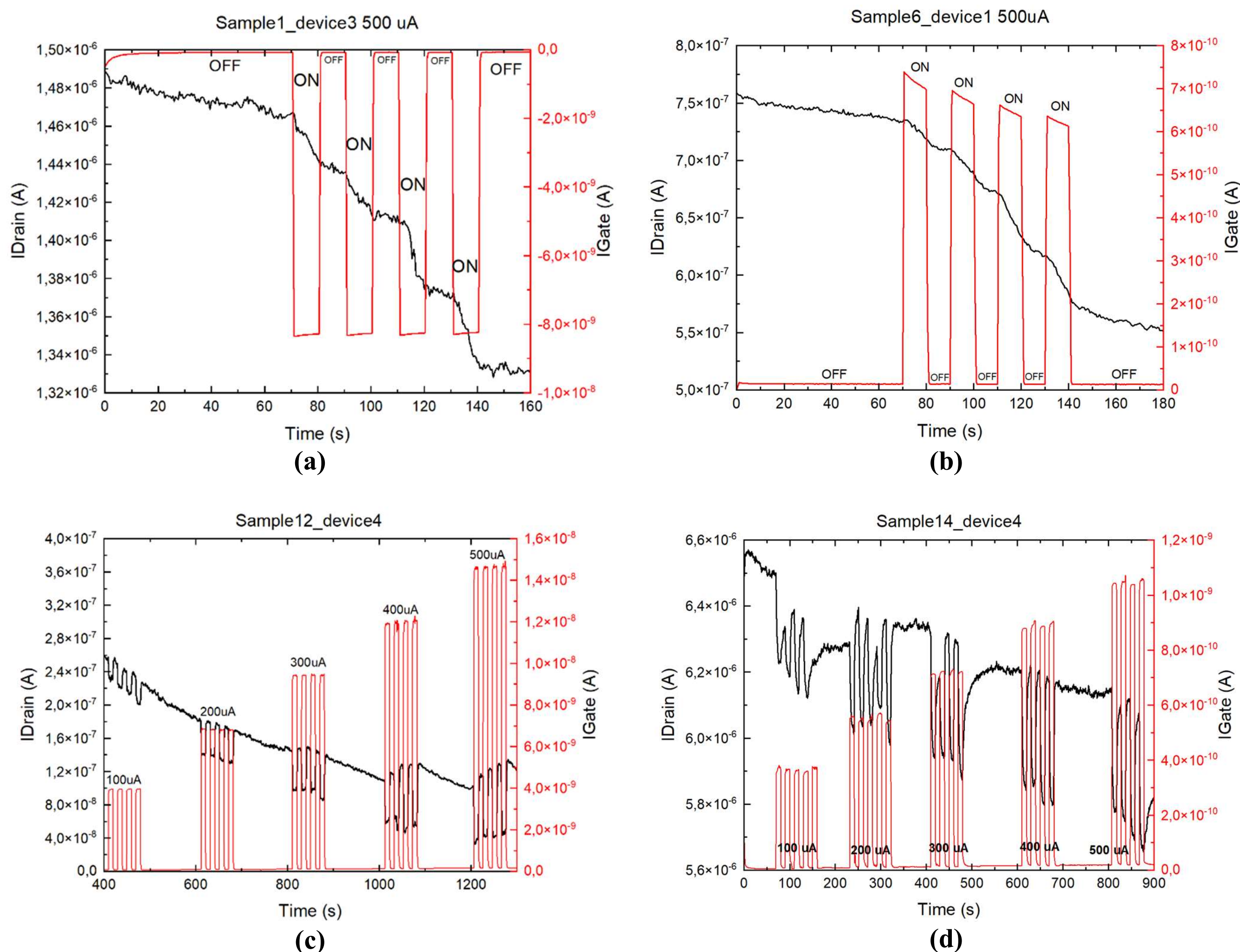

Figure 4.6 The side effect of negative photoresponse occurred during the X-ray characterization of the MoS_2-based detectors. In (**a**) and (**b**) I_{DS} consistently drops down without going to its former value, whereas in (**c**) and (**d**) the photoresponse is presented in the form of negative photocurrent peaks.

The comprehensive understanding of this "negative photocurrent" phenomena is not fully formed yet, hence, further thorough investigation into these anomalies is required to diminish the frequency of their occurrence and to enhance the detector performance.

Chapter 5 Results for TMTES:PS samples

The TMTES:PS phototransistor performance was firstly electrically characterized and after that the sensitivity of the active channel under X-ray radiation was derived from DC measurements upon X-ray pulses.

In this chapter I will first discuss the electrical parameters that were calculated from the electrical characterization of the phototransistors and how these parameters change with the TMTES:PS ratio. I will also discuss common features and anomalies shown up in some device performance during this characterization. In the second section I will describe the results from the DC measurements under X-rays and how the sensitivity was calculated. In the concluding section, I will evaluate the calculated electrical parameters and sensitivity of the TMTES:PS-based devices in comparison to results presented in literature and in the study conducted by previous studies. Finally, I will set side by side the TMTES:PS phototransistors with their MoS_2-based counterparts and assess their respective capabilities under ionizing radiation.

5.1 Electrical characterization of the TMTES:PS detectors

5.1.1 Overview on the device performance and results

The batch included in total 32 TMTES:PS based phototransistors, 30 of which underwent the IV characterization. As a consequence, almost each device demonstrated proper behaviour both in transfer characteristics (in saturation and linear regimes) and in output characteristics demonstrating an excellent yield. To begin with, the devices exhibit a notable absence of hysteresis, indicating stable and predictable functioning in different operation conditions. The leakage through the SiO_2 insulating layer is moderate and on the average is in the range of $|I_{GS}| \sim 10^{-9}$-10^{-8} A, which demonstrates good insulation performance. Besides, the TMTES:PS phototransistors show proper output characteristics, in which both linear and saturation regions are clearly depicted. Only at the TMTES:PS ratio of 39:1 (i.e. the lowest concentration of PS in the TMTES:PS blend), the field effect is weakly present at the gate voltage V_{GS} below -10 V and the device performs as a resistor. Finally, the subthreshold swing below 5 V dec^{-1} distinctly represented the states of operation in both the OFF- and ON-regimes of a transistor.

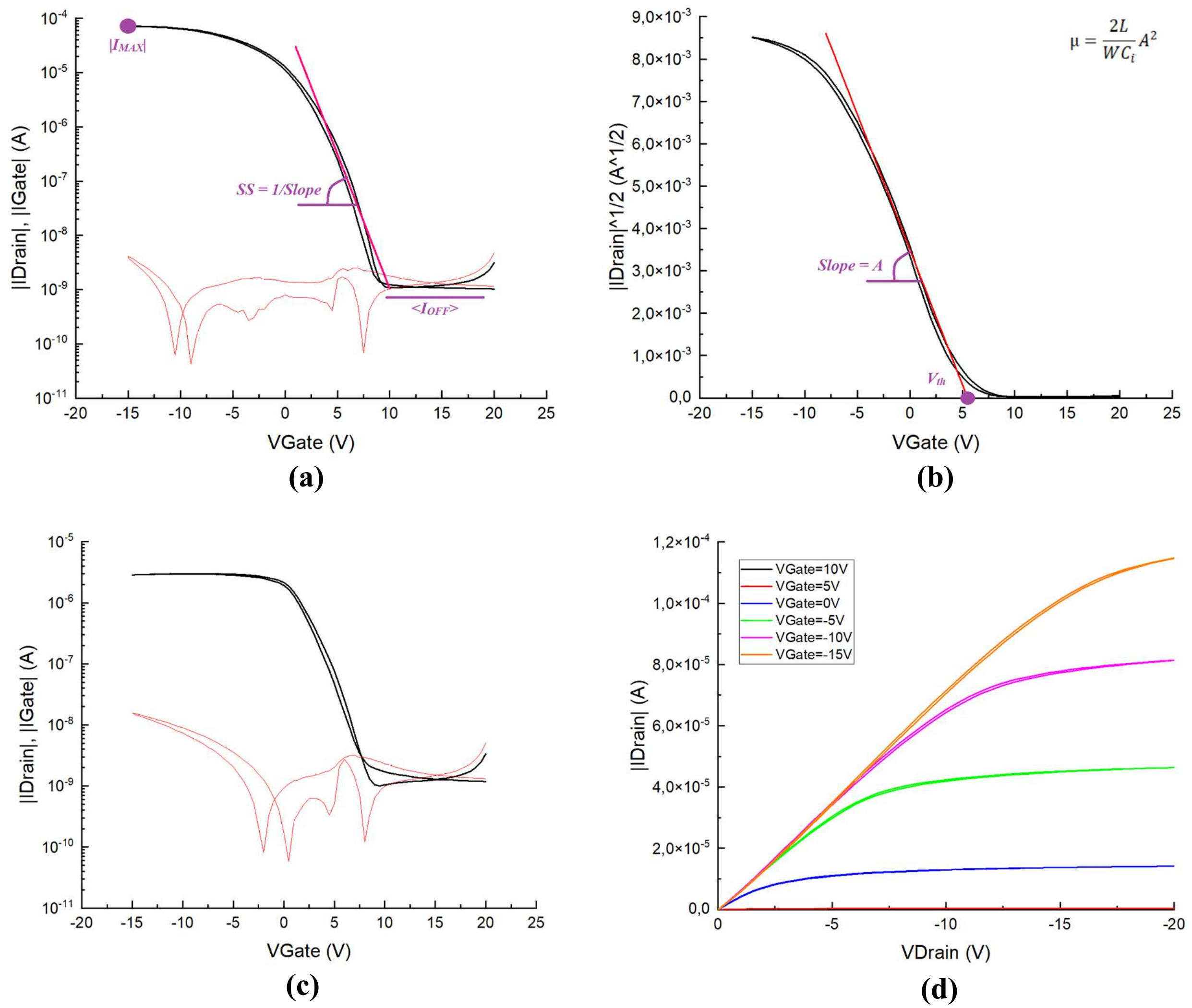

Figure 5.1 Typical electrical characterization curves of the TMTES:PS devices. Transfer characteristics in saturation regime in (**a**) and (**b**) are used to calculate the electrical parameters of a phototransistor: ON/OFF ratio, subthreshold swing *SS*, threshold voltage V_{th} and mobility μ. In (**c**) transfer characteristics in linear regime are depicted. In (**d**) the output characteristics are reported; the linear and saturation regimes are clearly seen for each V_{GS}.

Analogously to the MoS_2-based TFTs, the parameters to derive were the ON/OFF ratio, subthreshold swing *SS*, threshold voltage V_{th} and mobility μ. For this purpose, the same equations Eq. 2.4, 2.5, 2.6 and 2.8 from Chapter 2 were used in relation to the obtained transfer characteristics in saturation regime (Fig. 5.1). To calculate the mobility, the dielectric capacitance per unit area was estimated as C_i = 17.3 nF/cm^2 for each device.

5.1.2 Dependence of the electrical parameters on the TMTES:PS ratio

As a result, the average value of the four main parameters was calculated for each ratio of TMTES:PS batch. The results are depicted in Table 3.

MW	Ratio	ON/OFF	*SS* (V/dec)	V_{th} (V)	μ ($cm^2/(V\cdot s)$)
280 kDa	**17:3**	$(95 \pm 26) \times 10^3$	0.8 ± 0.2	1.5 ± 0.3	0.7 ± 0.3
	9:1	$(14 \pm 8) \times 10^3$	0.9 ± 0.3	2.7 ± 1.9	0.4 ± 0.3
	19:1	$(40 \pm 20) \times 10^3$	2.0 ± 0.4	5.8 ± 0.3	0.40 ± 0.05
	39:1	$(13 \pm 9) \times 10^3$	3.5 ± 0.6	11 ± 3	0.22 ± 0.10

Table 3 Average electrical parameters of the TMTES:PS X-ray detectors calculated for each ratio.

As seen, the ON/OFF ratio is noticeably deviated at each ratio with no possibility to provide any concrete tendency along the change of TMTES:PS proportion. On the other hand, the subthreshold swing *SS* explicitly increases with the reduction of PS from 0.8 ± 0.3 V/dec for TMTES:PS = 17:3 to 3.5 ± 0.6 V/dec for TMTES:PS = 39:1. The threshold voltage also rises from 1.5 ± 0.3 V at TMTES:PS of 17:3 to 11 ± 3 V at TMTES:PS of 39:1. The mobility μ, on the contrary, depicted direct proportionality for the PS amount and decreased from 0.7 ± 0.3 $cm^2/(V\cdot s)$ at maximum TMTES:PS proportion of 17:3 to 0.22 ± 0.10 $cm^2/(V\cdot s)$ at the TMTES:PS ratio of 39:1. The corresponding dependence of the average electrical parameters on the TMTES:PS proportion is shown in Fig. 5.2.

The trend of mobility to rise with a higher proportion of polystyrene in the TMTES:PS blend clearly indicates the role of PS in passivation of the interfacial majority carrier trapping states in the semiconductor (see Section 2.6), which enhances the majority carrier mobility and thus, increases the sensitivity of the device.

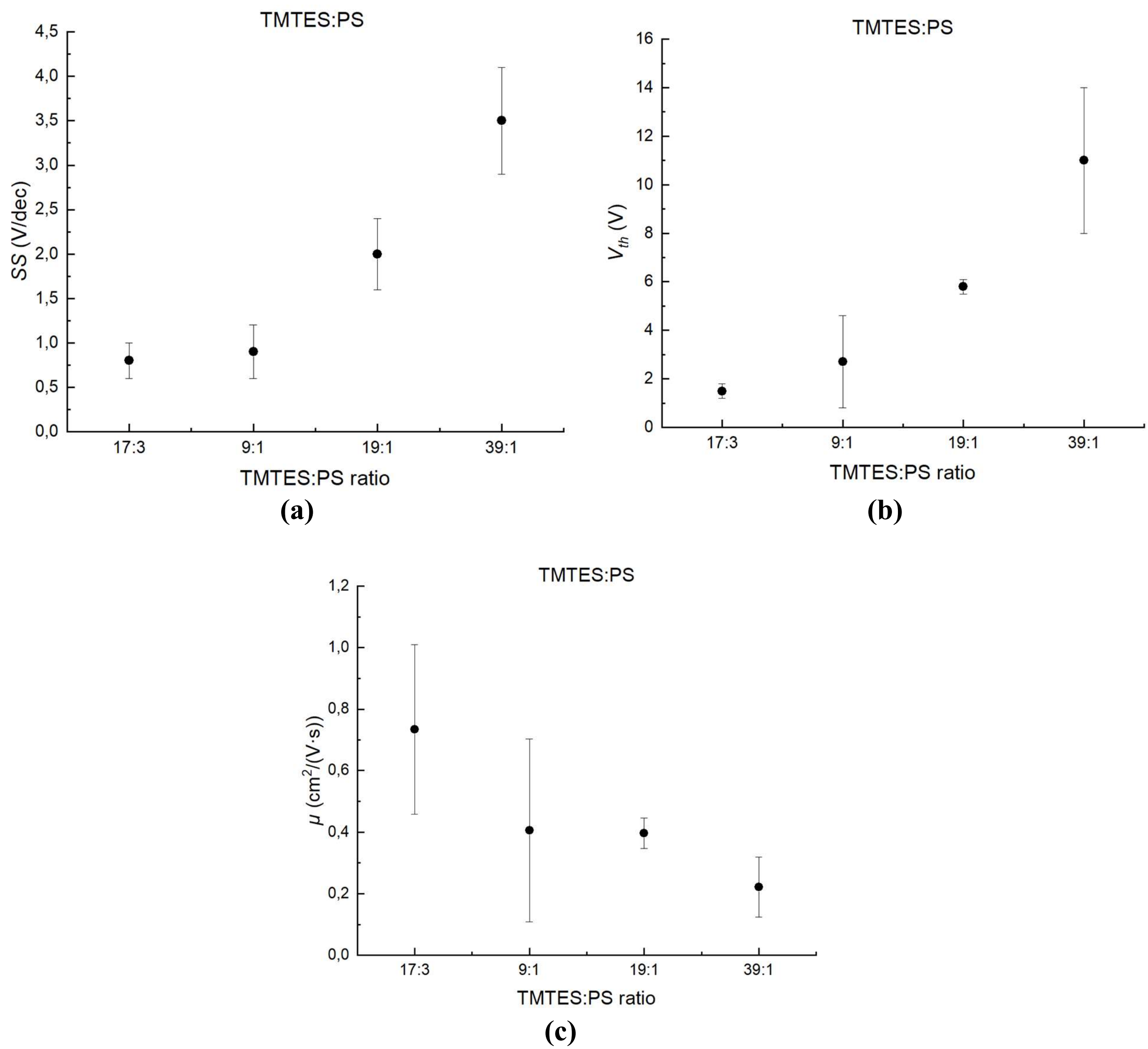

Figure 5.2 Dependence of average electrical parameters on the TMTES:PS ratio. In (**a**) and (**b**) the increase of subthreshold swing *SS* and threshold voltage V_{th}, respectively, at decreasing PS relative amount is shown. In (**c**) the mobility μ decreasing with the reduction of PS, is demonstrated.

5.2 X-ray measurement of the TMTES:PS detectors

The time period between the IV characterization and the X-ray measurements was approximately two weeks. Therefore, in order to verify if the electrical performance of the samples changed during the storage in ambient conditions and in dark, the transfer characteristics from the initial IV characterization and right before the X-ray exposure were compared. As a result, the majority of the samples exhibited a small shift towards the positive V_{GS} values with no drastic changes for each ratio (Fig. 5.3). Consequently, it is possible to assert that no significant semiconductor degradation was detected.

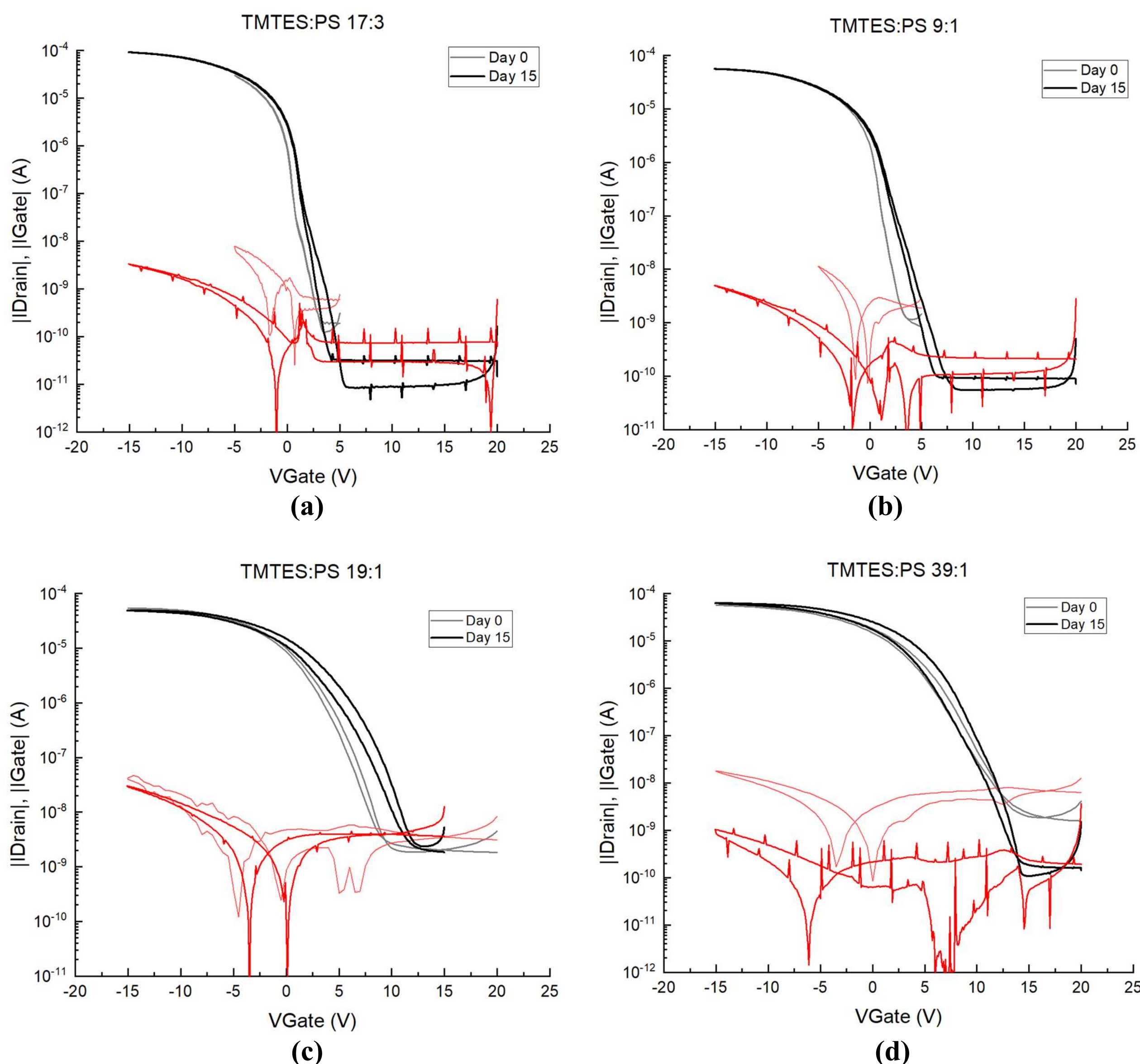

Figure 5.3 Transfer characteristics in saturation regime for the TMTES:PS samples obtained during the electrical characterization (gray and light red curves) and right before the X-ray measurements (black and red curves) after the period of two weeks of storage in ambient condition and in dark. Each graph depicts a typical trend for the TMTES:PS ratios of 17:3 (**a**), 9:1 (**b**), 19:1 (**c**) and 39:1 (**d**).

To perform the analysis on the X-ray measurements, first the X-ray tube current $I_{X\text{-}ray}$ was converted to the dose rate *DR* relatively to $V_{X\text{-}ray}$ = 40 kV and the distance of 17 cm between the chassis and the sample. To build the calibration plot, Eq. 3.2 (Section 3.1) was applied. The results are shown in Table 4.

$V_{X\text{-}ray}$ (kV)	$I_{X\text{-}ray}$ (μA)	*DR* (mGy/s)
40	100	1.3
	200	2.6
	350	4.6
	500	6.7

Table 4 Dose rate *DR* calculated at different $I_{X\text{-}ray}$ at the distance of 17 cm from the chassis of the X-ray tube.

The major issue during the X-ray characterization was the anomalous photoresponse of certain TMTES:PS detectors, which manifested itself in a decrease or complete drop of the absolute current $|I_{DS}|$ under the incident radiation. Such phenomenon had previously been detected in relation to the MoS_2-based devices. Regarding the TMTES:PS based samples, the non-ideal behaviour was initially slightly exhibited by the active channel of the 17:3 TMTES:PS proportion. For the 9:1 ratio (Fig. 5.4(b)), the "decreasing" photoresponse is explicitly shown, when after 20-30 seconds of irradiation, $|I_{DS}|$ begins to go down, even though the radiation is still switched on. When it comes to the TMTES:PS ratio of 19:1 (Fig. 5.4(c)), $|I_{DS}|$ reduces throughout the whole X-ray pulse and the photocurrent becomes completely negative. The tendency is only intensified for the 39:1 ratio (Fig. 5.4(d)).

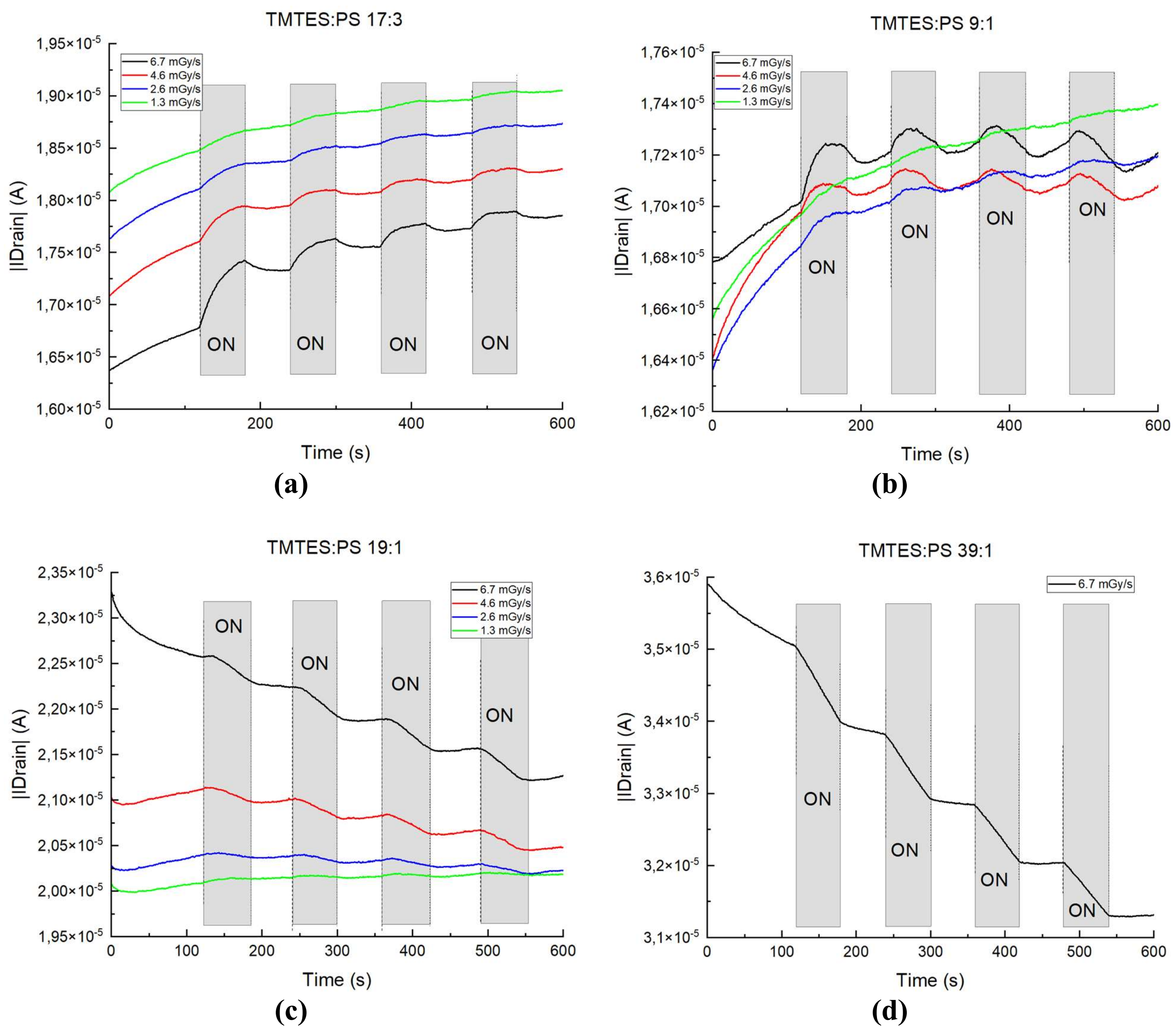

Figure 5.4 X-ray characterization for the TMTES:PS based phototransistors. The general form of $|I_{DS}|$ is depicted for the TMTES:PS ratio of 17:3 (**a**), 9:1 (**b**), 19:1 (**c**) and of 39:1 (**d**). As seen from the graphs, the "decreasing peaks" phenomenon starts to reveal itself relatively to the 9:1 proportion, where $|I_{DS}|$ first increases, but then drops down, even though the radiation is still switched on. Subsequently, for the TMTES:PS of both 19:1 and 39:1, the current decreases during the whole irradiation period.

Considering this anomalous behaviour, I was able to extract the sensitivity value only for the TMTES:PS ratio of 17:3 and 9:1. According to the same strategy applied for the MoS_2 samples, the dark current was normalized with a polynomial function of second order, as shown in Fig. 5.5(a, b). For each dose rate the average photocurrent I_{PH} was derived from the corresponding photoresponse peaks and the photocurrent versus dose rate plot was built for each device. The sensitivity was computed as the slope of the linear fitting function (Fig. 5.5(c)). In order to be independent on the area of the TMTES:PS active channel, the sensitivity per unit area was regarded as the final result.

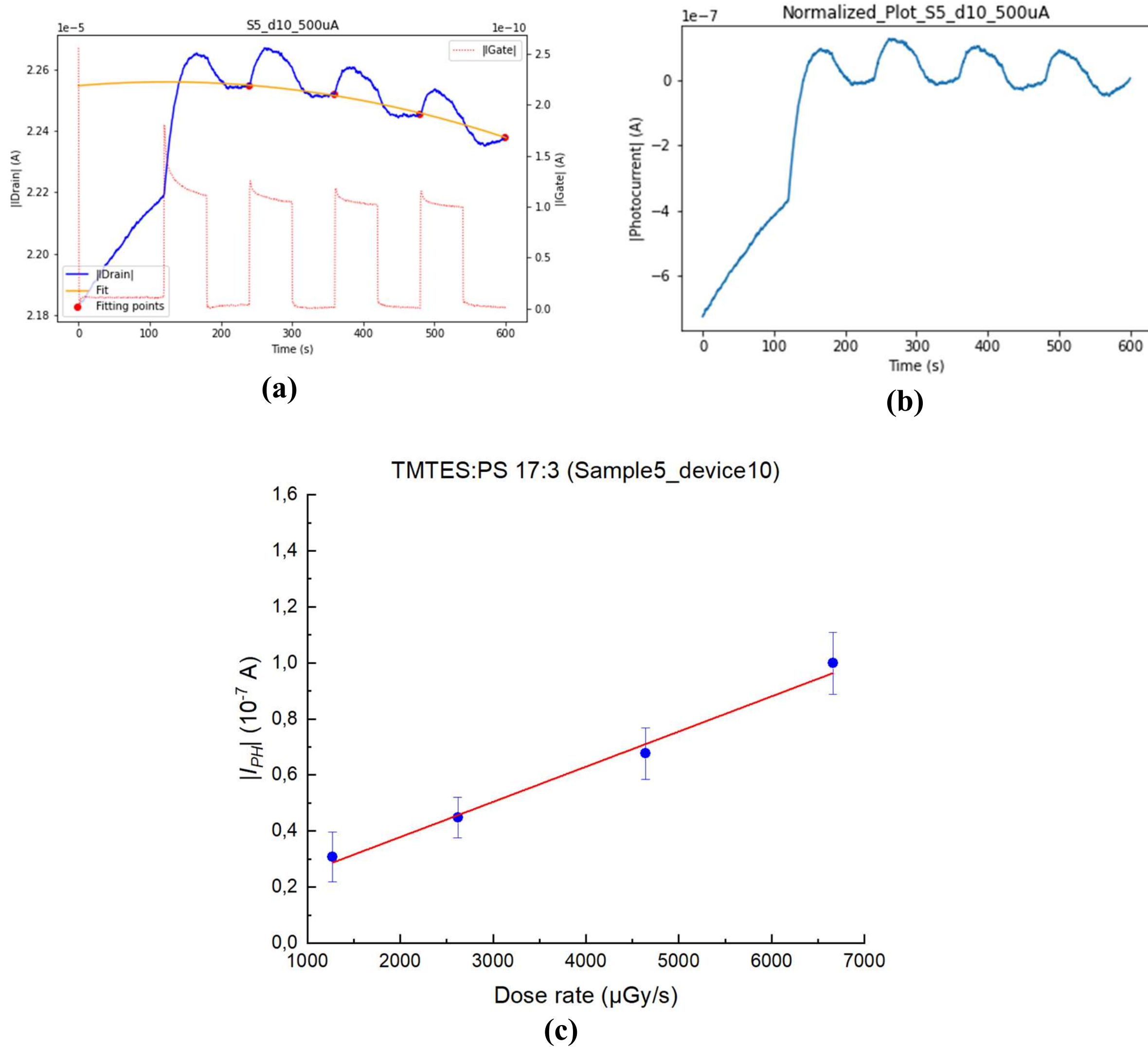

Figure 5.5 Normalized photocurrent peaks of the device denoted as *Sample5_device10* corresponding to the TMTES:PS ratio of 17:3: (**a**) raw $|I_{DS}|$ signal (blue) obtained at DR = 6.7 mGy/s, is normalized by a polynomial function of second degree (yellow) fitted with the time values (red dots) right before switching on the radiation (indicated by $|I_{GS}|$ (red dashes)). (**b**) normalized photocurrent peaks, whose height determines the photoresponse to X-rays. (**c**) The photocurrent versus dose rate scatter plot (blue dots) fitted with a linear function (red line). The sensitivity is determined as the slope of the fit.

Additionally, the average sensitivity per unit area was calculated for each TMTES:PS ratio. The results are demonstrated in Table 5. Since for TMTES:PS = 19:1 and 39:1 the photoresponse was completely negative, it was impossible to derive any sensitivity from the corresponding samples.

MW	Ratio	ON/OFF	*SS* (V/dec)	V_{th} (V)	μ ($cm^2/(V \cdot s)$)	*S/Area* ($10^3 \times \mu C/(Gy \cdot cm^2)$)
280 kDa	**17:3**	$(95 \pm 26) \times 10^3$	0.8 ± 0.2	1.5 ± 0.3	0.7 ± 0.3	3.4 ± 1.3
	9:1	$(14 \pm 8) \times 10^3$	0.9 ± 0.3	2.7 ± 1.9	0.4 ± 0.3	2.7 ± 0.8
	19:1	$(40 \pm 20) \times 10^3$	2.0 ± 0.4	5.8 ± 0.3	0.40 ± 0.05	-
	39:1	$(13 \pm 9) \times 10^3$	3.5 ± 0.6	11 ± 3	0.22 ± 0.10	-

Table 5 Results of both the IV characterization and X-ray measurements of the TMTES:PS based X-ray detectors. The sensitivity for the ratios of 19:1 and 39:1 was not calculated because of the negative photoresponse of the samples to X-rays.

As seen from the table, the average sensitivity related to the TMTES:PS ratio of 17:3 surpasses the sensitivity of the devices with lower quantity of PS determined by the 9:1 TMTES:PS proportion, which confirms the positive role of PS in device performance improvement.

5.3 Comparative analysis of TMTES:PS X-ray detectors

Before claiming any plausibility of the obtained results, it is necessary to first verify the values of the electrical properties with those achieved in outer research concerning the TMTES:PS based X-ray detectors. The work conducted by A. Tamayo, L. Basiricò, I. Fratelli *et al.* [33] was already discussed in Chapter 2 (Section 2.6). Therefore, in the next paragraphs I will extract the main information from this study and from other measurements performed on similar samples and I will compare these with my results.

As was also mentioned in Chapter 2, the main aim of this part of the work was to characterize the TMTES:PS phototransistors with several TMTES:PS ratio and to examine the dependence of the device sensitivity on the blend composition. Therefore, to have a broader view on a possible trend in sensitivity change when operating the semiconductor composition proportion, I will combine the outcome of my research with data previously collected by other researchers of the group.

In the research carried out by A. Tamayo *et al.*, the electrical performance was exhibited by the devices with the active channel fabricated by the TMTES:PS blend with the 2:1 ratio and PS of 280 kDa deposited with the coating speed of 10 $mm \cdot s^{-1}$. The average mobility corresponding to such parameters was estimated to be 2.6 ± 0.6 $cm^2/(V \cdot s)$ (maximum mobility found: 3.1 $cm^2/(V \cdot s)$), the threshold voltage was calculated as $-(1.1 \pm 0.2)$ V, whereas the ON/OFF ratio had the order of magnitude of 10^5. The maximum sensitivity per unit volume of the TMTES:PS X-ray detectors was achieved to be $(4.10 \pm 0.05) \times 10^{10}$ $\mu C/(Gy \cdot cm^3)$ [33].

Additionally, in order to convert the sensitivity per unit volume to the sensitivity per unit area, one can multiply the value by the TMTES:PS film thickness of 32 ± 7 nm. The resulting sensitivity per unit area will be equal to (131 ± 29) × 10^3 μC/(Gy·cm^2) (Table 7).

MW	Ratio	ON/OFF	V_{th} (V)	μ (cm^2/(V·s))
280 kDa	**2:1**	10^5	-(1.1 ± 0.2)	2.6 ± 0.6

Table 6 Electrical parameters obtained in [33] for the TMTES:PS based phototransistors. The ratio of 2:1 with PS of 280 kDa provided the maximum mobility μ.

S/Volume (10^{10}×μC/(Gy·cm^3))	*S/Area* (10^3×μC/(Gy·cm^2))
4.10 ± 0.05	131 ± 29

Table 7 Maximum sensitivity per unit volume acquired in [33]. To obtain the corresponding sensitivity per unit area value, the former was multiplied by the TMTES:PS film thickness of 32 ± 7 nm.

As seen from Table 6, the devices related to the TMTES:PS ratio of 2:1 possess noticeably superior electrical parameters than the samples characterized in my experimental study. In particular, the average mobility μ is approximately three times higher than that related to the 17:3 TMTES:PS proportion, and one order of magnitude higher than the minimum average mobility value derived for the 39:1 ratio. The ON/OFF ratio of ~10^5 is similar to the value calculated relatively to the 17:3 ratio. In reference to the devices with smaller relative amount of PS, the 2:1 ratio exhibits an almost one order of magnitude greater ON/OFF ratio, signifying a more pronounced distinction between its operational states. Finally, the average threshold voltage V_{th} calculated for the 2:1-ratio devices, is proportional to 1 V, which is smaller than that for the examined blend proportions and which implies on lower voltage required to switch the phototransistor on. This is particularly advantageous in low-power detection applications.

Regarding the efficiency of X-ray detection, the higher TMTES:PS ratio of 2:1 seems to exhibit greater sensitivity than the blend with lower PS quantity. Comparing exclusively the sensitivity per unit area related to the 17:3 and 9:1 relations, it is seen that their efficiency is almost 50 times lower than that of the blend with the 2:1 TMTES:PS proportion. Nevertheless, it is necessary to take into consideration the biasing conditions of the detectors, which also affect the sensitivity results. In [33], the devices were examined under X-ray radiation at V_{DS} = -15 V and V_{GS} = -20 V, while the samples studied in this work were biased at V_{DS} = -10 V and V_{GS} = -2.5 V, which could result in smaller sensitivity.

Furthermore, I can compare my results with previous measurements carried out on different TMTES:PS ratios and summarized in Table 8:

MW	Ratio	SS (V/dec)	V_{th} (V)	μ (cm^2/(V·s))	$S/Area$ (10^3×μC/(Gy·cm^2))
280 kDa	**1:2**	0.19 ± 0.02	0.13 ± 0.08	0.8 ± 0.1	3.4 ± 0.3
	2:1	0.49 ± 0.04	0.63 ± 0.07	2.4 ± 0.1	5.4 ± 0.9
	4:1	0.23 ± 0.01	0.13 ± 0.04	0.90 ± 0.04	1.7 ± 0.1

Table 8 Average electrical parameters and sensitivity per unit area acquired previously for different TMTES:PS ratio with the PS molecular weight of 280 kDa.

The average mobility reported for the 1:2 and 4:1 TMTES:PS proportions is approximately two times higher than that observed in lower relative PS amount in my samples. Such difference could be related to higher relative amount of PS, which would contribute more significantly to the mitigation of majority carrier interfacial traps in the semiconductor. In general, both studies exhibit the mobility values mostly below 1 cm^2/(V·s). Additionally, the threshold voltage is less than 1 V, while my results demonstrate V_{th} of approximately 10 times higher. Regarding the subthreshold swing, obtained SS values are lower for each ratio, which testifies to less voltage required to switch a phototransistor in the ON-mode.

As for the detection efficiency under X-rays, the analysis of the available data can already provide us an initial overview on the sensitivity behaviour. The consolidated data from both studies is depicted in Fig. 5.6. At the highest relative PS amount (TMTES:PS = 1:2), the sensitivity is at its minimum of (1.7 ± 0.1) × 10^3 μC/(Gy·cm^2). With a reduction of the PS relative quantity, the sensitivity begins to increase and reaches its maximum of (5.4 ± 0.9) × 10^3 μC/(Gy·cm^2) at the TMTES:PS ratio of 4:1. However, with further reduction of polystyrene in the blend (ratios 17:3 and 9:1), the sensitivity tends to decrease, which can be related to the increase interfacial trap density and thus, the deterioration of the electrical performance of the active channel. Nevertheless, further comprehensive examination is still required to form a conclusive understanding of the detector efficiency under varying TMTES:PS proportions.

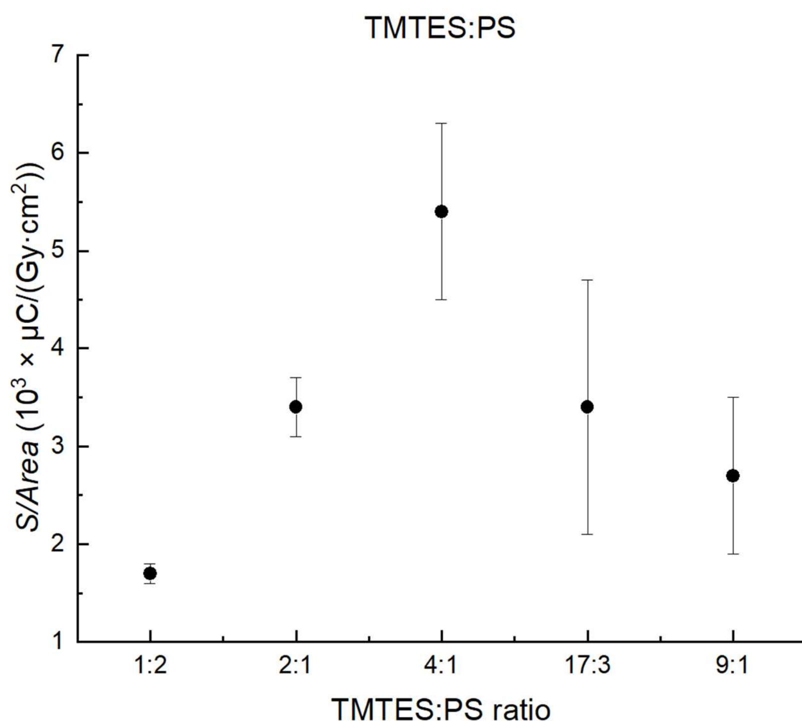

Figure 5.6 The dependence of the average sensitivity per unit area on the TMTES:PS ratio. The data is extracted both from my research on the organic semiconductor (related to the ratio of 17:3 and 9:1) and the work previously conducted by other researchers of the group (related to the TMTES:PS ratio of 1:2, 2:1 and 4:1).

5.4 Side Effects of the TMTES:PS characterization

During the electrical and X-ray characterization of the TMTES:PS-based TFTs, some noticeable imperfections were unveiled for several devices. A significant fraction of the batch (7 samples out of 30) exhibited an anomalous effect, which consists of abrupt increase of the slope in the subthreshold region, while a transistor is passing to the ON-mode. This effect was mostly noticed for the samples with the active channel made of the TMTES:PS blend with the ratio of 17:3 (Fig. 5.7) and 9:1. Since basically two different slopes were present in the transfer characteristics, this effect hindered the calculation of the subthreshold swing *SS*. To overcome such issue, the greater slope of in the subthreshold region was used for calculations of the electrical parameter.

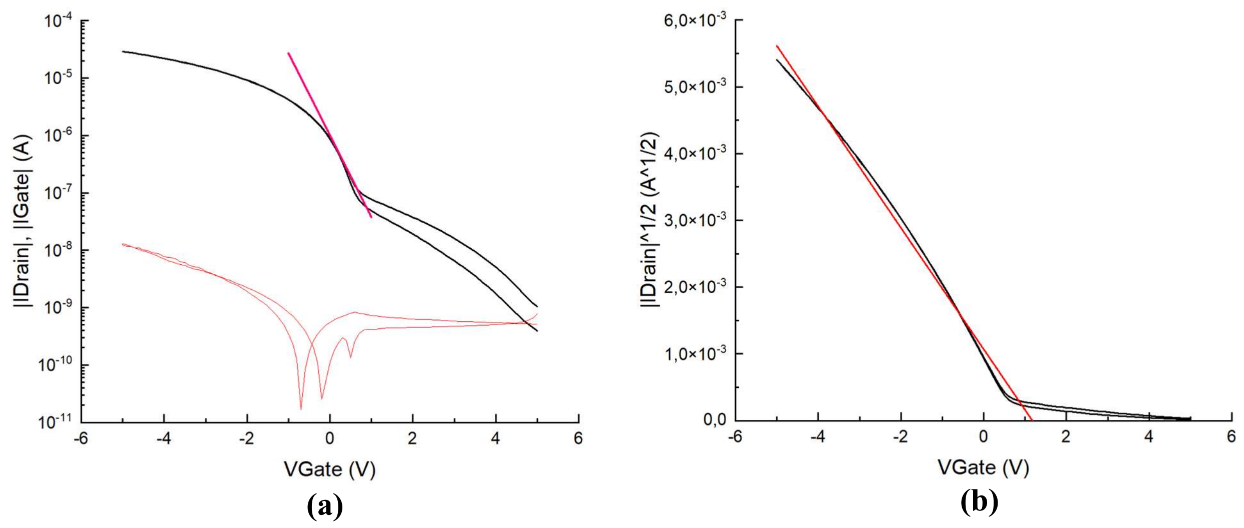

Figure 5.7 Transfer characteristics in saturation regime of a phototransistor of the TMTES:PS ratio of 17:3 showing a non-ideality. In order to calculate its electrical parameters, the greater slope of the linear fit was employed.

Chapter 6 Conclusions

In this experimental research, we studied X-ray detectors based on transition metal dichalcogenide MoS_2 and constructed in the form of thin-film transistors. Through the electrical characterization of the samples, we determined the average electrical parameters of the devices, yielding the ON/OFF ratio of $(0.3 \pm 0.2) \times 10^6$, the subthreshold swing $SS = 4.3 \pm 1.3$ V/dec, the threshold voltage $V_{th} = -(10 \pm 2)$ V and the mobility $\mu = 0.5 \pm 0.2$ cm^2/(V·s). The obtained quantities align well with the corresponding values from outer studies regarding MoS_2-based TFTs.

Subsequent to the electrical characterization, the MoS_2 X-ray detectors were subjected to X-ray radiation at a dose rate ranging from 1 to 6 mGy/s while being biased at the gate voltage ranging from 30 V to 50 V to enhance the photoconductive gain effect. As a result, the sensitivity of the characterized devices was estimated to lie within the range of 10^{11}-10^{12} µC/(Gy·cm^3), which surpasses the sensitivity reported by Taffelli *et al.* [39] by approximately two orders of magnitude.

To study the device performance at varying gate voltage, one of the MoS_2-based photodetectors was exposed to the X-rays of the same dose rate and at V_{GS} from 1 V to 50 V. The resultant sensitivity exhibited a decrease along with elevation of the gate voltage. This phenomenon may be attributed to the formation of new trapping states for majority carriers induced by the impinging X-ray radiation within the conductive channel expanded as the gate voltage increased.

After the characterization of the MoS_2-based photodetectors, we scrutinized the performance of X-ray detectors with the phototransistor architecture based on a fully organic semiconductor TMTES blended with polystyrene PS in different TMTES:PS proportions of 17:3, 9:1, 19:1 and 39:1. Analogously to the earlier phase of the research focused on MoS_2, the electrical characterization of TMTES:PS-based TFTs was initially conducted to derive the average electrical parameters relatively to each TMTES:PS ratio and subsequently to evaluate their respective performance. As a consequence, the average subthreshold swing increased from 0.8 ± 0.2 V/dec for the TMTES:PS ratio of 17:3 to 3.5 ± 0.6 V/dec for that of 39:1. The average threshold voltage also experienced a rise from 1.5 ± 0.3 V to 11 ± 3 V with the reduction of PS from 17:3 to 39:1 TMTES:PS proportion. The average mobility, on the contrary, decreased from 0.7 ± 0.3 cm^2/(V·s) for the ratio of 17:3 to 0.22 ± 0.10 cm^2/(V·s) for that of 39:1. Such mobility behaviour substantiates the incorporation of polystyrene in the blend for passivating interfacial majority carrier traps, consequently improving the sensitivity of the device. Considering the other average electrical parameters, it becomes evident that the electrical performance of TMTES:PS-based TFTs deteriorates with lowering the relative amount of PS.

After the completion of the electrical characterization of the TMTES:PS TFTs, the photodetectors were subjected to X-rays of the dose rate ranging from 1 to 7 mGy/s, while biasing

the gate at -2.5 V. The analysis revealed an average sensitivity of (3.4 ± 1.3) × 10^3 μC/(Gy·cm^2) and (2.7 ± 0.8) × 10^3 μC/(Gy·cm^2) for the TMTES:PS ratio of 17:3 and 9:1, respectively. In comparison with the research conducted by Tamayo *et al.* [33], the calculated sensitivity for each ratio is lower than the reported one by almost two orders of magnitude, which, in its turn, could be prompted by diverse biasing conditions. In addition, to have more comprehensive view on the sensitivity trend across varying TMTES:PS ratios, I integrated the acquired results with the outcome from previous studies examining the relationship between sensitivity and the relative amount of PS in the semiconductor. Based on the combined data, after the minimum value of (1.7 ± 0.1) × 10^3 μC/(Gy·cm^2) at the TMTES:PS ratio of 1:2, the sensitivity achieved its peak of (5.4 ± 0.9) × 10^3 μC/(Gy·cm^2) at the ratio of 4:1 and then experienced decrease with a reduction in the PS quantity at 17:3 and 9:1. Nevertheless, additional sensitivity measurements at different TMTES:PS proportions is necessary to construct a more reliable depiction of the sensitivity trend.

Finally, I would like to go through a comparative analysis of the results of the two parts of my research and to determine if the X-ray detectors based on TMDCs, in particular, on MoS_2 semiconductor, possess superior efficiency towards X-ray detection. When exclusively examining the outcome of my research, it becomes evident that the MoS_2-based phototransistors perform more efficiently under X-rays. From the onset, the sensitivity per unit area of the MoS_2-based OFETs is in the order of magnitude of 10^4 μC/(Gy·cm^2), whereas the TMTES:PS devices show an order of magnitude lower. This enables us to assert that MoS_2-based OFETs do indeed demonstrate superior efficiency towards X-ray detection compared to their TMTES:PS-based counterparts. As a result, even though additional auxiliary research on MoS_2-based X-ray detectors is still required, TMDCs already demonstrated promising performances as active material for thin-film X-ray detectors.

Bibliography

[1] G. F. Knoll, Radiation detection and measurement; 4th ed., New York, NY: Wiley, 2010.

[2] N. &. L. R. Flay, "Application of the optical transfer function in X-ray computed tomography – a review," 2012.

[3] "Synchrotron: Learn its Working Principle, Advantages, & Applications," [Online]. Available: https://testbook.com/physics/synchrotron.

[4] A. Cho, "Rebirth of leading European facility promises revolutionary advances in x-ray science," 2020. [Online]. Available: https://www.science.org/content/article/rebirth-leading-european-facility-promises-revolutionary-advances-x-ray-science.

[5] "X-ray Production, Tubes, and Generators," [Online]. Available: https://radiologykey.com/x-ray-production-tubes-and-generators.

[6] S. P. e. al., "Production of X-RAYS using X-RAY Tube," *Journal of Physics: Conference Series,* 2020.

[7] 05 February 2024. [Online]. Available: https://www.wolfmet.com/tungstenalloys.

[8] O. I. X.-r. Technologies, "Managing the Heat Produced by X-ray Tubes," 05 February 2024. [Online]. Available: https://xray.oxinst.com/learning/view/article/managing-the-heat-produced-by-x-ray-tubes.

[9] J. A. Seibert, "X-ray imaging physics for nuclear medicine technologists. Part 1: Basic principles of x-ray production," *Nuclear Medicine Technology,* 204.

[10] A. S. J. M. B. J, "X-Ray Imaging Physics for Nuclear Medicine Technologists. Part2: X-Ray Interactions and Image Formation," *J Nucl Med Technol,* pp. 3-18, 2005.

[11] B. Nett, “X-Ray Interactions, Illustrated Summary (Photoelectric, Compton, Coherent) for Radiologic Technologists and Radiographers,” [Online]. Available: https://howradiologyworks.com/x-ray-interactions/.

[12] B. P. O. T. a. K. I. David Pennicard, “Semiconductor materials for X-ray detectors,” *MRS Bulletin,* 2017.

[13] Z. Z. &. S. M. A. Datta, “A new generation of direct X-ray detectors for medical and synchrotron imaging applications,” *Scientific Reports,* 2020.

[14] A. C. B. F. Laura Basiricò, “Solution-Grown Organic and Perovskite X-Ray Detectors: A New Paradigm for the Direct Detection of Ionizing Radiation,” *Adv. Mater. Technol.,* 2021.

[15] H. S. Christian W. Fabjan, Particle Physics Reference Library, Volume 2: Detectors for Particles and Radiation, Vienna, Austria: Springer, 2020.

[16] “Silicon Sensors,” [Online]. Available: https://www.dectris.com/en/technology/sensors/silicon-sensors/.

[17] E. E. H. Matthew D. McCluskey, “Dopants and defects in semiconductors, Second Edition,” CRC Press, 2018, pp. 29-33.

[18] D. A. Neamen, “Semiconductor Physics and Devices: Basic Principles, Fourth Edition,” 2012, p. Chapter 4.

[19] A. T. I. R. Ben Depuydt, “Germanium: From the first application of Czochralski crystal growth to large diameter dislocation-free wafers,” in *Materials Science in Semiconductor Processing*, 2006, pp. 437-443.

[20] C. Kittel, “Introduction to Solid State Physics, Eighth Edition,” John Wiley & Sons, Inc., 2005, p. 190.

[21] K. Vetter, “Recent Developments in the Fabrication and Operation of Germanium Detectors,” 2007.

[22] A. B. G. Lioliou, “Gallium Arsenide detectors for X-ray and electron (beta particle) spectroscopy,” *Nuclear Instruments and Methods in Physics Reasearch A,* pp. 37-45, 2016.

[23] S. D. S. L. Abbene, “CdTe Detectors,” in *Comprehensive Biomedical Physics*, Elseiver , 2014, pp. 285-314.

[24] T. S. R. J. H. H. H. Y. M. G. M. Schieber, “Study of impurity segregation, crystallinity and detector performance of melt-grown cadmium zinc telluride crystals,” *Journal of Crystal Growth,* pp. 2082-2090, 2002.

[25] S. Z. M. B. N. S. A. D. C. C. P. a. A. Z. S. Tsigaridas, “Fabrication of Small-Pixel CdZnTe Sensors and Characterization with X-rays,” *Sensors,* 2021.

[26] M. M. K. M. a. G. P. Luisa Torsi, “Organic field-effect transistor sensors: a tutorial review,” *Chem. Soc. Rev.,* 2013.

[27] “Thin-film transistor,” [Online]. Available: https://en.wikipedia.org/wiki/Thin-film_transistor.

[28] H. A. A.-J. P. K. N. J. A. C.-F. N. W. M. N. H. &. H. A. Zhenwei Wang, “Low Temperature Processed Complementary Metal Oxide Semiconductor (CMOS) Device by Oxidation Effect from Capping Layer,” *Scientific Reports,* 2015.

[29] K. K. N. S.M. Sze, Physics of Semiconductor Devices, Third Edition, John Wiley & Sons, Inc., 2007.

[30] S. B. M. e. al., “Electrical characterization of 2D materials-based field-effect transistors,” *2D Mater.,* 2021.

[31] P. L. E. I. K. e. a. Yun Sun, “Key factors for ultra-high on/off ratio thin-film transistors using as-grown carbon nanotube networks,” *RCS Advances,* 2022.

[32] A. C. T. C. P. C. A. B. &. B. F. Laura Basiricò, “Direct X-ray Photoconversion in flexible organic thin film devices operated below 1 V,” *Nature Communications,* 2016.

[33] I. F. A. C. B. F. M. M.-T. L. B. e. a. Adriàn Tamayo, “X-ray Detectors With Ultrahigh Sensitivity Employing High Performance Transistors Based on a Fully Organic Small Molecule Semiconductor/Polymer Blend Active Layer,” *Advanced Electronic Materials,* 2022.

[34] J. S. L. Y. C. J. Z. Y. S. H. C. S. M. L. C. D. Z. G. Z. K. Y. Z. L. S. Hu M, “Large and Dense Organic-Inorganic Hybrid Perovskite CH3NH3PbI3 Wafer Fabricated by One-Step Reactive Direct Wafer Production with High X-ray Sensitivity,” *ACS Appl Mater Interfaces,* 2020.

[35] L. B. I. F. A. T. A. C. M. M.-T. &. B. F. Inés Temiño, “Morphology and mobility as tools to control and unprecedentedly enhance X-ray sensitivity in organic thin-films,” *Nature Communications,* 2020.

[36] K. J. A. P. e. a. H.M. Thirimanne, “High sensitivity organic inorganic hybrid X-ray detectors with direct transduction and broadband response,” *Nature Communications,* 2018.

[37] Ossila, “TIPS-Pentacene,” [Online]. Available: https://www.ossila.com/products/tips-pentacene.

[38] P. K. D. L. A. K. S. P. J. S. Arun Kumar Singh, “2D layered transition metal dichalcogenides (MoS2): Synthesis, applications and theoretical aspects,” *Applied Materials Today,* pp. 242-270, 2018.

[39] M. H. M. F. S. D. L. P. E. J. W. L.-K. A. Q. a. G. L. Alberto Taffelli, “Demonstrating the high sensitivity of MoS2 monolayers in direct X-ray detectors,” *APL Materials,* 1 August 2023.

[40] J. M. S. L. S. T. B. C. S. T. N. K. Saju Joseph, “A review of the synthesis, properties, and applications of 2D transition metal dichalcogenides and their heterostructures,” *Materials Chemistry and Physics,* 2023.

[41] A. K. a. T. Heine, “On the Stability and Electronic Structure of Transition-Metal Dichalcogenide Monolayer Alloys Mo1−xXxS2−ySey with X = W, Nb,” *Electronics,* 2015.

[42] M. S. S. a. C. Mattevi, “Direct synthesis of metastable phases of 2D transition metal dichalcogenides,” *Chem. Soc. Rev. ,* p. 49, 2020.

[43] M. W. a. W. w. F. H. E. T. A. o. S.-G. E.-B. B. 1T-Phase Transition Metal Dichalcogenides (MoS2, “Nasuha Rohaizad, Carmen C. Mayorga-Martinez, Zdenel Sofer and Martin Pumera,” *Applied Materials & Interfaces,* 2017.

[44] A. T. H. F. K. P. e. a. Adam L. Friedman, “Evidence for Chemical Vapor Induced 2H to 1T Phase Transition in MoX2 (X=Se, S) Transition Metal Dichalcogenide Films,” *Scientific Reports,* 2017.

[45] E. J. W. L.-K. Max Heyl, “Only gold can pull thiss off: mechanical exfoliations of transition metal dichalcogenides beyond scotch tape,” *Applied Physics A,* 2022.

[46] D. B. T. S. S. P. G. L. N. K. a. E. J. W. L.-K. Max Heyl, “Thermally Activated Gold-Mediated Transition Metal Dichalcogenide Exfoliation and a Unique Gold-Mediated Transfer,” *hys. Status Solidi RRL,* 2020.

[47] Y. Z. X. L. e. a. Wenli Li, “Gas Sensors Based on Mechanically Exfoliated MoS2 Nanoshhets for Room-Temperature NO2 Detection,” *Sensors,* 2019.

[48] M. B. Luca Seravalli, “A Review on Chemical Vapour Deposition of Two-Dimensional MoS2 Flakes,” *Materials,* 2021.

[49] T. H. K. H. L. Y. R. P. W. C. C. J. L. Ji Heon Kim, “Thickness-dependent electron mobility of single and few-layer MoS2 thin-film transistors,” *AIP Adnvances,* 2016.

[50] H. L. H. L. L. J. e. a. Zongyou Yin, “Singe-Layer MoS2 Phototransistors,” *American Chemical Society,* 2011.

[51] Z. Y. Q. H. H. L. X. H. G. L. D. W. H. F. A. l. Y. T. Q. Z. a. H. Z. Hai Li, “Fabrication of Single- and Multilayer MoS2 Film-Based Field-Effect Transistors for Sensing NO at Room Temperature,” *Small,* pp. 63-67, 2012.

[52] A. R. J. B. V. G. a. A. K. B. Radisavljevic, “Single-layer MoS2 transistors,” *Nature Nantoechnology,* 2011.

[53] “The General Properties of Si, Ge, SiGe, SiO2 and Si3N4,” 2002. [Online]. Available: https://www.virginiasemi.com/pdf/generalpropertiesSi62002.pdf.

[54] “Properties of SiO2 and Si3N4 at 300K,” [Online]. Available: https://eesemi.com/sio2si3n4.htm.

[55] f. P. G. G. e. a. L. Abbene, “Room-temperature X-ray response of cadmium-zinc-telluride pixel detectors grown by the vertical Bridgman technique,” *Journal of synchrotron radiation,* 2019.

[56] "TMTES-pentacene," [Online]. Available: https://www.ossila.com/products/tmtes-pentacene.

[57] "Polystyrene (PS)," [Online]. Available: https://www.sigmaaldrich.com/IT/it/substance/polystyrene123459003536.

[58] [Online]. Available: https://rtigroup.com/.